Karlsruhe Institute of Technology

Geophysical Institute KIT-Dept. of Physics

Ultrasound medical imaging using 2D viscoacoustic full-waveform inversion

Medizinische Bildgebung mit Ultraschall unter Nutzung der 2D viskoakustischen Wellenfeldinversion

Master's Thesis of

Fabian Kühn

at the Geophysical Institute,
Department of Physics

Reviewer:
Prof. Dr. Thomas Bohlen

Second reviewer:
Prof. Dr. Andreas Rietbrock

Date of submission:
12.11.2018

Karlsruher Institut für Technologie
Fakultät für Physik
Postfach 6980
76128 Karlsruhe

Contents

Abstract

In this work I conduct a comprehensive literature research on ultrasound breast imaging with a focus on former applications of full-waveform inversion (FWI) in this field of research, investigate the potential of two-dimensional viscoacoustic FWI by performing reconstruction tests with an anatomically realistic numerical breast model under optimal conditions and examine the feasibility of applying three-dimensional FWI on data acquired with the KIT 3D USCT II, the first automated breast ultrasound data acquisition system with a full three-dimensional acquisition geometry.
The synthetic tests demonstrate a high achievable resolution of speed of sound and attenuation reconstructions even if low frequencies are used which have the dual benefit of yielding a high robustness of the inversion as well as reducing the computational effort. The feasibility study addresses several challenges related to the application of three-dimensional FWI on clinical ultrasound data, e.g. the consideration of transducer characteristics and movements of the breast during the data acquisition. Due to a massive lack of implemented receivers, artifacts caused by spatial aliasing occur in the gradients and the achievable resolution is drastically reduced. Since the achievable resolution is very low, I conclude that the application of three-dimensional FWI on data acquired with the KIT 3D USCT II is not worth the required extremely high computational effort.

Zusammenfassung

In dieser Arbeit führe ich eine ausführliche Literaturrecherche bezüglich der Brustbildgebung mit Ultraschall durch, wobei der Schwerpunkt auf bisherigen Anwendungen der Wellenfeldinversion (WFI) in diesem Forschungsgebiet liegt, untersuche das Potential der zweidimensionalen viskoakustischen WFI mit Hilfe von Rekonstruktionstests mit einem anatomiegetreuen numerischen Brustmodell unter optimalen Bedingungen und prüfe ob sich Datensätze, welche mit dem KIT 3D USCT II, dem ersten automatisierten Brustultraschallsystem mit einer vollständig dreidimensionalen Aufnahmegeometrie, aufgenommen wurden, mit dreidimensionaler WFI ausgewertet werden können.
Die synthetischen Tests zeigen, dass die Schallgeschwindigkeit und Dämpfung mit hoher Genauigkeit rekonstruiert werden können, auch wenn niedrige Frequenzen genutzt werden. Die Nutzung niedriger Frequenzen ist in zweierlei Hinsicht von Vorteil, da diese eine hohe Stabilität der Inversion gewährleistet und gleichzeitig den nötigen Rechenaufwand reduziert. Die Durchführbarkeitsstudie befasst sich mit mehreren Herausforderungen, welchen man sich bei der Anwendung der dreidimensionalen WFI stellen muss, wie zum Beispiel die Berücksichtigung der Abstrahl- und Empfangscharakteristik der verwendeten Ultraschallsonden und Bewegungen der Brust während der Messungen. Es sind viel zu wenige Empfänger installiert, weshalb der räumliche Alias-Effekt Artefakte in den Gradienten hervorruft und nur eine sehr geringe Auflösung erreicht werden kann. Ich komme zu dem Ergebnis, dass eine Anwendung der dreidimensionalen WFI auf Daten des KIT 3D USCT II den extrem hohen Rechenaufwand nicht wert ist, da bei einer so stark begrenzten Auflösung das Potenzial der WFI nicht ausgeschöpft werden würde.

Chapter 1

Introduction

In the last 20 years full-waveform inversion (FWI) has been developed in the geophysical community with great success, as it is able to provide multi-parameter models in high resolution. In FWI, an initial model is iteratively adjusted by minimizing the misfit between the synthetic and the measured data using, e.g., adjoint techniques. By exploiting more information of the measured waveform compared to traveltime tomography, FWI is able to exceed the resolution limit of ray-based methods at the expense of much higher computational costs. In this work I investigate the benefits of transferring the well established seismic FWI technology to ultrasound medical imaging, especially breast cancer screening.
Breast cancer is the most common cancer in women with nearly 1.7 million new cases diagnosed worldwide in 2012 (Ervik et al., 2016). Nowadays, mammography using X-rays is the common approach for breast cancer screening. However, it is more and more often replaced by ultrasound tomography, which is non-invasive, provides more reproducible results due to the fact that the breast is not deformed during data acquisition and has the potential to provide more reliable results in dense breasts. Increased breast density is a well-known breast cancer risk factor and complicates imaging of tumors as the contrast between the tumor and surrounding breast tissue is reduced in terms of density and speed of sound. Improvements in ultrasound tomography based on FWI could help to detect small cancers earlier, in particular among the aforementioned risk group, and thus improve the survival rate of patients.

In chapter 2 the basic concepts of medical ultrasound are introduced by performing a literature research on the history of medical ultrasound. The literature research highlights the individual development steps which finally led to the first applications of FWI on breast ultrasound by Pratt et al. (2007). A detailed overview of subsequent studies in this field demonstrates the current state of the research. Furthermore, the basic anatomy of the breast and the formation of breast cancer is presented as they are of fundamental importance in understanding how tumors can be detected with ultrasound.

The theoretical principles of viscoacoustic wave propagation, its numerical solution using the finite-differences (FD) method and full-waveform inversion are introduced in chapter 3. The focus lies on the description of the single aspects of my inversion strategy and on the proposal of a criterion to determine an appropriate spatial and temporal discretization for the FD forward modeling in order to obtain a sufficient accuracy of the simulated wavefields despite numerical dispersion greatly affecting the simulation due to the large number of propagated wavelengths in breast ultrasound.
Former synthetic tests using FWI for breast imaging consider very simple breast models and most of them invert exclusively for the speed of sound. In chapter 4 I present reconstruction tests using two-dimensional viscoacoustic FWI considering an anatomically authentic numerical breast model under optimal conditions in order to investigate the potential of FWI in a more realistic scenario. Even in seismics the accurate reconstruction of the attenuation using viscoacoustic FWI is still a great challenge. Moreover, the forward-simulated data are analyzed in order to study ultrasound wave propagation within the breast because a deep understanding of the occurring wave phenomena is crucial for analyzing measured data in clinical applications and the optimization of the full-waveform inversion strategy.
Sandhu et al. (2017), Wiskin et al. (2017) and Agudo et al. (2018) published the first studies using three-dimensional FWI algorithms which clearly demonstrated that the application of two-dimensional FWI on three-dimensional datasets lead to a significant loss of the achievable resolution and the occurrence of artifacts caused by out-of-plane scattering. Obviously, measured data are always affected by three-dimensional wave phenomena. All of these experiments were restricted to synthetic tests.
In chapter 5 I investigate the feasibility of applying three-dimensional FWI on data acquired with the KIT 3D USCT II, the first automated breast ultrasound system with a full three-dimensional acquisition geometry, as a preliminary study for the potential first application of three-dimensional FWI on measured data.

Chapter 2

Medical ultrasound computed tomography

In this chapter the basic concepts of medical ultrasound are presented. In section 2.1 the most important fields of application, the basic imaging modes and terminology used in medical ultrasound are introduced by summarizing its development history. After that two main categories of experimental set-ups either using the reflected or refracted parts of the wavefield are presented. In the last part the commonalities and differences of seismic and medical ultrasound with a focus on full-waveform inversion are discussed. In section 2.2 the history of ultrasound for early breast cancer detection is discussed at first. The focus is on developments which lead to the first application of full-waveform inversion in this field. Then the medical background of breast cancer, including an introduction to the anatomy of a woman's breast and the development of breast cancer, is presented. Subsequently, the major breast imaging techniques, namely mammography, ultrasound and magnetic resonance imaging, are introduced and compared with each other. At last a literature research of former applications of full-waveform inversion in the field of breast ultrasound imaging is shown.

2.1 Medical ultrasound imaging in general

2.1.1 Development history and ultrasound modes

Ultrasound is defined as sound waves with frequencies higher than the upper audible limit of human hearing, which is approximately 18 kHz. Depending on their intensity, ultrasound waves are used for a wide variety of applications.
High amplitude or high intensity ultrasound waves are used for cutting, cleaning and precise destruction of tissue in industry and in the medical field. For example, high-intensity focused ultrasound is used for highly localized heating to treat cysts and tumors and in lithotripsy ultrasound waves are used for breaking up kidney stones and gallstones. A nice overview of such therapeutic ultrasound applications is given by Miller et al. (2012).

In this work I focus on low intensity ultrasound waves, which are used for non-destructive testing and medical imaging. For these applications the intensity must be low enough to prevent damages at the tested objects and to ensure that the maximum applied stresses do not exceed the elastic limit below which Hooke's law (see section 3.1.1) is assumed to be valid (Blitz and Simpson, 1995).

The history of non-destructive testing and medical imaging begins 1880 with the discovery of the piezoelectric effect by the brothers Pierre and Jacques Curie. According to this, mechanical deformation of certain solids generates electrical voltage, which is the basis for pressure sensors. The reverse effect, i.e. voltage leads to deformation of such materials, can be used for generating ultrasound waves. In ultrasound both, sources and receivers, are called transducers because they convert mechanical to electrical energy (and vice versa) based on the aforementioned piezoelectric effect. About 60 years later during World War II, after the discovery of radar, the acoustical physicist Floyd Firestone invented the ultrasound reflectoscope in which he adapted the pulse-echo ranging principle of radar for the detection of defects in metals (Szabo, 2014, chapter 1).

After commercialization of the reflectoscope medical imaging was born. First attempts with simple A-scans have been made in the late 1940s and early 1950s. An A-mode image or A-scan, short for amplitude scan, refers to a single trace of a pressure seismogram in seismics. In the following I summarize some of the most important experiments.
George Ludwig used a modified version of the reflectoscope to locate gallstones in an in-vitro experiment (studies with components of an organism isolated from their usual biological surroundings) in 1949. In 1950 Ludwig performed measurements of speed of sound and acoustic impedance of various tissues in human bodies whose results are partially still valid despite the simplicity of the experiment (Szabo, 2014, chapter 1).
Wild and Reid (1952) were the first to analyze breast A-scans to differentiate between benign and malignant tissue. Additionally they published the very first B-scans of women's breasts in this paper, which are shown in figure 2.1. In a B-mode image or B-scan, short for brightness scan, the amplitudes of various A-scans are imaged along corresponding ray paths (beam-forming ultrasound sources are required) as brightness values side by side in one common 2D plot. This is is similar to an image plot of a zero-offset section in seismics. In a more general sense, a B-scan is used as a synonym for reflectivity images obtained by any migration algorithm.
By publishing this work, Wild and Reid have founded the field of ultrasound breast imaging. Further developments in this particular field are presented in section 2.2.
In 1953 Inge Edler and Carl Hellmuth Hertz were the first to detect heart motions and developed echocardiography, the medical field of imaging and characterizing the human heart with ultrasound. Therefore, they introduced the M-mode with which it is possible to investigate time-dependent processes. In M-mode imaging, short for motion mode imaging, ultrasound pulses are repetitively emitted and each time either an A-mode or B-mode image is taken. Similar to the results of 4D seismics, the obtained "video" contains information about time-varying processes (Szabo, 2014, chapter 1).

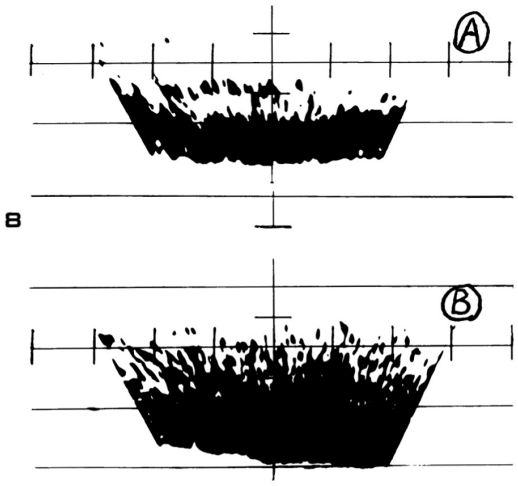

Figure 2.1: First-ever published B-scan of a woman's breasts. Image (A) shows a healthy breast and image (B) shows a breast with a lesion, an abnormal damage or change in the tissue of an organism (Wild and Reid, 1952).

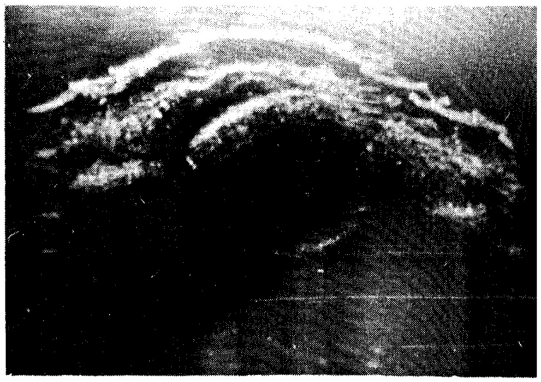

Figure 2.2: First-ever published B-scan of a fetal head in the 34th week of pregnancy. (Donald et al., 1958).

Satomura (1956) adapted technology from radar to ultrasound and introduced the Doppler-mode to measure and visualize blood flows and heart motion. The Doppler-mode makes use of the eponymous effect stating that a relative motion between source and receiver causes a change in the frequency of the observed wave. This can be used to obtain information of the velocity of moving reflectors, e.g. flowing blood in the heart or vascular system.
Donald et al. (1958) started the nowadays probably best-known medical application of ultrasound, the prenatal imaging of a developing embryo or fetus in its mother's uterus called obstetric ultrasound. In figure 2.2 the first-ever published B-scan of a fetal head in the 34th week of pregnancy is shown.

Since the beginnings of ultrasound imaging enormous progress has been made due to the rapid advancements in computer technology and electronics. These have made it possible to use more sophisticated signal processing schemes and reconstruction algorithms to generate more and more detailed ultrasound images from data with increasing quality. As an example fetal images from 1960 to 2002 are shown in figure 2.3.

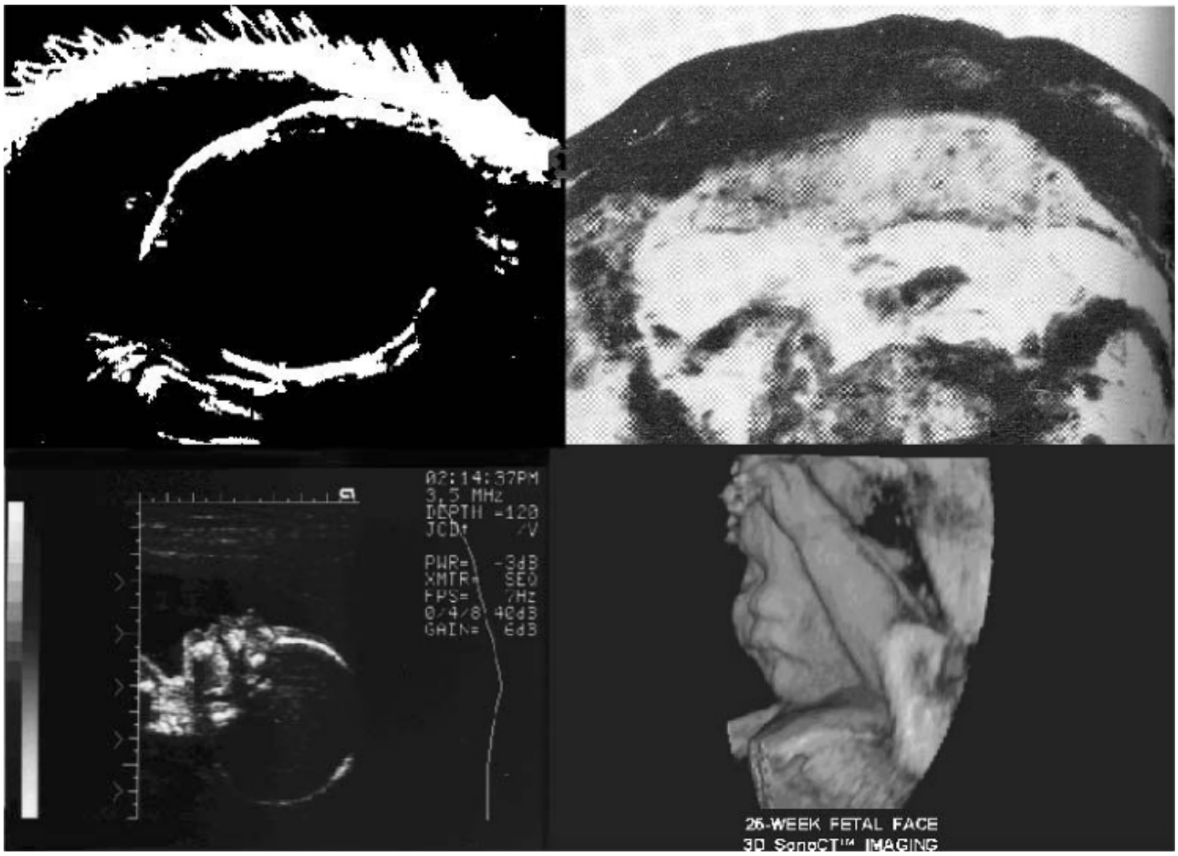

Figure 2.3: The development of medical ultrasound imaging as shown in fetal images. (Upper left) Fetal head black-and-white image from 1960. (Upper right) Early grayscale negative image of fetus from the 1970s. (Lower left) High-resolution fetal profile from the 1980s. (Lower right) Surface-rendered fetal face and hand from 2002 (Szabo, 2014, chapter1).

2.1.2 Backscatter vs. transmission mode

The large number of different applications leads to numerous, different experimental set-ups. These can roughly be divided into two categories depending on their acquisition geometries.
On the one hand, there are set-ups which are designed for the backscatter or echo mode in which the reflected parts of the wavefield are observed and evaluated. Typically handheld ultrasound devices are used, where the receivers are arranged in an array close to the source in the ultrasound probe (see figure 2.4). Coupling agents like gel, mineral oil and white petrolatum are used for minimizing the energy loss by reducing the acoustic impedance contrast between the probe and the skin to suppress reflections (Casarotto et al., 2004). On the other hand there are automated breast ultrasound systems (ABUS) in which either the transmitted parts of the wavefield or even the whole wavefield are observed at receivers opposite of the ultrasound source or all around the object of interest, respectively (see figure 2.4).

Such tomographic set-ups were frequently used in the early beginnings of ultrasound imaging but have increasingly been replaced by hand-held systems because they are more flexible in their applicability, much smaller, real-time capable and less expensive (Dempsey, 2004). However, tomography systems have experienced a renaissance since the 1980s when sufficient computational power was available to make medical ultrasound computed tomography applicable, where inverse problems are computationally solved to reconstruct quantitative images of physical properties such as speed of sound and attenuation to overcome the purely qualitative results of B-mode imaging (Greenleaf, 2018).
Nowadays, tomographic systems are mostly used in breast imaging because it is necessary to insert the object of interest in a tank filled with a coupling agent, usually degassed water, to guarantee a sufficient coupling. While this is relatively easy for a woman's breast, it can be problematic in the case of internal organs. In principle it would be possible to insert the whole human body in a water tank but this would yield some other problems regarding strong attenuation and extreme complexity of the wavefields due to strong heterogeneities and the large number of propagated wavelengths.
ABUS have the major advantage that their results are more reproducible because the data acquisition does not depend on the practicing physician. The high number of receivers makes it possible to collect more data compared to hand-held systems. On the one hand this leads to some technical difficulties and makes the inversion computationally demanding especially in 3D set-ups. On the other hand these data contain more information, e.g. about the attenuation in the transmitted phases, which can be used to reconstruct more detailed tomograms.

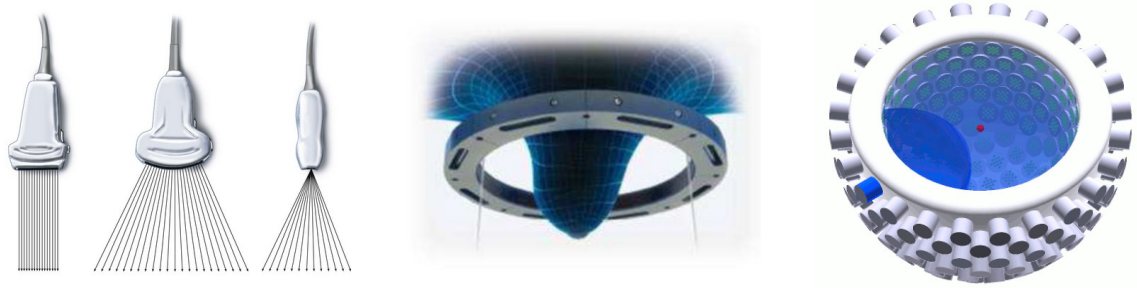

Figure 2.4: Ultrasound acquisition geometries. [Left] Schematic illustration of hand-held ultrasound probes. From left to right a linear array probe, a curved array probe and a phased array probe are shown. The arrows present individual ultrasound beams emitted by the transducer arrays (Karmakar and Kwok, 2016). [Middle] Scheme of a 2D tomographic geometry as used in breast ultrasound imaging. Transducers are spread over a ring array, which can be displaced in the vertical direction to image the whole breast (Sandhu et al., 2015). [Right] Scheme of a full 3D tomographic geometry as used in breast ultrasound imaging. Transducers are spread over a semi-ellipsoid. In blue an active source and its wavefield are shown (Ruiter et al., 2018b).

2.1.3 Comparison with seismics

In both cases, seismic and ultrasound imaging, elastic or acoustic waves are generated, observed and analyzed to obtain information about the unknown propagation medium. The physics of wave propagation is exactly the same, but the scale of the parameters differs as is shown in table 2.1.
There are many parallels in the methodology of analyzing the wave data. Analogue to the prior section, in the following I will distinguish between the evaluation of backscattered aka reflected waves and transmitted aka refracted waves.

Seismic reflection methods correspond to the backscatter mode in ultrasound imaging. The common approaches in medical ultrasound are B-mode imaging and synthetic aperture focusing techniques (SAFT) (Jensen et al., 2010). The latter are equivalent to Kirchhoff migration (Schneider, 1978) in reflection seismics. However, there are differences in the procedure. In reflection seismics the data acquisition and extensive processing of a single dataset, as described in Yilmaz (2001), usually requires weeks to months while medical ultrasound targets real-time analysis.
Velocity models in reflection seismics are typically obtained by evaluating the traveltimes of reflections based on their coherency in a so called velocity model building. The resulting smooth, low-wavenumber models are then used in the migration, in which also the high-wavenumber components, contained in the waveforms of the reflections, are evaluated to create detailed reflectivity images of the subsurface.

The reconstruction of velocity models in ultrasound is typically restricted to the analysis of transmitted aka refracted waves in tomography set-ups. Conventional ray-based tomography methods, as used in seismics and ultrasound, also result in smooth velocity models because only traveltimes are evaluated. Similar to seismics the reflectivity images obtained by B-mode imaging or SAFT are much more detailed. A comparison of common imaging methods for ultrasound imaging is given by Ozmen et al. (2015).
If no transmission ultrasound data exist, usually homogeneous models are considered for the application of SAFT. This approximation can be made because the speed of sound in most biological, soft tissues (e.g. breast tissue) hardly differs from that of water (Szabo, 2014, appendix B). Additionally, this yields small reflection coefficients which reduce the effect of out-of-plane scattering in the 2D analysis of 3D datasets. Moreover elastic effects will be negligible if no bones are located in the propagation medium. In contrast to that, in seismics we usually cannot ignore elastic wave effects such as mode conversions and the presence of high amplitude, dispersive surface waves, 3D heterogeneity and anisotropic wave propagation (Pratt, 2018).
More sophisticated tomography methods overcoming the ray approximation, such as, for instance, diffraction tomography and full-waveform inversion which are able to produce more detailed velocity models, are mostly used in seismics due to the high computational costs. However, these methods become more and more interesting in medical ultrasound imaging because of the development of more effective algorithms and the ever increasing computational power that is available.

Table 2.1: Comparison of the scale of parameters in exploration seismics and medical ultrasound based on Pratt (2018). For both cases typical values for low and high frequencies are presented individually. The size of the Fresnel zone corresponds to the horizontal resolution of common ray-based inversion techniques. The achievable resolution in full-waveform inversion is in the order of $\lambda/4$. The definition of the seismic Q-factor and the attenuation factor α as well as the conversion between both quantities is shown in section 3.1.2. Here α is assumed to linearly depend on f.

Parameter		**Exploration seismics**		**Medical Ultrasound**	
		Low frequency	High frequency	Low frequency	High frequency
Propagation distance	L	16 km	16 km	15 cm	15 cm
Frequencies	f	2.5 Hz	25 Hz	1 MHz	3 MHz
Speed of sound	c	4000 m/s	4000 m/s	1500 m/s	1500 m/s
Wavelength	$\lambda = c/f$	1.6 km	0.16 km	0.15 cm	0.05 cm
Fresnel zone size	$\sqrt{L\lambda}$	4.9 km	1.5 km	1.5 cm	0.9 cm
Number of wavelengths	$N_\lambda = L/\lambda$	10	100	100	300
Seismic Q	Q	500	500	200	200
Attenuation factor α	$\frac{20}{\ln 10}\frac{\pi}{cQ}$	0.14 dB/cm/MHz	0.14 dB/cm/MHz	0.91 dB/cm/MHz	0.91 dB/cm/MHz
Total attenuation	$\alpha L f$	0.55 dB	5.5 dB	14 dB	41 dB

Full-waveform inversion in ultrasound benefits from the aforementioned characteristics of biological, soft tissues. By neglecting anisotropic and elastic effects the (isotropic) acoustic approximation of the elastic wave equation can be used, which significantly reduces the necessary computational efforts. Sources and receivers located all around the object of interest (in transmission geometry) enable an optimal illumination. Relatively small variations in the speed of sound make it easier to find an appropriate initial model, which reduces the risk of non-convergence (more information are given in section 3.3.1). As shown in table 2.1, the large number of propagated wavelengths N_λ and the high attenuation factor α yield much higher total attenuation. Combined with the transmission geometry and by considering the viscoacoustic wave equation this represents ideal conditions for inverting the attenuation.
On the other hand, some of these properties can also lead to difficulties. The large number of propagated wavelengths increases the computational costs and the risk of non-convergence due to the high complexity of the wavefield (Pratt, 2008). Especially for high frequencies the strong attenuation dramatically worsens the signal-to-noise ratio.

Major differences are related to the sources and receivers. In conventional ultrasound beam-forming sources are used to enable B-mode imaging. The beam-forming has to main causes. Firstly, many ultrasound devices use arrays of sources instead of single senders to achieve beam-forming (Szabo, 2014, chapter 7). Secondly, the size of the sender elements is in the same order of magnitude than the wavelengths (Szabo, 2014, chapter 6). This makes it more challenging to correctly simulate them, because the point source approximation, which is usually used in seismics, is not valid in this case. The stronger the beam-forming, the smaller the opening angle, which leads to a less uniform illumination as shown in figure 2.5.
A similar problem can be observed for receivers because their size is equivalent to those of the sources (usually the same transducers are used). Strong receiver characteristics arise from this, where the response function depends on the incidence angle and the wavelength or frequency of an incident wave. The aforementioned effects are investigated in more detail in sections 3.4 and 5.3.5.

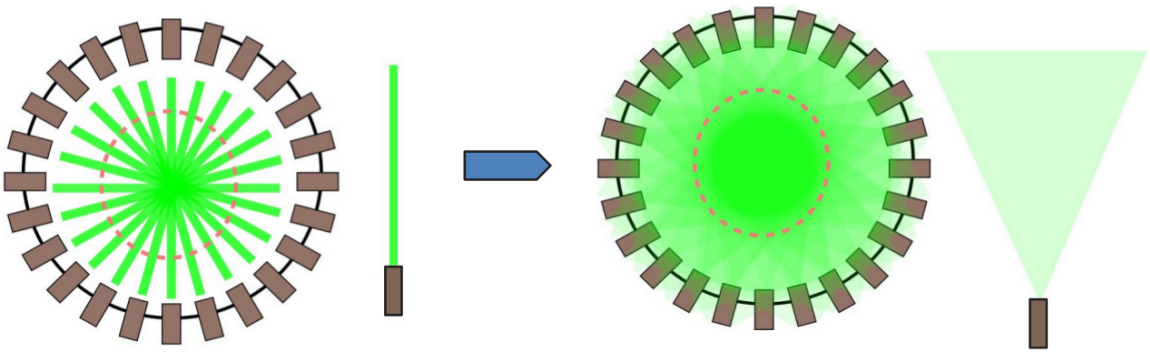

Figure 2.5: Dependency of the illumination on the opening angle of the sources. The stronger the beam-forming, the less uniform the area of interest (red dashed circle) is illuminated (Zapf et al., 2018).

2.2 Imaging of the breast

The publications of Dempsey (2004); Szabo (2014) and Greenleaf (2018) present the development history of ultrasound in great details. In the following, the most important facts with respect to the developments, which lead to the first applications of full-waveform inversion on data acquired with modern automated breast ultrasound systems, are summarized.

As mentioned in section 2.1.1, the first breast ultrasound examinations were published by Wild and Reid (1952). The goal of this work was the preoperative distinction between benign and malignant lesions. Histological examinations of the surgically removed lesions showed the great potential of this application by confirming the characterization of all 21 objects of investigation. Furthermore they published the first B-scan of a human breast (see figure 2.1) in this work. Already two years later the technique for preoperative characterization of lesions was ready for the first clinical application (Wild and Reid, 1954).
During the 1960s, the first ultrasound tomography breast scanner, in which the patients were lying prone with the breasts suspended in a temperature-controlled water bath (see figure 2.6,) was built and tested. The device used a center frequency of 2 MHz and was able to perform one B-scan in approximately one minute (Wells and Evans, 1968). This kind of set-up is used in almost all modern ultrasound breast scanners.

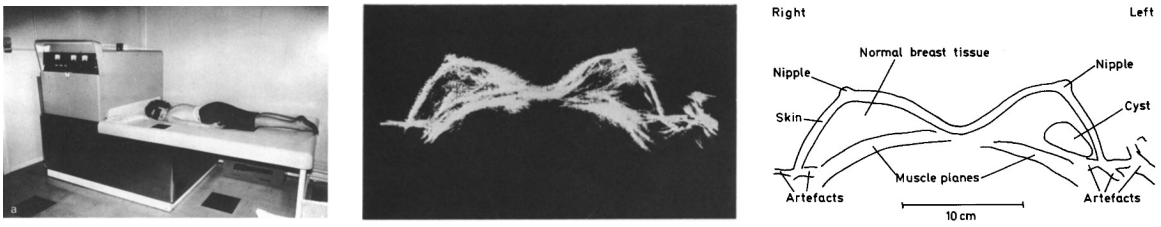

Figure 2.6: Ultrasound tomography breast scanner and first results from Wells and Evans (1968). [Left] First ultrasound scanning device in which the breasts are suspended in a temperature-controlled water bath. The patient is placed in a prone position. [Middle] Transverse B-scan of a patient's breasts in the first clinical tests. [Right] Interpretation of the shown B-scan.

In the early 1970s a major improvement occurred when grayscale B-mode imaging was introduced by Jellins et al. (1971, 1975). Such B-scans allowed a much better differentiation of the constituent tissues of the breast compared with the prior binary images (compare figures 2.6 and 2.7).
At the same time, asymptomatic, healthy breasts were examined by Fry et al. (1972). This was the first attempt to use ultrasound for early breast cancer detection (screening) instead of using it for the characterization of known, suspicious masses, which had formerly been detected with X-ray or palpation.

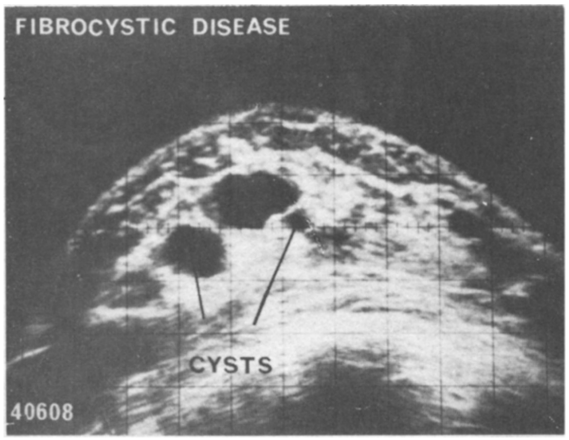

Figure 2.7: Grayscale B-scan of a breast suffering from fibrocystic disease (Jellins et al., 1975).

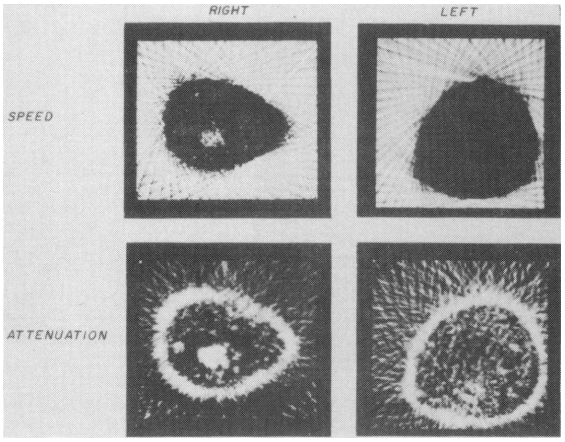

Figure 2.8: Reconstructions of speed of sound and attenuation showing scirrous carcinoma in the right breast based on ultrasound computed tomography (Greenleaf and Bahn, 1981).

A major step in the direction of using full-waveform inversion for ultrasound breast imaging was done in the 1970s when the theoretical basis of ultrasound computed tomography was introduced by Greenleaf et al. (1974). Using those ray-based algorithms it was possible to quantitatively reconstruct 2D distributions of speed of sound and attenuation in single slices of a breast for the first time, as shown in figure 2.8. These reconstructions could be used for tissue characterizations themselves and the distribution of speed of sound could additionally be used for correcting or improving the reconstructions of the reflectivity. Greenleaf and Bahn (1981) published the first clinical study based on results from ultrasound computed tomography, in which they quantitatively analyzed speed of sound and attenuation to categorize breast tissue (see figure 2.10).

Based on these developments, the digital revolution, which started in the 1980s and offered many new capabilities regarding signal processing, the significant improvements of electronic measuring equipment and the possibility to use more and more complex reconstruction algorithms due to the increasing computational power, the quality of ultrasound tomograms has continuously enhanced for the last 50 years.
In 2007 the well-established seismic full-waveform inversion technique were successfully transferred to ultrasound breast imaging by Pratt et al. (2007) for the first time. By exploiting more information of the measured waveform compared to traveltime tomography, FWI is able to exceed the resolution limit of ray-based methods at the expense of much higher computational costs. A detailed overview of this work and subsequent research projects is given in section 2.2.3.

2.2.1 Medical background

A healthy breast roughly consists of glandular tissue involving globules which produce milk and milk ducts which transport it to the nipples, connective or fibrous tissue and fat, also called adipose tissue. The breast is streaked by blood vessels and limited by the skin and the chest wall (Netter, 2017). On the left side of figure 2.9 an anatomically sketch of a woman's breast is shown.
Fibrous and glandular tissue are often combined to fibroglandular tissue based on their density and the BI-RADS classification. BI-RADS (breast imaging - reporting and data system) is a widely accepted classification system by the American College of Radiology for standardized risk assessment and quality control for mammography, ultrasound and magnetic resonance imaging. The classification of the results of ultrasound examinations takes various aspects into account, e.g. the shape, orientation, margin and echo pattern of suspicious masses, calcification and the tissue composition based on the overall density. The latter is based on the ratio and the relative distribution of fat and fibroglandular tissue (the higher the percentage of fibroglandular tissue the more dense the breast). On the basis of these (and some more) criteria lesions in breasts are assigned to one of six final assessment categories, which are related to specific treatment processes and chances of malignancy (D'Orsi and Acr, 2013).

In the following different kinds of cellular abnormality, whose detection and diagnosis is targeted by breast imaging, are introduced based on the descriptions given by Cooper (1992).
The most general term lesion describes any abnormal change in the tissue of an organism. Lesions can be caused by diseases or trauma.
A neoplasm is any abnormal growth of cells, which persists even if the original trigger is removed and is uncoordinated with the growth of surrounding tissue. It usually forms a mass which is called tumor. All tumors can be classified as lesions but not all lesions are tumors. Tumors can either be benign or malignant.
Benign tumors are usually enclosed in a fibrous capsule and neither invade the surrounding, healthy tissue nor spread to other parts of the body. Usually, they are not life-threatening because they remain localized to their original location and thus can be completely removed. Cysts, fluid-filled sacs, and common skin warts are examples of benign tumors.
Malignant tumors, also known as cancer, are characterized by their ability to metastasize. This means that the tumor can invade normal tissue and spread throughout the body, making them so dangerous and difficult to treat. After metastases have occurred, localized treatments such as surgery are no longer able to cure cancer. Malignant tumors are classified by the type of their original cells. Carcinomas develop from epithelial cells which build up the outer surfaces of organs and blood vessels.

Breast cancer most commonly develops in the epithelial cells of milk ducts (ductal carcinomas) and the lobules (lobular carcinomas). It is understood that spatial proximity to fat is very important for the initiation of cancer. That is why 99% of malignant tumors are localized at the interface of fibroglandular and adipose tissue (Littrup et al., 2018).

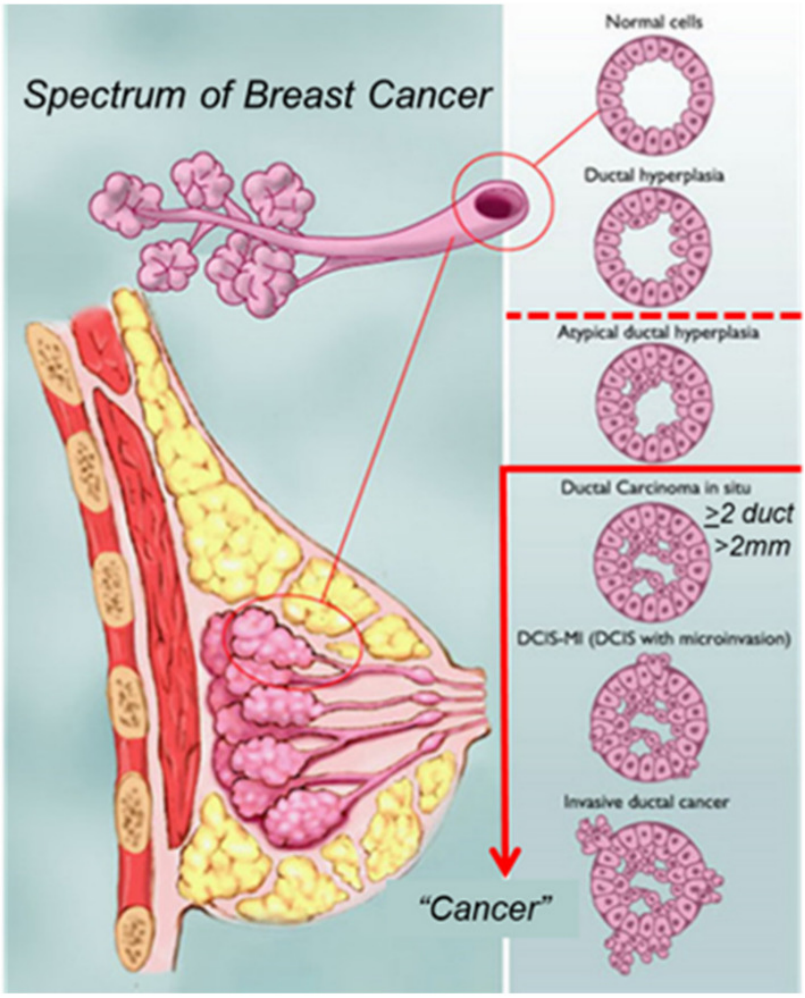

Figure 2.9: On the left side the anatomy of a woman's breast is shown. Glandular tissue, involving globules which produce milk and ducts which transport it to the nipples, is shown in dark rose. Adipose tissue consisting of fat is shown in yellow. Muscles (red) and ribs (brown) build up the chest wall. Fibrous tissue or connective tissue is shown in light rose. Blood vessels are not shown. On the right side the development of a ductal carcinoma is shown. It extends from high risk lesions, such as atypical ductal hyperplasia to multiple forms of ductal carcinoma in situ and invasive cancer (Littrup et al., 2018).

On the right side of figure 2.9 the development of an invasive ductal carcinoma starting from a normal duct is show. A normal milk duct consists of a single layer of epithelial cells. Hyperplasia describes the state when these cells begin to grow to multiple layers and fill the inner of the duct, which increases the tissue's density and stiffness. If the additional layers are build up of unevenly distributed cells it is called atypical ductal hyperplasia. Ductal carcinoma is diagnosed if either more than 2 ducts are involved or the extent of atypical ductal hyperplasia is greater than 2 mm. Carcinomas which have not started to metastasize are marked by the suffix in situ. If the metastases have already begun, they are called invasive (Littrup et al., 2018).

The described developments on cellular level yield an increase of the density and elastic parameters, e.g. the bulk modulus, and consequently the speed of sound (see equation 3.11). The potential of characterizing different tissues, especially cancer, based on their viscoelastic properties, namely speed of sound and attenuation, has already been recognized by Greenleaf and Bahn (1981) during the first clinical study of ultrasound computed tomography. The results, which are still valid today, are shown in figure 2.10.

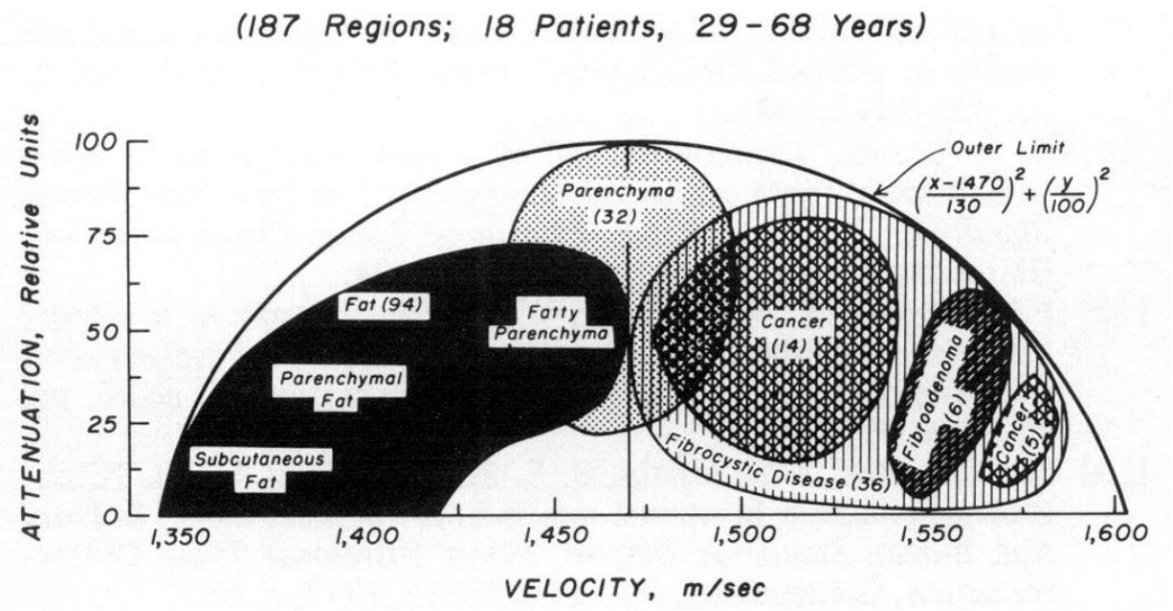

Figure 2.10: Empirical relationship between speed of sound and relative attenuation in different breast tissues. Parenchyma denotes the functional parts of organs. In the breast this refers to glandular tissue (Greenleaf and Bahn, 1981).

Breast cancer is the most common cancer in women and second most common cancer overall, with nearly 1.7 million new cases diagnosed worldwide in 2012. This represents about 12% of all new cancer cases and 25% of all cancers in women. It is the fifth most common cause of death from cancer in women (Ervik et al., 2016).

Breast cancer is more common after menopause. However, 25-30% of breast cancer occurs in premenopausal woman and 30% of menopausal women have dense breasts (high percentage of fibroglandular tissue) where the current standard screening method mammography, breast imaging with X-rays, fails in up to 50%. These young women with dense breasts represent a special risk group, because dense breast tissue is also one of the most important risk factors of breast cancer (Madjar, 2018). A study of Boyd et al. (2007) with more than 200 000 women showed that the risk of breast cancer is five times increased in breasts in which more than 75% of tissue is dense.

Breast cancer detection can be performed with several methods. Palpation has been used exclusively before imaging methods became available. A physician uses his hands and sense of touch to identify lesions based on changes in the stiffness. To be detectable the cancer must have progressed so far that it is perceptible by the physician. For the diagnosis of detected suspicious masses needle biopsies are necessary.
Imaging methods are able to detect malignant tumors earlier, which significantly increases the chance of successfully curing them (Aiello et al., 2004; Chen et al., 2017), and they are more independent on the skills of the attending physician. Additionally, they can be used for diagnosis of lesions. However, final diagnosis is always done by histological examinations of biopsied samples.
Mammography and ultrasound make use of the increase of density and stiffness of cancerous tissue. Magnetic resonance imaging is based on an enhanced concentration of an injected contrast agent due to increased blood supply of tumors. A detailed comparison of those imaging techniques is given in the next section.

2.2.2 Comparison of different imaging techniques

The major breast imaging techniques are mammography, ultrasound and magnetic resonance imaging.

Mammography is the standard screening method. X-rays propagate with the speed of light on approximately straight rays. Due to wavelengths less than 1 µm diffraction is negligible. Thus, reconstruction algorithms are relatively simple and the resolution of obtained images is high. Resulting images show 2D projections of the 3D distribution of X-ray absorption, where the shown values refer to the mean of the absorption coefficient along the ray paths which are oriented perpendicular to the imaged plane. X-ray absorption mainly depends on the mass density of the propagation medium (Szabo, 2014, chapter 1).
However, in women with dense breasts, who have a higher risk of developing breast cancer, mammography fails in up to 50% (Madjar, 2018) due to the low contrast between the X-ray absorption coefficients of fibroglandular and cancerous tissue. Computed tomography is able to produce volumetric images of the breast in contrast to common two-dimensional mammography. By showing the distribution of X-ray absorption coefficients instead of their 2D projections, computerized tomography is able to better detect small lesion in fibroglandular tissue at the expense of a higher dose of ionizing

radiation and higher costs (Szabo, 2014, chapter 1). Furthermore in mammography breasts are compressed between two metal plates to prevent movements during data acquisition. This is uncomfortable for patients and lowers the reproducibility of the images, which can lead to problems especially if breasts are imaged for treatment monitoring e.g. during chemotherapy.

Magnetic resonance imaging is based on measuring the reaction of nuclei of hydrogen atoms (single protons), which are stimulated by radio waves of a particular frequency, in a strong, static, externally applied magnetic field. The nuclei re-emit a part of the absorbed energy in form of radio signals. These signal are observed with radio antennas and their points of origin can be localized (Pykett et al., 1982).
Hydrogen atoms are abundant in fat and water and thus magnetic resonance imaging naturally maps the distribution of fat and water in a human's body. In breast imaging contrast agents are used, which concentrate in highly blood supplied tissues like tumors, and make them detectable (Szabo, 2014, chapter 1).
This method is able to produce detailed 3D images even in dense breasts and thus improves the sensitivity of tissue characterization without ionizing radiation. However, magnetic resonance imaging is very expensive, examinations take a long time and specificity can be reduced (Duric et al., 2018).
Specificity is defined as the ratio between true negative and the sum of true negative and false positive diagnoses. Analogously, sensitivity is defined as the ratio between true positives and the sum of true positives and false negatives.

Ultrasound imaging is supposed to be an equivalent, low-cost alternative for magnetic resonance imaging. Duric et al. (2018) analyzed the statistics from ten major medical studies from 1995 to 2015 to prove the effectiveness of hand-held ultrasound imaging in detecting breast cancer, particularly for women with dense breasts. They showed that ultrasound examinations are able to almost double the detection rate of invasive cancers in dense breasts in comparison to mammography. However, the sensitivity to ductal carcinomas in situ is reduced. For the assessment of this trade-off the much higher mortality rate of invasive cancer has to be considered. Furthermore, neither ionizing radiation, as in mammography, nor the injection of contrast agents, as in magnetic resonance imaging, is needed and of course ultrasound imaging and mammography could be combined to overcome the aforementioned trade-off.
Despite the aforementioned arguments hand-held ultrasound is not suitable for screening because it has a strictly limited field of view and its results strongly depend on the operating physician. High-skilled operators are necessary because differences in anatomy and many possible planes of view have to be considered to find targets of diagnostic significance and to obtain good images of them (Szabo, 2014, chapter 1). However hand-held ultrasound is suitable for diagnostic purposes, especially if a suspicious mass has already been detected, due to the achievable high resolution enabled by the usage of high frequencies up to 50 MHz (Garcia et al., 2005).

Automated breast ultrasound (ABUS) systems with transmission geometry are supposed to be the solution to those problems because they are able to reduce the operator dependence and they enable imaging of the whole breast (Duric et al., 2018). In terms of clinical applicability costs are a crucial factor. Ultrasound examinations are approximately as expensive as mammography and thus much cheaper than magnetic resonance imaging (Szabo, 2014, chapter 1). Although the necessary equipment is more expensive than for hand-held ultrasound, such systems have the potential to reduce the costs of ultrasound examinations due to the fact that no physician is needed for the automated data acquisition.
Many projects are already focusing on automation of evaluating the obtained images using machine learning and artificial intelligence because this could have a positive impact on the sensitivity and specificity and it could further reduce the physician's part of work in screening (Greenleaf, 2018; Sandhu et al., 2018).

According to Sak et al. (2017a), speed of sound in breast tissue approximately linearly depends on the density, as shown in section 3.1.1. According to this, both speed of sound and X-ray absorption reconstructions mainly image the same features based on their density. In contrast to mammography and magnetic resonance imaging, a single ultrasound dataset can be used to reconstruct multiple modalities or parameters, namely speed of sound, acoustic attenuation and reflectivity, which contain complementary information and can be combined in a joint diagnosis (Ruiter et al., 2018a).
The observation of transmission data makes it possible to adopt seismic full-waveform inversion, which is more successful with transmitted than with reflected waves (Pratt, 2018). By using full-waveform tomography it is possible to exceed the resolution limit of ray-based methods determined by neglected diffraction effects (as shown in the figures 2.12, 2.13 and 4.14). Thus, details like the position, shape and margin of lesions, which have a high diagnostic value (see section 2.2.1), can be interpreted more precisely. Highly increased computational costs are still a problem, especially with respect to customary clinical applicability, which desires a reconstruction time of less than 30 minutes (Wiskin et al., 2017). Parallelization of the computation makes it possible to significantly reduce the required computational time but it is restricted by the high costs of the required hardware, nowadays. Further growth of computational power is supposed to solve this issue in the future, though.
In figure 2.11 reconstructions of a breast suffering from an invasive ductal carcinoma are presented to illustrate the characteristics of the introduced imaging modalities, which were used to obtain the shown images. Despite the high resolution, it is hard to detect the carcinoma in mammography due to the low contrast between dense fibrous and cancerous tissue. In contrast to that, it can be clearly identified on the results of magnetic resonance imaging and high-quality ultrasound. Synthetic aperture focusing techniques and an iterative bent-ray tomography algorithm (Li et al., 2009) were used for reflectivity imaging and inversion for speed of sound and attenuation, respectively, using data from the SoftVue ultrasound system (Duric et al., 2014). The reflectivity reconstruction obtained by hand-held ultrasound has the highest resolution but a very limited field of view.

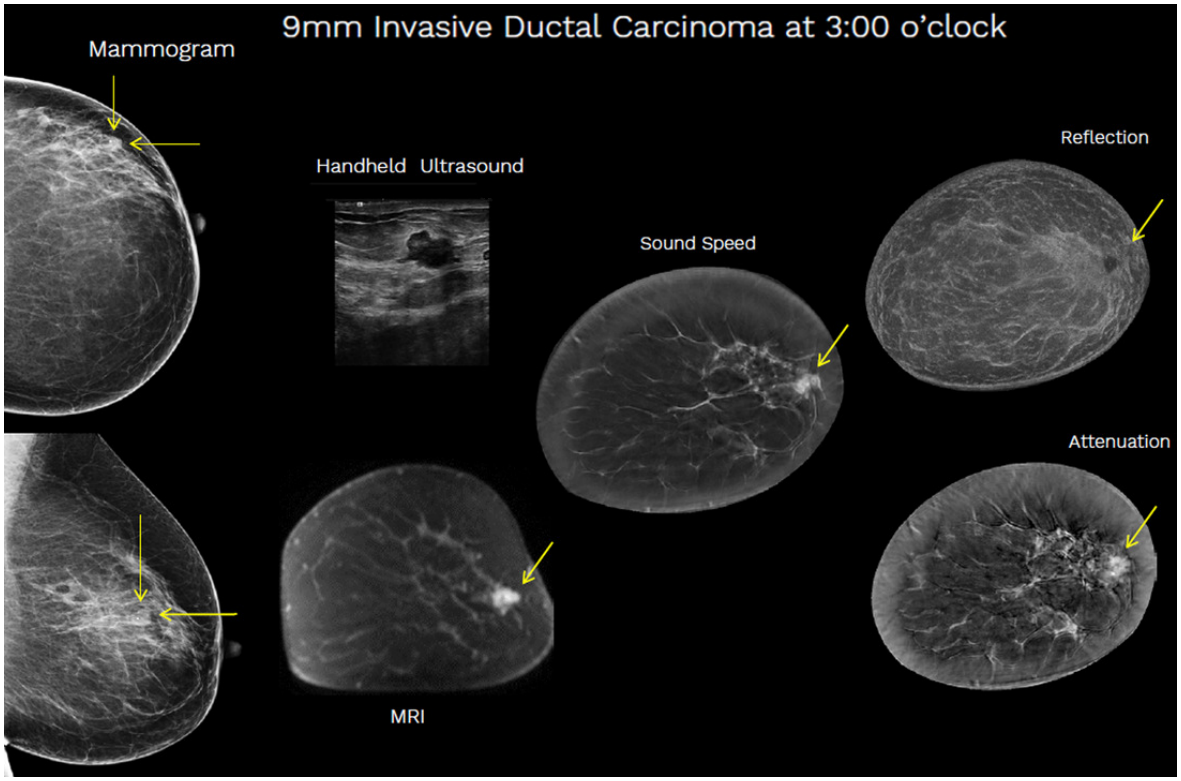

Figure 2.11: Comparison of breast imaging methods based on the example of a breast suffering from an invasive ductal carcinoma. On the left side mammograms in the transverse (top) and sagittal plane (bottom) are shown. In the middle column the results of handheld B-mode ultrasound and magnetic resonance imaging in the coronal plane are shown. On the right side coronal speed of sound, attenuation and reflectivity reconstruction, obtained by iterative bent-ray tomography and synthetic aperture focusing techniques are presented. Data for the latter were acquired with the SoftVue ultrasound tomography system (Delphinus Medical Technologies, 2018).

2.2.3 Ultrasound computed tomography using full-waveform inversion

In the last 40 years full-waveform inversion (FWI) has been developed in the geophysical community with great success, as it is able to provide multi-parameter models of the subsurface in high resolution. The theoretical principles have already been derived in the 1980s (Lailly, 1983; Tarantola, 1984) but it took about ten years until computational power had increased enough to enable first real data applications and it took at least another ten years until it became available for routine use (Pratt, 2018).
In FWI, an initial model is iteratively adjusted by minimizing the misfit between the synthetic and the measured data using e.g. adjoint techniques. By exploiting more information of the measured waveform compared to traveltime tomography, FWI is able to exceed the resolution limit of ray-based methods at the expense of much higher computational costs.

In this section basic terms and concepts of FWI are expected to be known. Readers, who are not familiar with the basics, should first read the detailed introduction to FWI given in section 3.3. Particularities of the application of FWI on medical ultrasound data are presented in section 2.1.3.
Even though there is just a small number of research groups working on ultrasound computed tomography using FWI, not all of their works can be presented. Instead, only the major pioneering contributions will be shown. The selection is made to my best knowledge.

The first successful application of FWI to ultrasound data of breast scans was given by Pratt et al. (2007). Data were obtained using the CURE system (Duric et al., 2007) at the Karmanos Cancer Institute in Detroit, Michigan. The acquisition system consisted of a 20 cm diameter ring, with 256 active, non-beamforming transducers, which surrounded the examined breast in a water tank and could be displaced in vertical direction to obtain approximate 2D datasets of slices in different elevations. Transducers emitting signals with a relatively low, dominant ultrasound frequency of 1.5 MHz were used.
Preprocessing consisted of lowpass filtering the observed data using a corner frequency of 800 kHz, time windowing of the transmitted waves to remove reflected phases and noise prior to the first arrivals, amplitude normalization in common source and common receiver domain to reduce the effects of transducer characteristics and removal of receivers closer than 7.5 cm to the active source, due to crosstalk and high sensitivity of the inversion result from minor timing and location errors in these data. Initial models were created by first-arrival traveltime tomography. All transducer elements were used and for each of them the source signal was estimated with the source time function inversion proposed by Pratt (1999).
Frequency-domain viscoacoustic FWI, using the multiscale approach starting from 400 kHz, was applied to reconstruct speed of sound and attenuation images of two experimental datasets. The whole iterative procedure was performed twice with two

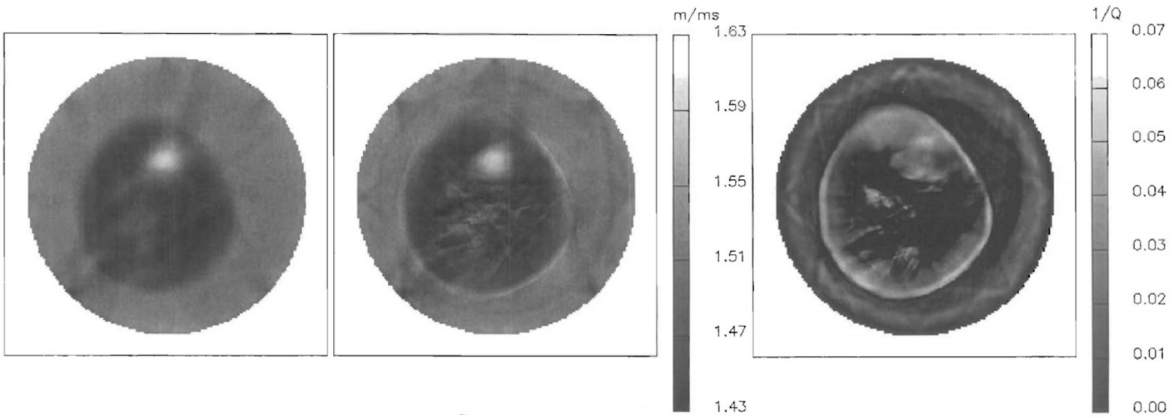

Figure 2.12: Speed of sound and attenuation reconstructions of a clinical dataset. Speed of sound reconstructions obtained by time-of-flight tomography and FWI are shown on the left and in the middle. Attenuation, shown on the right, was reconstructed using exclusively FWI (Pratt et al., 2007).

different wavenumber-space filters to restrict the model updates to features with extensions larger than about two wavelengths or a quarter wavelength, respectively. A physical breast phantom and a clinical example were examined. The results of the latter are shown in figure 2.12. Using FWI instead of time-of-flight tomography leads to a significant increase of resolution, which makes details like the pattern of fibroglandular tissue and the extension of the skin visible.

Subsequently, most of the published papers focused on accelerating FWI algorithms to make them more applicable for clinical usage.
Roy et al. (2010) present and freely provide an efficient time-domain finite-difference parallel implementation of FWI on graphical processing units (GPU) for an arbitrary ultrasound tomography scanner with a circular acquisition geometry. They present the optimal nearly analytic discrete method (ONADM) proposed by Yang et al. (2006), which is able to effectively suppress numerical dispersion caused by too coarse discretization of the wave equation. This allows them to use coarser spatial grids and larger temporal sampling intervals compared to the common finite difference method to speed up the inversion. They further consider the finite velocity of propagating waves to avoid unnecessary updates in the parts of the model where the emitted wave has not yet arrived at a certain time. By assuming the distance between the emitter and a considered region d_0 and a maximum speed of propagation c_{max}, a field will only be updated after time $t_0 = d_0/c_{max}$. Moreover, they present some specific implementation details for GPUs to optimize the memory access and computational complexity.
A frequency domain viscoacoustic FWI algorithm adapted to GPU computational architecture was published by Li et al. (2014). Using a single Tesla C2050 GPU card, they are able to speed up a complete FWI iteration by a factor of 2.5 compared to their implementation on central processing units (CPU) without any GPU support (the specific CPU model is not mentioned). Using additional GPUs can further reduce the

computational time. Performing reconstruction tests with a simple numerical model and very low frequencies from 112 kHz to 364 kHz, they concluded that the resolution achieved with FWI is about one wavelength of the highest used frequency.
Wang et al. (2015) were the first to demonstrate source encoding concepts, originally proposed by Krebs et al. (2009), combined with a stochastic gradient descent method in this specific application. Instead of sequentially propagating the wavefields of each emitter, several or even all sources are encoded to simulate different source signatures and thus can be modeled simultaneously using source encoding. By this, it is possible to reduce the number of forward propagations per iteration. In general, more iterations are needed then but the overall number of required forward simulations and thus the computational cost are reduced. In a numerical test with a simple breast phantom and a ring-shaped transducer array consisting of 256 elements they were able to reduce the computational time by a factor of approximately 60. It should be noted that all 256 transducers were used as sources in this experiment.
Vinard et al. (2014) proposed a method to optimally select the number and locations of the emitters from a preset transducer array in order to reduce the number of redundant wave propagation simulations and thus minimize the required computational time. Note, however, that the usage of fewer sources would lower the acceleration factor obtained by source encoding that was stated in the aforementioned paper.

A very detailed overview about breast ultrasound computed tomography using FWI is given in the dissertation of Sandhu (2015). He includes among others an extensive description of his frequency domain viscoacoustic FWI algorithm using the multiscale approach, necessary signal processing steps and the requirements imposed on initial models to avoid non-convergence. Furthermore he performs synthetic tests for assessing the achievable accuracy and resolution and presents several in vivo results with data measured at only 256 of 2048 available transducer elements of the SoftVue ultrasound system (Duric et al., 2014), with a signal bandwidth centered at 2.75 MHz installed in a transducer ring with 11 cm radius. One special component of the ultrasound system is the so-called SEQUR breast interface, a soft anatomically-formed guide, which contacts the front of the breast to center, shape and steady it during the data acquisition (Delphinus Medical Technologies, 2018). An example of these in vivo results is shown in figure 2.13. Most of the authors and coauthors of the presented papers, including Roy, Li, Sak, Wang and Sandhu, are employees of Delphinus Medical Technologies, Inc., which develops and provides the SoftVue tomographic ultrasound system. The company was founded by Duric and Littrup in 2010, who had previously developed the CURE ultrasound system, e.g. used for data acquisition in the work of Pratt et al. (2007), at Karmanos Cancer Institute, Wayne State University, Detroit. Despite the SoftVue system's standard use of an iterative bent-ray tomography algorithm (Li et al., 2009), Delphinus is very interested in FWI techniques, which is indicated by their very intensive research activities in this field. Inter alia, Sak et al. (2017b) were the first to use results of ultrasound computed tomography with FWI in a clinical study, in which breast density changes among women undergoing tamoxifen therapy were assessed.

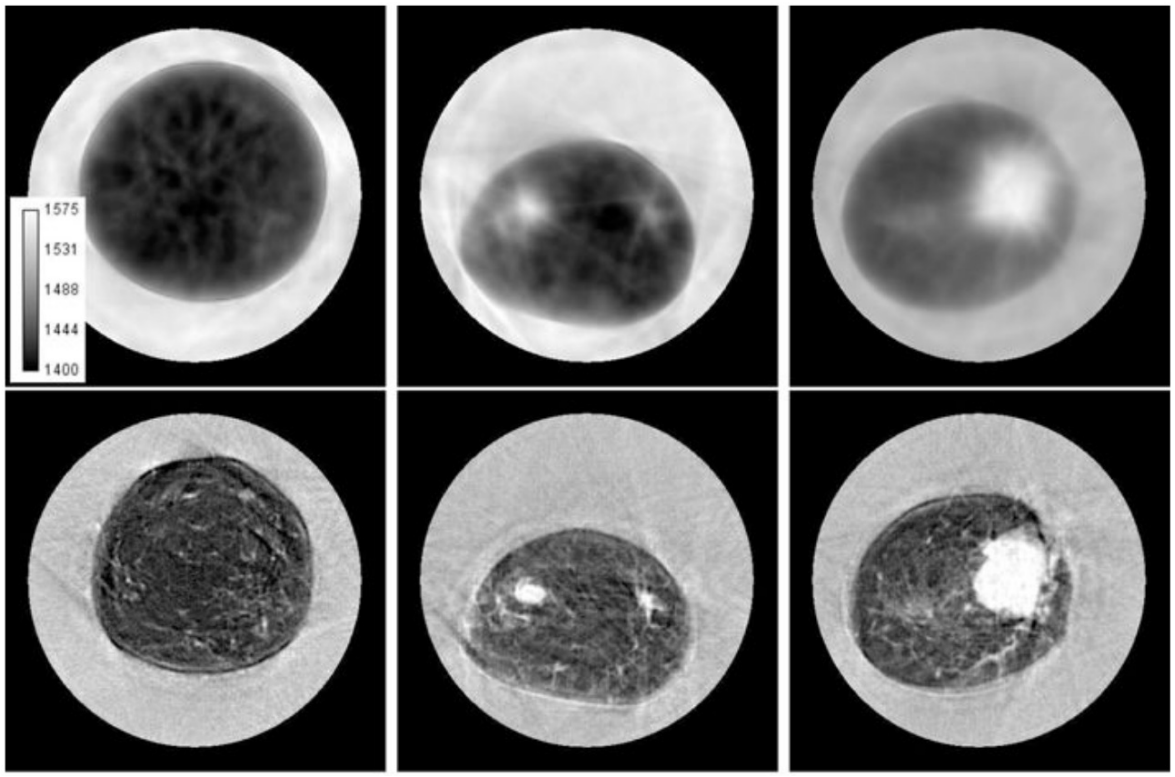

Figure 2.13: Comparison of speed of sound reconstructions using traveltime tomography (upper row) and FWI (lower row). Data were obtained using the SoftVue ultrasound system (Duric et al., 2014). From left to right breasts with a fine pattern of fibroglandular tissue, a tumor with a diameter of 1 cm and a tumor with a diameter of 4 cm are shown. Gray scale values correspond to speed of sound values from 1400 m/s to 1575 m/s as specified in the colorbar in the upper left corner (Sandhu, 2015).

Another early groundbreaking work, based on the patent of Borup et al. (1999), was published by Wiskin et al. (2007). In contrast to the approaches used in all other presented papers and this thesis, they use a tomographic ultrasound device with planar transducer arrays to generate approximate planar waves and do not solve the full wave equation in a strict sense. Instead, a parabolic approximation of the acoustic wave equation in the frequency domain, which describes waves primarily propagating in a preferred direction as is given for planar waves, is used to significantly speed up the forward simulations.
In the latest paper Wiskin et al. (2017) generalize their earlier 2D algorithm to a full 3D inversion algorithm, emphasize the necessity of 3D algorithms to suppress artifacts caused by the 2D approximation and estimate the achieved accuracy by inverting ultrasound data from various physical phantoms with known properties.
Ultrasound data with a frequency content of about 0.3 MHz to 1.3 MHz are acquired with an automated breast ultrasound system of quantitative transmission (QT) Ultrasound Labs using two opposite rectangular planar transducer arrays, each consisting of 1536 transducer elements, for transmitting and receiving the sound waves.

The whole system is rotatable and vertically displacable to enable full illumination of the breast. A detailed description of the system is given in Wiskin et al. (2012). Using the parabolic approximation of the viscoacoustic wave equation for fast forward simulations, the multiscale approach, a conjugate gradient method and 2D initial models for each level, obtained by time-of-flight tomography, they first use their 2D waveform tomography algorithm to obtain a stack of 2D speed of sound and attenuation models. These 2D models are concatenated to 3D models, which are subsequently used as initial models for the 3D reconstruction algorithm. It should be noted that no full 3D tomographic transducer geometry is used for data acquisition. By neglecting scattered and reflected phases, even in the 3D case, only the transmitted part of a wavefield is used.
Results for several physical phantoms prove a high accuracy of the reconstructed quantitative values, especially for speed of sound. The relative deviations between the means of the distributions of inverted speed of sound and attenuation and the specifications given by the phantoms manufacturers are in the order of 10^{-3} and 10^{-2} respectively. The relative standard deviations are in the order of 10^{-3} to 10^{-2} for speed of sound and 10^{-1} for attenuation.

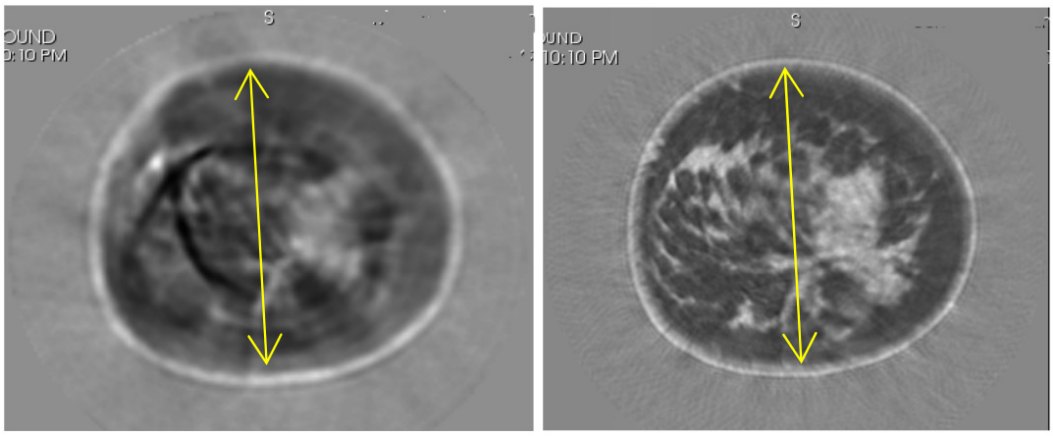

Figure 2.14: Comparison of in vivo coronal speed of sound reconstructions of a volunteer. The image on the left, showing artifacts, was created using a 2D inversion algorithm and has fallen into a local minimum. The right-hand image was reconstructed with a 3D algorithm and seems to correctly show the pattern of fibroglandular tissue (light gray) in the adipose tissue (dark gray). Grayscale speed of sound values vary from 1350 m/s (black) to 1600 m/s (white). Yellow arrows are 12.5 cm for reference (Wiskin et al., 2017).

A comparison of in vivo coronal speed of sound reconstructions obtained with their 2D and 3D algorithms show that the 2D approximation lowers the achievable resolution and yields low-speed artifacts (see figure 2.14) due to the incorrect 2D inversion of phases scattered at objects outside of the reconstructed plane, whose increased traveltimes are considered to be caused by low velocity anomalies instead of extended travelpaths. Strongest artifacts occur close to the chest wall and skin, especially near the nipples, because strong reflectors are non-orthogonally oriented to the reconstruc-

tion plane in these regions. The complementary effect of scattering energy out of plane yields overestimations of the attenuation reconstructed with 2D algorithms because in this case the associated energy loss is interpreted as attenuation.

The first experiments that use 3D FWI algorithms solving the full wave equation were published by Sandhu et al. (2017) and Agudo et al. (2018). Both are limited to synthetic tests and use 2D acquisition geometries mimicking transducer rings. They analyze the consequences of using a 2D algorithm to invert 3D data and confirm the previously described effects.
Agudo et al. (2018) use a time domain finite-difference viscoacoustic algorithm. In figure 2.15 synthetic ultrasound data generated with a 2D and 3D forward simulation code using 250 transducers in a circular array located in the shown 2D slice of the 3D numerical breast phantom are presented. Considerable differences are clearly visible in the transmitted phases measured at transducers opposite of the source marked with a black circle. Especially these data have a huge impact on the inversion's result, which points out the importance of correctly simulating them.
The 3D data of 50 transducers are inverted using a 2D and a 3D FWI algorithm and homogeneous initial models with the properties of water. The speed of sound reconstructions and the true model are shown in the bottom row of figure 2.15. In both cases the multiscale approach is used in a frequency range from 150 kHz to 1 MHz. It is shown that starting at such low frequencies makes it even possible to use homogeneous initial models without suffering from cycle-skipping. On the one hand, the achieved accuracy is significantly improved by using the 3D inversion, which is well visible at the reconstructions of the spherical inclusions and interface between fat (dark blue) and fibroglandular tissue (light red). On the other hand, using the 3D algorithm is not able to prevent overestimating the size of the inclusion denoted by 3 and the occurrence of the artifacts denoted by 1 and 2 (see image (c) in figure 2.15), which are caused by waves propagating slightly off-plane. Either vertically focused transducers or full 3D data acquisition (see figure 2.4), as is the case in the 3D-USCT system developed by Ruiter et al. (2018a), are supposed to solve this problem.

Finally, the most important points, in which all presented papers agree, are very briefly summarized: Using FWI instead of ray-based methods can significantly increase the resolution and accuracy of speed of sound and attenuation reconstructions. Crucial factors for convergence are the availability of low frequency data and appropriate initial models. For FWI of 3D datasets, as is always the case for measured data, a 3D algorithm should be used to prevent the occurrence of artifacts and a significant loss of resolution. However, performing 3D FWI dramatically increases the computational costs, which is the most restrictive factor for customary applicability, even in 2D.

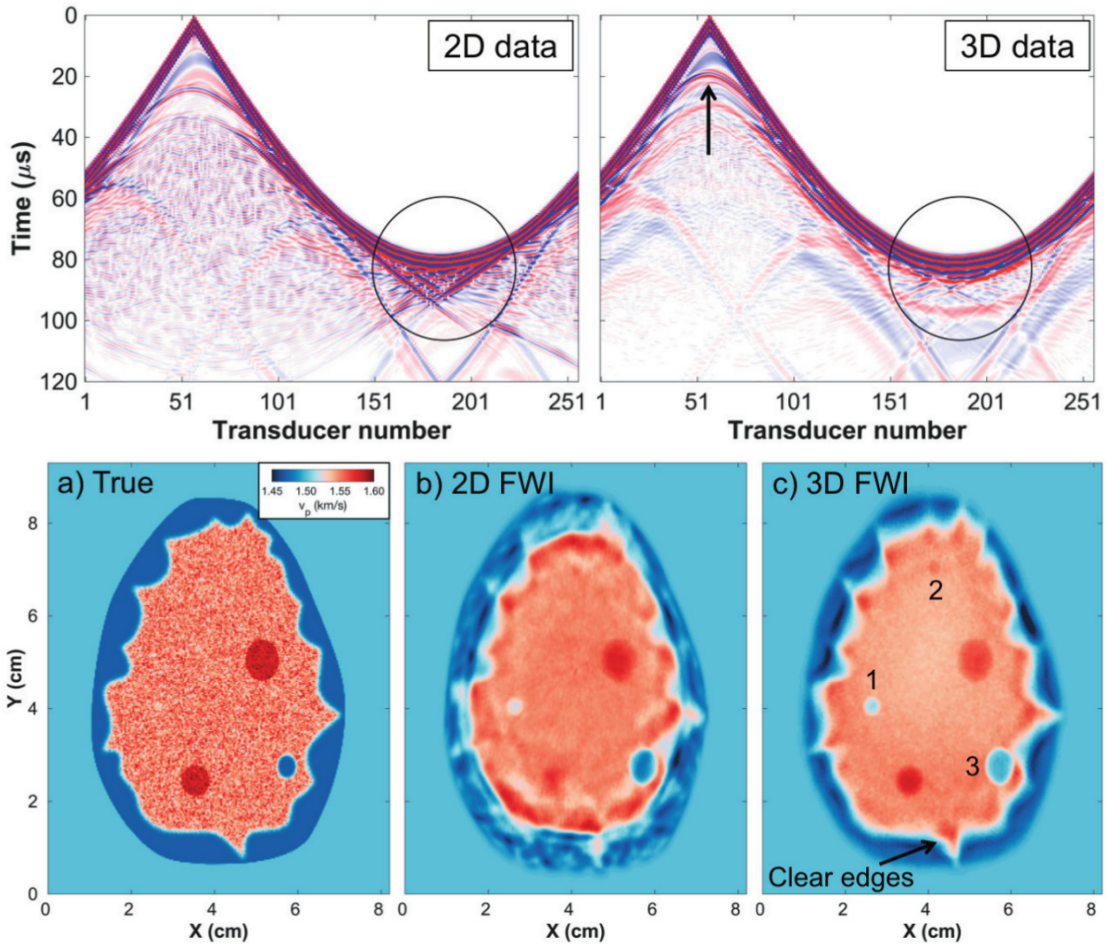

Figure 2.15: Comparison of 2D and 3D FWI. In the upper row modeled data for a source in a 2D circular transducer array using a 2D (left) and 3D (right) wave propagation code. In the lower row a 2D slice of the true 3D numerical breast phantom (a) and the speed of sound reconstructions after 2D (b) and 3D FWI (c) of a subset of the above shown 3D dataset are presented (Agudo et al., 2018).

Chapter 3

Methodology

In this chapter I present the theoretical principles of acoustic and viscoacoustic wave propagation. In section 3.2 I introduce the finite-differences method, which allows us to numerically solve differential equations to simulate wave propagation. A special focus is on the spatial discretization and temporal sampling of the wavefields and the associated numerical dispersion. Due to the large number of propagated wavelengths in medical ultrasound, the typical criteria to limit numerical dispersion in seismics are not sufficient.
In section 3.3 an overview of time-domain full-waveform inversion with a focus on the optimization strategy used in this work is given.
Lastly, I propose a semi-analytical method to simulate the effects of the finite size and geometry of transducers on the generated and received waveforms in dependence of the radiation or incidence angle, respectively.

In the interest of readability vectors and matrices are given in boldface.

3.1 Physics of wave propagation

The acoustic approximation of the elastic wave equation is used to describe the propagation of longitudinal compressional waves in media where no shear stresses and thus no shear waves occur. This is the case in fluids, gases and plasma. However, it is reasonable to use the acoustic approximation in breast tissue due to the large percentage of water, which leads to elastic effects being negligible. Moreover, the propagation medium is assumed to be isotropic.

In this section I derive the two-dimensional acoustic wave equation in the velocity-stress formulation, where wave propagation is described by a system of first-order partial differential equations. By introducing the generalized standard linear solid the acoustic wave equation is extended in order to take anelastic attenuation into account. Furthermore, I introduce a formula to convert typical quantities used to describe attenuation in seismics and medical ultrasound into each other.

3.1.1 Acoustic wave equation

This section follows the derivations of the elastic wave equation given in Aki and Richards (2002) and Müller (2007) and adapts them to the acoustic case.
The equilibrium condition for an arbitrary volume in a deformable body state that the sum of body force density $\boldsymbol{f}$ and surface force density, described by the stress tensor $\boldsymbol{\sigma}$, and the resulting angular moment must be equal to zero. They yield the equation of motion in Einstein summation convention

$$\rho \frac{\partial^2 u_i}{\partial t^2} = \frac{\partial \sigma_{ij}}{\partial x_j} + f_i \ , \tag{3.1}$$

with the components u_i of the displacement vector $\boldsymbol{u}$, the mass density ρ, time t and position vector $\boldsymbol{x}$.

In linear elasticity theory the stress-strain relationship is described by the linear generalized Hooke's Law

$$\sigma_{ij} = M_{ijkl} \epsilon_{kl} \ . \tag{3.2}$$

M_{ijkl} are elasticity constants and

$$\epsilon_{kl} = \frac{1}{2} \left(\frac{\partial u_k}{\partial x_l} + \frac{\partial u_l}{x_k} \right) \tag{3.3}$$

denote the components of the strain tensor $\boldsymbol{\epsilon}$. All indices range from 1 to 3 and correspond to the three spatial axes x, y and z defined by a three-dimensional Cartesian coordinate system.

Assuming isotropic and acoustic media, only one elastic parameter remains and equation 3.2 can be written as

$$\sigma_{ij} = \lambda \Theta \delta_{ij} \ , \tag{3.4}$$

where λ is a Lamés parameter,

$$\Theta = \mathrm{trace}(\boldsymbol{\epsilon}) = \epsilon_{xx} + \epsilon_{yy} + \epsilon_{zz} \tag{3.5}$$

is the cubic dilatation and

$$\delta_{ij} = \begin{cases} 1 & \text{for } i = j \\ 0 & \text{otherwise} \end{cases} \tag{3.6}$$

is the Kronecker symbol or unit tensor.

Substituting the displacement velocity $\boldsymbol{v} = \frac{\partial \boldsymbol{u}}{\partial t}$, the relation between the hydrostatic pressure P and the stress tensor in an acoustic medium

$$\sigma_{ij} = -P \, \delta_{ij} \tag{3.7}$$

and equation 3.3 in equations 3.1 and 3.4 yields a system of four first-order differential equations, called the velocity-stress formulation of the acoustic wave propagation

$$\begin{aligned} \frac{\partial v_i}{\partial t} &= -\frac{1}{\rho}\frac{\partial P}{\partial x_i} \\ \frac{\partial P}{\partial t} &= -\lambda\frac{\partial v_i}{\partial x_i} \end{aligned} \quad , \tag{3.8}$$

where the external body force density $\boldsymbol{f}$ is set to zero.

Moreover, in the acoustic approximation λ corresponds to the bulk modulus k

$$k = \lambda \tag{3.9}$$

and thus for the relation between the elasticity constant, the density ρ and the velocity of pressure waves or speed of sound c holds

$$c = \sqrt{\frac{k}{\rho}} = \sqrt{\frac{\lambda}{\rho}} \iff \lambda = \rho\, c^2 \ . \tag{3.10}$$

According to Sak et al. (2017a), the bulk modulus for breast tissues approximately scales as the cube of density, yielding a linear relation between tissue density and speed of sound

$$c \propto \rho \ . \tag{3.11}$$

Using equation 3.9, 3.10 and the two-dimensional approximation (assume all properties to be constant in z direction), in which partial derivatives with respect to z vanish, the system of coupled first-order differential equations 3.8 is reduced to the three following equations

$$\begin{aligned} \frac{\partial v_x}{\partial t} &= -\frac{1}{\rho}\frac{\partial P}{\partial x} \\ \frac{\partial v_y}{\partial t} &= -\frac{1}{\rho}\frac{\partial P}{\partial y} \\ \frac{\partial P}{\partial t} &= -\rho\, c^2 \left(\frac{\partial v_x}{\partial x} + \frac{\partial v_y}{\partial y}\right) \end{aligned} \quad . \tag{3.12}$$

They can be solved numerically to simulate wave propagation for a given spatial distribution of density ρ and speed of sound c.
The equations 3.1 and 3.2, and consequently 3.12, are ony valid under the assumption of infinitesimally or in practice appropriately small deformations. By using acoustic approximations in many parts of the derivation, the absence of shear stresses or propagation of shear waves is assumed.

3.1.2 Viscoacoustic wave equation

To describe wave propagation in highly attenuative breast tissue accurately, anelastic attenuation, yielding dispersion and conversion of motion energy into heat, has to be considered. Propagating waves not only become smaller in amplitude, but their waveforms also change shape (Szabo, 2014, chapter 4), which is of crucial importance to correctly simulate waveforms, e.g. during FWI.

Describing attenuation in viscoacoustic media
In seismics, attenuation is usually described by the dimensionless quality factor Q, while in medical ultrasound imaging the energy or amplitude loss per distance per frequency $\hat{\alpha}$, specified in $\mathrm{dB\,cm^{-1}\,MHz^{-y}}$, is preferred. The scalar y is a material specific constant specifying the frequency dependence of the attenuation.
Sometimes the latter is expressed in terms of nepers per centimeter. The conversion from $\hat{\alpha}_{Np}$ in $\mathrm{Np\,cm^{-1}\,MHz^{-y}}$ to $\hat{\alpha}$ in $\mathrm{dB\,cm^{-1}\,MHz^{-y}}$ is given by

$$\hat{\alpha} = 8.686\,\hat{\alpha}_{Np}\ . \tag{3.13}$$

In the following, I derive a formula for the conversion from $\hat{\alpha}$ to Q based on the exponential law

$$P(x) = P_0\,e^{-\alpha x} \tag{3.14}$$

describing spatial changes of the amplitude or pressure $P(x)$ of a plane wave propagating in x-direction with the initial amplitude P_0 and the attenuation coefficient α, specified in $\mathrm{m^{-1}}$ (Szabo, 2014, chapter 4). I further use the definition of decibel based on the ratio of two amplitudes

$$20\log_{10}\left(\frac{P_0}{P(x)}\right) = \hat{\alpha} f^y x\ , \tag{3.15}$$

where f denotes the frequency and x denotes the propagation distance. Substitution of equation 3.14 yields

$$\alpha = \frac{\ln 10}{20} f^y \hat{\alpha}\ . \tag{3.16}$$

In the following, I assume $Q \gg 1$. Despite breast tissue is highly attenuative, this assumption is valid for relatively low ultrasound frequencies typically used in FWI (as shown in figure 4.2 in section 4.1). By using the approximation for $Q \gg 1$ given by Toksöz and Johnston (1981)

$$Q = \frac{\pi f}{c\,\alpha} \tag{3.17}$$

and equation 3.16 I obtain

$$Q = \frac{20}{\ln 10}\frac{\pi}{c\,\hat{\alpha}} f^{1-y}\ . \tag{3.18}$$

For $y = 1$ this becomes equal to the conversion proposed by Pratt (2008). This case corresponds to a linear dependence of α on the frequency f or constancy of the quality factor Q, which is usually assumed in the typical seismic frequency range. In contrast to that, an arbitrary power law dependence on frequency of y-th degree of α, as

considered in equation 3.18, is often used in medical ultrasound (see figure 4.2, sec 4.1).

To describe an arbitrary frequency dependence of the attenuation in a medium, I use a rheological model called generalized standard linear solid (GSLS) (Liu et al., 1976). It consists of a spring, called Hooke body, and L parallely connected Maxwell bodies. Each Maxwell body consists of a Hooke and a Newton body in series. While the Hooke elements describe the pure acoustic properties, the Newton bodies characterize the viscosity of the medium. Each combination of a Maxwell body and the separate Hooke element represents one individual relaxation mechanism.
A GSLS with $l = \{1, ..., L\}$ can be quantified by the relaxed bulk modulus k_r and two additional parameters per relaxation mechanism, namely the relaxation times $\tau_{\sigma,l}$ and retardation times $\tau_{\epsilon,l}$. Blanch et al. (1995) suggested to replace the L dependent retardation times by one L independent parameter

$$\tau := \sum_{l=1}^{L} \frac{\tau_{\epsilon,l}}{\tau_{\sigma,l}} - 1 \tag{3.19}$$

to reduce the number of variables and, thus, reduce the memory requirements and computational costs when numerically solving the viscoelastic or viscoacoustic wave equation. By using this simplification, for the quality factor of a GSLS holds

$$Q(\omega, \tau_{\sigma,l}, \tau) = \frac{1 + \sum\limits_{l=1}^{L} \frac{\omega^2 \tau_{\sigma,l}^2}{1+\omega^2 \tau_{\sigma,l}^2} \tau}{\sum\limits_{l=1}^{L} \frac{\omega \tau_{\sigma,l}}{1+\omega^2 \tau_{\sigma,l}^2} \tau} , \tag{3.20}$$

where $\omega = 2\pi f$ denotes the angular frequency. The application of a least-squares optimization algorithm on this equation makes it possible to approximate any desired frequency dependence of Q, within a limited frequency range, by determining an appropriate τ and L relaxation times $\tau_{\sigma,l}$ or angular relaxation frequencies $\omega_l = \frac{1}{\tau_{\sigma,l}}$ (Blanch et al., 1995; Bohlen, 2002).
Usually τ, which is given by

$$\tau = \left(\sum_{l=1}^{L} \frac{\omega/\omega_l}{1 + \omega^2/\omega_l^2} Q \right)^{-1} , \tag{3.21}$$

is used rather than Q in the implementation of attenuation (Kurzmann, 2012).
The frequency-dependent dispersion $c(\omega)$ for $Q \gg 1$ in terms of ω_l and τ is given by

$$c(\omega) = c_{ref} \left(\sqrt{1 + \sum_{l=1}^{L} \frac{\omega^2 \tau_{\sigma,l}^2}{1 + \omega^2 \tau_{\sigma,l}^2} \tau} - \sqrt{1 + \sum_{l=1}^{L} \frac{\omega_0^2 \tau_{\sigma,l}^2}{1 + \omega_0^2 \tau_{\sigma,l}^2} \tau} \right) , \tag{3.22}$$

providing no dispersion at the angular reference frequency ω_0. The reference velocity c_{ref} is defined as the phase velocity $c(\omega)$ for $\omega = \omega_0$. It is suggested to define ω_0 as the angular peak frequency of the source wavelet or measured data (Kurzmann, 2012).

Using this notation and the assumption $Q \gg 1$, the relaxed frequency-dependent bulk modulus k_r can be computed by (Kurzmann, 2012)

$$k_\mathrm{r} = \rho\, c_{ref}^2 \left(1 + \sum_{l=1}^{L} \frac{\omega_0^2/\omega_l^2}{1+\omega_0^2/\omega_l^2}\tau\right)^{-1} \quad . \tag{3.23}$$

Viscoacoustic wave equation

In viscoacoustic media the stress does not only depend on the current strain but on the strain history. This can be described by replacing the multiplication in the stress-strain relation of acoustic media (see equation 3.2) with a convolution (Christensen, 1982)

$$\sigma_{ij} = M_{ijkl} * \epsilon_{kl} \ , \tag{3.24}$$

where $\boldsymbol{M}(t)$ becomes a complex-valued function of time t. Due to causality, it must hold $\boldsymbol{M}(t) = 0$ for $t < 0$ (Forbriger and Friederich, 2005).

As proposed by Carcione et al. (1988) and Robertsson et al. (1994), I introduce memory variables r_l in order to avoid the convolution and obtain the following system of $3+L$ first-order differential equations describing two-dimensional viscoacoustic wave propagation:

$$\begin{aligned}
\frac{\partial v_x}{\partial t} &= -\frac{1}{\rho}\frac{\partial P}{\partial x} \\
\frac{\partial v_y}{\partial t} &= -\frac{1}{\rho}\frac{\partial P}{\partial y} \\
\frac{\partial P}{\partial t} &= -k_r \left(\frac{\partial v_x}{\partial x} + \frac{\partial v_y}{\partial y}\right)(1 + L\,\tau) - \sum_{l=1}^{L} r_l \\
\frac{\partial r_l}{\partial t} &= -\frac{1}{\tau_{\sigma,l}}\left(k_r\,\tau\left(\frac{\partial v_x}{\partial x} + \frac{\partial v_y}{\partial y}\right) + r_l\right) \text{ with } l = \{1, ..., L\}
\end{aligned} \tag{3.25}$$

Please take note that Einstein summation notation is not used in these equations and, thus, no sum over l has to be computed.

3.2 Finite-difference forward modeling

In full-waveform inversion (FWI) the system of differential equations 3.12 or 3.25 has to be solved numerous times to simulate wave propagation. While there exist analytical solutions for simple cases, e.g. homogeneous propagation media (Rienstra and Hirschberg, 2004), wave propagation in complex models must be simulated numerically. In this work the software IFOS2D (Inversion of Full Observed Seismograms) is used, in which wave modeling is performed with a time-domain finite-difference (FD) method originally developed by Bohlen (1998). The forward code is parallelized by dividing the model into several equally sized subdomains, which are distributed among different CPUs, to reduce memory consumption and computation time (domain decomposition). Using the FD method, the partial derivatives in the velocity-stress formulation of the wave equation are approximated with discrete FD operators to obtain an explicit time-stepping scheme. Therefore, it is necessary to discretize the spatial and temporal domain.

3.2.1 Discretization

A rectangular grid with equidistant spacing Δh is used to discretize the spatial domain. The coordinates of an arbitrary grid point (i, j) are given by

$$\begin{aligned} x &= i\,\Delta h \\ y &= j\,\Delta h \end{aligned} \quad . \tag{3.26}$$

Time is similarly discretized with constant timesteps Δt yielding

$$t = n\,\Delta t \ , \tag{3.27}$$

where t is the time at the n-th timestep. This leads us to the notation

$$P(x, y, t) = P(i\,\Delta h, j\,\Delta h, n\,\Delta t) = P^{[n]}_{[i,j]} \tag{3.28}$$

for discretized wavefield variables.

I follow the staggered-grid approach (Virieux, 1986; Levander, 1988), where half integral grid points are introduced. As shown in figure 3.1, the pressure P and memory variables r_l are computed at integral grid points and half time steps, while the components of the particle velocity v_x and v_y are computed at half integral grid points and full time steps. Time-independent viscoacoustic parameters, namely density ρ, speed of sound c and τ, which quantifies the attenuation, are defined on integral grid points. However, the calculation of the components of the particle velocity v_x and v_y additionally requires the density on half integral spatial grid points. Therefore, the density has to be arithmetically averaged (Bohlen and Saenger, 2006):

$$\begin{aligned} \bar{\rho}_{[i+\frac{1}{2},j]} &= \frac{\rho_{[i,j]} + \rho_{[i+1,j]}}{2} \\ \bar{\rho}_{[i,j+\frac{1}{2}]} &= \frac{\rho_{[i,j]} + \rho_{[i,j+1]}}{2} \end{aligned} \tag{3.29}$$

In the following, the FD approximations of first order derivatives, as they appear in the velocity-stress formulations of the acoustic and viscoacoustic wave equations, are introduced. By doing this, I will be able to obtain an explicit time-stepping scheme to simulate wave propagation. This is exemplarily shown by approximating the spatial and temporal derivatives with second order accuracy in the differential equation of the velocity component v_x in the viscoacoustic case.
I derive the FD operators by applying a Nth-order Taylor series expansion of an arbitrary function $f(\xi)$

$$f(\xi) = \sum_{n=0}^{N} \frac{f^{(n)}(\xi_0)}{n!}(\xi - \xi_0)^n \ , \tag{3.30}$$

where $f^{(n)}(\xi_0)$ denotes the n-th derivative of f evaluated at the point ξ_0 and $n!$ denotes the factorial of n.
For $N = 1$ and discrete points $\xi = \xi_0 + i\,\Delta\xi$ we obtain

$$f(\xi_0 + i\,\Delta\xi) = f(\xi_0) + \frac{\partial f(\xi_0)}{\partial \xi} i\,\Delta\xi + \mathcal{O}(\Delta\xi^2) \tag{3.31}$$

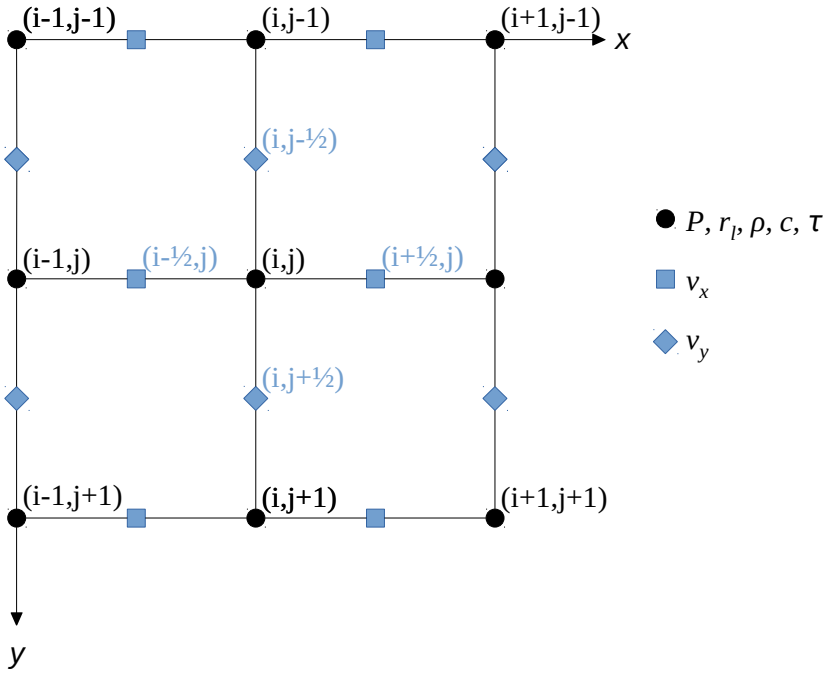

Figure 3.1: Standard staggered grid in Cartesian coordinates for two-dimensional viscoacoustic finite-difference wave modeling. Black dots represent integral grid points, where the pressure P and memory variables r_l are computed at half time steps. The viscoacoustic parameters, namely the density ρ, speed of sound c and τ, which quantifies the attenuation, are also defined on these full spatial grid points. The blue squares and diamonds represent half integral grid points, where the components of the particle velocity v_x and v_y are computed at full time steps.

with $\mathcal{O}$ specifying the order of the truncation error. Setting $i = 1$, ignoring higher orders and rearranging the equation yields the forward FD operator

$$\frac{\partial f(\xi_0)}{\partial \xi} = \frac{f(\xi_0 + \Delta\xi) - f(\xi_0)}{\Delta\xi} + \mathcal{O}(\Delta\xi) \ . \tag{3.32}$$

Analogous procedure with $i = -1$ yields the backward FD operator

$$\frac{\partial f(\xi_0)}{\partial \xi} = \frac{f(\xi_0) - f(\xi_0 - \Delta\xi)}{\Delta\xi} + \mathcal{O}(\Delta\xi) \ . \tag{3.33}$$

Calculating the arithmetic mean of forward and backward operator yields

$$\frac{\partial f(\xi_0)}{\partial \xi} = \frac{f(\xi_0 + \Delta\xi) - f(\xi_0 - \Delta\xi)}{2\Delta\xi} + \mathcal{O}(\Delta\xi^2) \ , \tag{3.34}$$

which represents the central FD operator second order accurate in $\Delta\xi$. By using the central operator instead of the forward or backward operator, the approximation of the partial derivative converges quadratically instead of linearly as $\Delta\xi \to 0$ (Ladyzhenskaya, 1985).

The staggered grid enhances the precision and stability of the FD simulation (Liu and Sen, 2009). Hence, the second-order central FD operator of the staggered grid is given by

$$\frac{\partial f(\xi_0)}{\partial \xi} = \frac{f(\xi_0 + \frac{1}{2}\Delta\xi) - f(\xi_0 - \frac{1}{2}\Delta\xi)}{\Delta\xi} + \mathcal{O}(\Delta\xi^2) \ . \tag{3.35}$$

Moreover, the accuracy can be increased by expanding the Taylor series, shown in equation 3.30, to higher orders. Considering terms of order N results in central FD operators of $2N$th-order accuracy, which include N neighboring points in positive and negative directions, respectively. Using higher-order FD operators makes it possible to use a coarser discretization without losing accuracy, which allows to reduce the total number of grid points and thus the computational costs. In IFOS2D it is possible to use FD operators second-order accurate in time and higher-order accurate in space.

Approximating the spatial and temporal derivatives in the differential equation of the velocity component v_x in the viscoacoustic wave equation 3.25 with the FD operator shown in equation 3.35 yields

$$\frac{v^{[n+1]}_{x,[i+\frac{1}{2},j]} - v^{[n]}_{x,[i+\frac{1}{2},j]}}{\Delta t} = -\frac{1}{\bar{\rho}_{[i+\frac{1}{2},j]}} \frac{P^{[n+\frac{1}{2}]}_{[i+1,j]} - P^{[n+\frac{1}{2}]}_{[i,j]}}{\Delta h} \ , \tag{3.36}$$

where $\bar{\rho}_{[i+\frac{1}{2},j]}$ denotes the density on half integral grid points approximated by equation 3.29. Rearrangement provides the explicit FD time-stepping scheme for v_x:

$$v^{[n+1]}_{x,[i+\frac{1}{2},j]} = v^{[n]}_{x,[i+\frac{1}{2},j]} - \frac{1}{\bar{\rho}_{[i+\frac{1}{2},j]}} \frac{\Delta t}{\Delta h} \left(P^{[n+\frac{1}{2}]}_{[i+1,j]} - P^{[n+\frac{1}{2}]}_{[i,j]} \right) \ . \tag{3.37}$$

Replacement of the derivatives in the remaining differential equations of the wave equation in velocity-stress formulation will result in similar FD schemes, where the wavefield variables at future timesteps can be calculated with values from the previous ones. A complete list of FD time-stepping schemes in the acoustic and viscoacoustic case, derived with second-order central FD operators in time and space, is shown in Kurzmann (2012). It has to be noted that in his work, as well as in IFOS2D, the relation between the stress tensor $\boldsymbol{\sigma}$ and the hydrostatic pressure P is not defined in the conventional way as shown in equation 3.7, but with a positive sign as $\sigma_{i,j} = P\,\delta_{i,j}$. By defining the normal vector of a unit volume with the opposite direction, the bulk modulus k is also defined with the opposite sign ($k < 0$). This, consequently, leads to slightly different formulations of the acoustic and viscoacoustic wave equation and time-stepping schemes. Nevertheless, the resulting wave equations and FD schemes are equivalent to those presented in this chapter and can easily be transformed into each other by changing P to $-P$. Moreover, it has to be noted that the staggered grid used in Kurzmann (2012) is shifted by half a time step.

3.2.2 Initial conditions and boundary layers

The propagation medium is supposed to be in equilibrium at $t = 0$, which yields

$$\begin{aligned} P(x, y, t = 0) &= \dot{P}(x, y, t = 0) = 0 \\ v_x(x, y, t = 0) &= \dot{v}_x(x, y, t = 0) = 0 \\ v_y(x, y, t = 0) &= \dot{v}_y(x, y, t = 0) = 0 \end{aligned} \tag{3.38}$$

as initial conditions in the acoustic case. The viscoacoustic case additionally requires

$$r_l(x, y, t = 0) = \dot{r}_l(x, y, t = 0) = 0 \qquad \text{with } l = \{1, ..., L\} \ , \tag{3.39}$$

where L is the number of considered relaxation mechanisms.

An effective method to suppress artificial reflections from the outer boundaries of the model is the convolutional perfectly matched layer (C-PML) method as proposed by Komatitsch and Martin (2007). It corresponds to a coordinate transformation, which maps the coordinates at the model boundaries to complex numbers in order to let waves decay exponentially. The implementations in the acoustic and viscoacoustic case are explained by Kurzmann (2012) in great detail.
In contrast to classical geophysical applications no free surface conditions are needed.

3.2.3 Source implementation

N_{src} explosive point sources with an omnidirectional radiation pattern at the discrete coordinates

$$\begin{aligned} x_s &= i_s \, \Delta h \\ y_s &= j_s \, \Delta h \end{aligned} \qquad \text{with } s = \{1, ..., N_{\text{src}}\} \tag{3.40}$$

are considered. To excite waves, the source signal S_s, specified as a pressure signal, is added at each timestep to the current pressure P at the respective source location:

$$P^{[n]}_{[i_s, j_s]} = P^{[n]}_{[i_s, j_s]} + S^{[n]}_s \qquad \text{with } s = \{1, ..., N_{\text{src}}\} \tag{3.41}$$

3.2.4 Numerical dispersion and instability

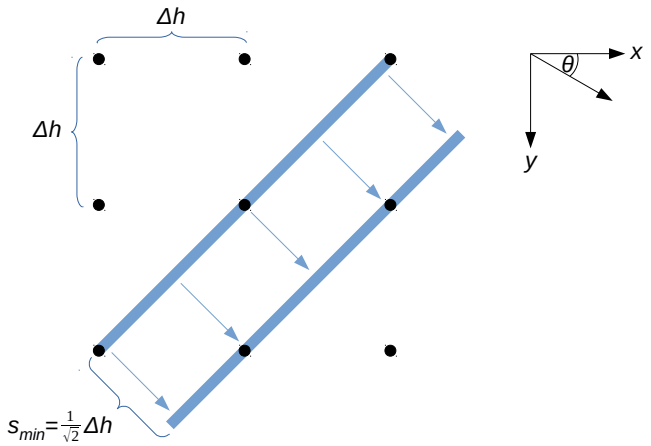

Figure 3.2: Blue lines represent a plane wave propagating in the direction specified by blue arrows ($\theta = 45°$). Black dots represent grid points within a rectangular grid with equidistant spacing Δh.

Table 3.1: Factor γ in the Courant-Friedrichs-Lewy criterion and factor n in the criterion to limit spatial dispersion proposed by Köhn (2015) for different FD orders.

FD order	γ	n
2nd	1	12
4th	7/6	8
6th	149/120	6
8th	2161/1680	5

According to section 3.2.1, space and time must be discretized to enable the simulation of wave propagation with FD methods. In the following, I investigate how the spatial and temporal sampling intervals Δh and Δt have to be chosen.

Courant et al. (1928) proposed the Courant-Friedrichs-Lewy criterion

$$\Delta t \leq \frac{\Delta h}{\gamma \sqrt{D}\, c_{\max}} \,, \tag{3.42}$$

which assures that a plane wave does not propagate further than the minimum distance $s_{\min}$ between two grid points during one time step. Simple geometrical considerations yield the minimum distance $s_{\min} = \frac{\Delta h}{\sqrt{D}}$, where D denotes the number of considered spatial dimensions. The two-dimensional case is shown in figure 3.2. The parameter $c_{\max}$ denotes the maximum speed of sound and the factor γ specifies the dependence on the FD order (see table 3.1). If this criterion is not fulfilled, amplitudes will grow to infinity and the simulation will become unstable.
The Nyquist–Shannon sampling theorem (Shannon, 1949) states, that we have to choose

$$\Delta h < \frac{1}{2}\lambda_{\min} = \frac{1}{2}\frac{c_{\min}}{f_{\max}} \approx \frac{1}{2}\frac{c_{\min}}{2\, f_c} \tag{3.43}$$

and

$$\Delta t < \frac{1}{2}T_{\min} = \frac{1}{2}\frac{1}{f_{\max}} \approx \frac{1}{2}\frac{1}{2\, f_c} \tag{3.44}$$

to prevent spatial and temporal aliasing, respectively. The minimum wavelength $\lambda_{\min}$

was replaced with the minimum velocity of propagation $c_{\min}$ and the maximum frequency $f_{\max}$, which is approximately twice the center frequency f_c of the source wavelet. $T_{\min}$ denotes the minimum period.

These criteria provide upper limits for Δh and Δt, but they are not sufficient because they do not prevent numerical dispersion.
I use the criterion proposed by Köhn (2015), namely

$$\Delta h \leq \frac{\lambda_{\min}}{n} = \frac{c_{\min}}{n\, f_{\max}} \approx \frac{c_{\min}}{2\, n\, f_c}, \tag{3.45}$$

to obtain a first estimate of Δh, which assures that the FD approximation of the spatial derivative of a sine function and the analytical solution differ by less than 0.1%. The influence of the FD order is taken into account by the factor n (exemplary values are presented in table 3.1). By inserting the obtained spatial sampling interval in the Courant-Friedrichs-Lewy criterion (equation 3.42), I obtain a first estimate and upper limit of Δt.
This workflow limits the spatial dispersion, which lowers the numerical velocity of propagation c_{FD} with increasing frequency f, but it does not consider temporal dispersion, which has the opposite effect. Due to the large number of propagated wavelengths (see table 2.1) in medical ultrasound, the forward modeled data strongly suffer from numerical dispersion. Especially Δt must be chosen much smaller than it is suggested by the Courant-Friedrichs-Lewy criterion to avoid strong temporal dispersion.

To assess the accuracy related to a given discretization, I simulate ultrasound waves with finite differences for several source-receiver distances s in an acoustic two-dimensional homogeneous model with the speed of sound c and compare them to the corresponding analytical solutions which are given by the convolution of the source wavelet $Q_s(t)$ and the Green's function for the two-dimensional wave equation $G_{2\mathrm{D}}(\boldsymbol{x}, \boldsymbol{x}_s, t)$, i.e.

$$P_{\mathrm{ana}}(\boldsymbol{x}, \boldsymbol{x}_s, t) = Q_s * G_{2\mathrm{D}} \tag{3.46}$$

where $\boldsymbol{x}$ and $\boldsymbol{x}_s$ are the coordinates of the receiver and source, respectively. The Green's function is defined as (Rienstra and Hirschberg, 2004)

$$G_{2\mathrm{D}} = \frac{1}{2\,\pi\, c^2} \frac{H(t - s/c)}{\sqrt{t^2 - s^2/c^2}} \tag{3.47}$$

with the Heaviside step function

$$H(\xi) = \begin{cases} 1 & \text{for } \xi \geq 0 \\ 0 & \text{for } \xi < 0 \end{cases} \tag{3.48}$$

and source-receiver distance $s = |\boldsymbol{x} - \boldsymbol{x}_s|$.

This approach is very suitable to check the accuracy of numerically simulated waveforms for a given discretization. However, numerous forward modelings would be necessary to find a reasonable combination of Δh, Δt and the spatial FD order because the influence of these parameters on $c_{FD}(f)$ is very complex. Due to compensating effects between the individual parameters and the aim of finding sampling intervals as large as possible to minimize the computational costs, it is inefficient to simply test smaller and smaller parameters until the desired accuracy is obtained.

To find a better way of determining an appropriate choice of those parameters and to analyze their influences, I derive a formula in appendix A which describes the ratio between the numerical and true velocity of propagation $\frac{c_{\mathrm{FD}}}{c}$ as a function of f, Δt, Δh, the spatial FD order and the incidence angle θ (see figure 3.2 for definition) for a plane wave propagating in a two-dimensional homogeneous acoustic medium considering second-order accurate temporal FD operators:

$$\frac{c_{\mathrm{FD}}}{c} = \frac{1}{2\,\pi\,f\,\Delta t}\arccos\left\{1 + c^2\frac{\Delta t^2}{\Delta h^2}\left[-a_0 + \sum_{m=1}^{M} a_m\left(\cos\left(\frac{m\,\cos(\theta)\,2\,\pi\,f\,\Delta h}{c}\right) + \cos\left(\frac{m\,\sin(\theta)\,2\,\pi\,f\,\Delta h}{c}\right)\right)\right]\right\} \tag{3.49}$$

The coefficients a_m are related to the spatial order of accuracy (examples are shown in table 6.1 in the appendix). The derivation is based on the one-dimensional approach proposed by Bohlen and Pan (2018) and considers both spatial and temporal dispersion. Even though the second-order differential equation formulation of the acoustic wave equation (see equation 6.4) and discretization on a non-staggered grid are considered, the dispersive characteristics, described by equation 3.49, are quantitatively equivalent to those described by Liu and Sen (2011) who consider the velocity-stress formulation and discretization on a staggered-grid. At least for a homogeneous medium, thus, the presented approach seems to be reasonable despite the assumptions made in its derivation.
In figure 3.3 the ratio of the true speed of sound $c = 1500\,\mathrm{m\,s^{-1}}$ and the numerical velocity of propagation c_{FD} of a plane wave propagating in the direction specified by θ is shown as a function of the frequency f for exemplary temporal sampling intervals Δt (upper left), spatial sampling intervals Δh (upper right), incidence angles θ (lower left) and spatial FD orders (lower right). Both, temporal and spatial dispersion, increase with frequency and partially compensate each other, but the latter clearly dominates for high frequencies. However, the temporal dispersion dominates within the lower frequency range which is preferably used for full-waveform inversion. Increasing the incidence angle from 0° to 45° is equal to a reduction of the "effective" Δh (refers to s_{min} in figure 3.2) and thus, has similar effects than reducing Δh. By using higher spatial FD orders it is possible to effectively reduce spatial dispersion at the expense of increased temporal dispersion. I choose the sixth-order spatial FD operator to optimize this trade-off in my experiments.

To determine Δt and Δh in a certain experiment, we have to consider the maximum number of propagated wavelengths or source-receiver distance s_{max}. Therefore, I calculate the difference between the true and numerically simulated arrival time

$$\delta t = \frac{s_{\max}}{c} - \frac{s_{\max}}{c_{\mathrm{FD}}} \tag{3.50}$$

using c_{FD} as specified in equation 3.49. With that formula it is possible to test and evaluate many different discretizations with very low effort and computational costs. I propose

$$|\delta t(f)| \leq \alpha\, T(f) = \frac{\alpha}{f} \tag{3.51}$$

with the period time T and constant $\alpha = 0.1$ (based on preliminary empirical results) as a criterion for sufficient accuracy. The choice of α is consistent with the criterion to avoid cycle-skipping (Pratt, 1999), which states that the phase mismatch for a certain frequency must be less than π to avoid being trapped in local minimum while minimizing the misfit (for details the reader is referred to section 3.3). This condition corresponds to $\alpha < 0.5$.

Finally, I would like to briefly repeat the suggested workflow for finding a reasonable discretization. Firstly, I use the criteria 3.42 and 3.45 to obtain first estimates of the spatial and temporal sampling interval, respectively, and to assure numerical stability. The absence of spatial and temporal aliasing is guaranteed by the Nyquist–Shannon criteria 3.43 and 3.44. Using equation 3.50 I can easily test several combinations of Δh and Δt. I choose sampling intervals as large as possible for which the criterion 3.51 is satisfied within the used frequency range to minimize the total number of discrete points. As a proof that the determined discretization yields a reasonable accuracy, I compare the simulated waveforms with the corresponding analytical solutions. It should be mentioned that attenuation, especially the related dispersion (see equation 3.22), also influences the numerical dispersion. Nevertheless, the acoustic approximation is used in all tests due to its simplicity.

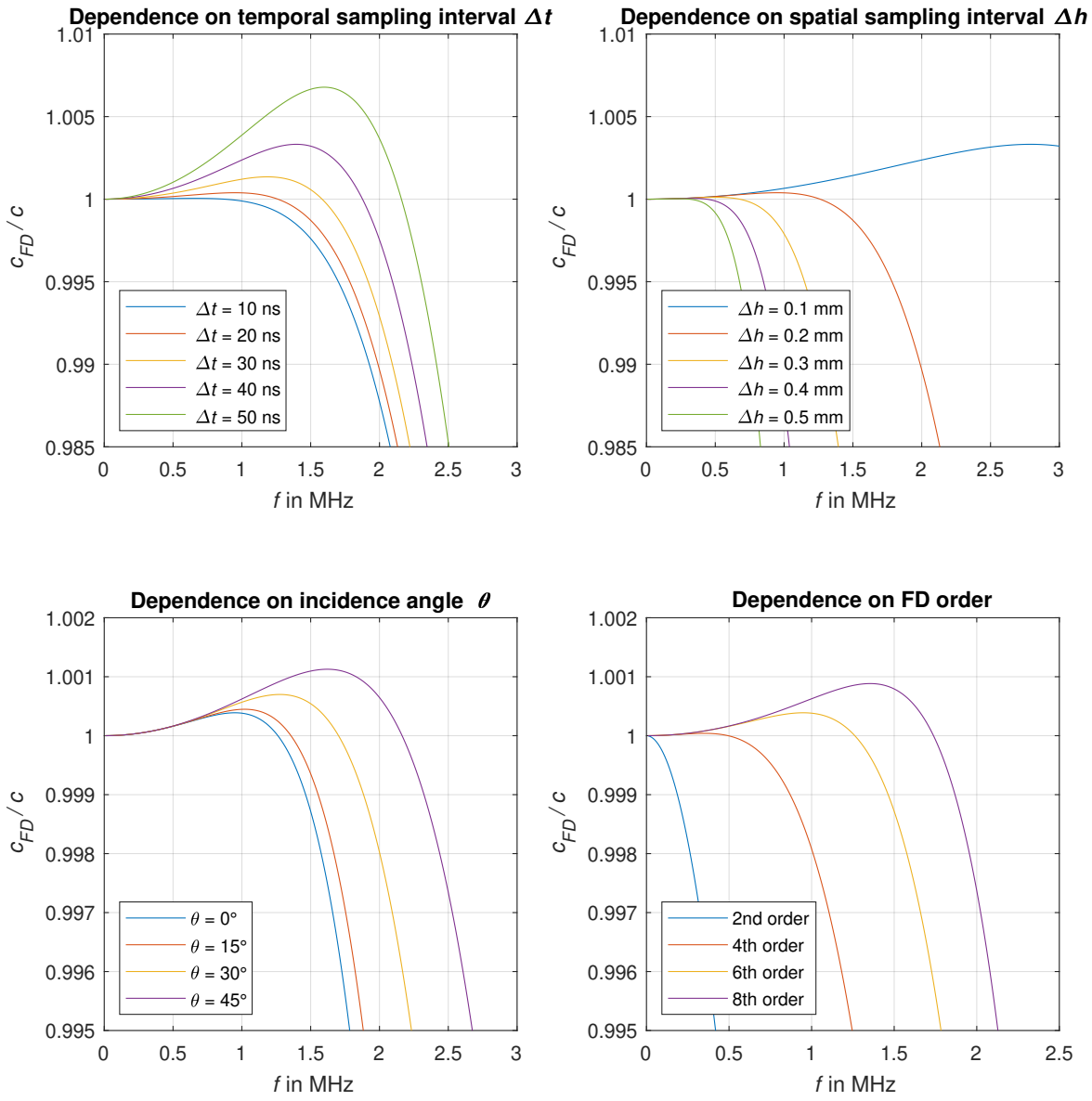

Figure 3.3: Analysis of numerical dispersion with respect to the temporal sampling interval Δt (upper left), spatial sampling interval Δh (upper right), incidence angle θ (lower left) and spatial FD order (lower right). In each plot the ratio o the true speed of sound $c = 1500\,\mathrm{m\,s^{-1}}$ and the numerical velocity of propagation c_{FD} of a plane wave propagating in the direction specified by θ is shown as a function of the frequency f. Unless specified otherwise, finite-differences operators second-order accurate in time and sixth-order accurate in space, $\Delta h = 0.2\,\mathrm{mm}$, $\Delta t = 20\,\mathrm{ns}$ and $\theta = 0°$ are used.

3.3 Time-domain full-waveform inversion

The goal of full-waveform inversion (FWI) is to find a model of the propagation medium which describes the observed waveforms as accurate as possible. By fitting the whole waveforms, i.e. exploiting information contained in the amplitudes and phases, FWI is able to exceed the resolution limit of classical tomography methods, which only exploit parts of the waveforms, e.g. the first-arrival times, at the expense of highly increased computational efforts. Furthermore, it is possible to reconstruct multiple parameters, e.g. the velocity of propagation, density and attenuation, all at once.
Since wave propagation is a highly non-linear problem the inverse problem is non-linear as well and cannot be solved directly. Instead, the problem is linearized and gradient-based minimization algorithms are used, in which an initial model is iteratively adjusted by minimizing the misfit between the synthetic and observed data using adjoint methods (Lailly, 1983; Tarantola, 1984).

The choice of a suitable misfit function is one of the most important steps for successful applications of FWI, especially for measured data. In this work, the well-established L_2-norm is used.
Moreover, an appropriate initial model is required to avoid non-convergence caused by cycle-skipping (Fichtner, 2010). To prevent cycle-skipping, i.e. being trapped in a local minimum of the misfit function due to the matching of wrong cycles in the synthetic and observed waveforms, the initial model must be accurate enough to generate synthetic data with less than half a period deviation (Pratt, 1999). Illustratively, this means, that the starting model must be located in the same valley as the global minimum of the misfit function.
A successful strategy to greatly reduce the aforementioned requirements is the multi-scale approach (Pica et al., 1990; Bunks et al., 1995). Based on the observation that the misfit functionals of smooth models tend to be smooth as well, the iterative inversion is started exclusively with the low-frequency or long-period components of a dataset to reduce the risk of non-convergence. Therefore, observed and modeled data are filtered with low-pass frequency filters in the time-domain FWI approach. The inversion is performed stage-wise, starting with several iterations of the lowest frequency components in the first stage and using the obtained final model as a starting model in the next stage, in which a low-pass filter with a higher corner frequency is used. This procedure is repeated until the whole frequency content is considered.
To increase the speed and robustness of convergence I use the preconditioned conjugate gradient method (Polak and Ribière, 1969; Shin et al., 2001) and perform a parabolic line search method proposed by Nocedal and Wright (2006), see also Sourbier et al. (2009).
For the sake of completeness, it should be mentioned that there exist other promising strategies to avoid cycle-skipping, which are not pursued in this work, e.g. the adaptive waveform inversion proposed by Warner and Guasch (2016) and the combination of wave-equation reflection traveltime inversion with dynamic warping and full-waveform inversion proposed by Ma and Hale (2013).

Figure 3.4 illustrates the general steps of the FWI workflow used in this work. Each step will be explained mathematically in the following sections using vector notation. For further information I refer to the very detailed overviews of the whole FWI framework given by Virieux and Operto (2009) and Fichtner (2010).

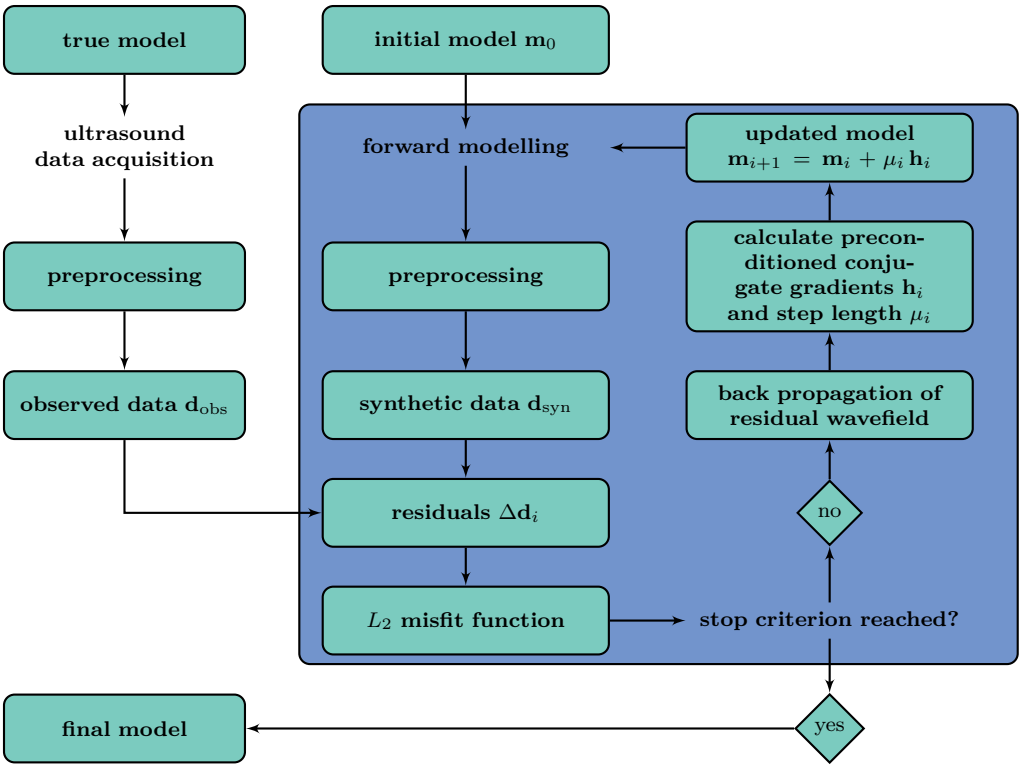

Figure 3.4: Scheme of the FWI workflow. The steps within the blue box are iterated until a stop criterion is reached.

3.3.1 Iterative solution of the full-waveform inversion problem

The objective of FWI in a deterministic sense is to find an optimal model of the propagation medium minimizing the misfit functional $E(\boldsymbol{m})$ which quantifies the discrepancies between the observed data $\boldsymbol{d}_{\mathrm{obs}}$ and the modeled synthetic data $\boldsymbol{d}_{\mathrm{syn}}$ (Fichtner, 2010).
To describe the relation between a model $\boldsymbol{m}$ and the related synthetic data I introduce the nonlinear forward operator $\mathfrak{F}$, such that

$$\boldsymbol{d}_{\mathrm{syn}} = \mathfrak{F}(\boldsymbol{m}) \tag{3.52}$$

holds. In the viscoacoustic case I parameterize the model using the vector

$$\boldsymbol{m} = (\boldsymbol{c}_{\mathrm{ref}}, \boldsymbol{\rho}, \boldsymbol{Q}_{\mathrm{ref}})^{\top} \ , \tag{3.53}$$

e.g. in terms of the spatial distribution of the reference speed of sound $\boldsymbol{c}_{\text{ref}}(\boldsymbol{x})$, density $\boldsymbol{\rho}(\boldsymbol{x})$ and reference quality factor $\boldsymbol{Q}_{\text{ref}}(\boldsymbol{x})$ defined at the reference frequency f_{ref}. In the acoustic case I use $\boldsymbol{m} = (\boldsymbol{c}, \boldsymbol{\rho})^{\top}$.
I define the misfit functional as the L_2-norm

$$E(\boldsymbol{m}) = \frac{1}{2}\,\Delta\boldsymbol{d}^{\top}\,\Delta\boldsymbol{d} \tag{3.54}$$

of the data residuals

$$\Delta\boldsymbol{d} = \boldsymbol{d}_{\text{syn}} - \boldsymbol{d}_{\text{obs}}\ , \tag{3.55}$$

which refers to a summation of the squared data residuals over all time steps and all source-receiver pairs. The resulting misfit is equal to the residual signal energy that is not described by the current model $\boldsymbol{m} = \boldsymbol{m}_i$.
The misfit is minimized by successively updating the current model $\boldsymbol{m}_i$ to a new model $\boldsymbol{m}_{i+1}$ with $E(\boldsymbol{m}_{i+1}) < E(\boldsymbol{m}_i)$:

$$\boldsymbol{m}_{i+1} = \boldsymbol{m}_i + \mu_i\,\boldsymbol{h}_i \tag{3.56}$$

The scalar μ_i denotes the step length and the vector $\boldsymbol{h_i}$ denotes the descent direction of the i-th iteration. For the first iteration $i = 0$ an initial model m_0 is needed (Fichtner, 2010).
This procedure is repeated until either a maximum number of iterations $i_{\max}$ is reached or the relative decrease of the misfit functional falls below a certain threshold $\delta E_{\text{rel,min}}$.
The estimation of the optimal step length using a parabolic line search method is described in section 3.3.3. In the following paragraphs, an overview of how to determine the descent direction $\boldsymbol{h}$ is given. In section 3.3.2 two more specific optimization strategies are introduced which modify $\boldsymbol{h}$ to make the inversion converge faster.
By assuming the Born approximation in which an updated model of dimension M

$$\boldsymbol{m} = \boldsymbol{m}_0 + \Delta\boldsymbol{m} \tag{3.57}$$

is given by the sum of an initial model $\boldsymbol{m}_0$ and a model perturbation $\Delta\boldsymbol{m}$, the second-order Taylor expansion of the misfit functional $E(\boldsymbol{m})$ in the vicinity of $\boldsymbol{m}_0$ can be expressed as

$$\begin{aligned} E(\boldsymbol{m}) &= E(\boldsymbol{m}_0 + \Delta\boldsymbol{m}) \\ &= E(\boldsymbol{m}_0) + \frac{\partial E(\boldsymbol{m}_0)}{\partial m_j}\Delta m_j + \frac{1}{2}\frac{\partial^2 E(\boldsymbol{m}_0)}{\partial m_j\,\partial m_k}\Delta m_j\,\Delta m_k + \mathcal{O}(\Delta\boldsymbol{m}^3) \end{aligned} \tag{3.58}$$

using the indices $j, k = \{1, ..., M\}$ and Einstein summation notation.
I require the derivative with respect to m_k in order to vanish to find a local minimum in the vicinity of $\boldsymbol{m}_0$:

$$\frac{\partial E(\boldsymbol{m})}{\partial m_k} = \frac{\partial E(\boldsymbol{m}_0)}{\partial m_k} + \frac{\partial^2 E(\boldsymbol{m}_0)}{\partial m_j\,\partial m_k}\Delta m_k \stackrel{!}{=} 0 \tag{3.59}$$

Rearrangement yields the model perturbation

$$\Delta\boldsymbol{m} = -\boldsymbol{H}^{-1}\,\nabla_m E(\boldsymbol{m}_0) \tag{3.60}$$

with the Hessian matrix

$$\boldsymbol{H} = \frac{\partial^2 E(\boldsymbol{m}_0)}{\partial m_j \, \partial m_k} \tag{3.61}$$

and the gradient of the misfit function with respect to the model parameters

$$\nabla_m E(\boldsymbol{m}) = \frac{\partial E(\boldsymbol{m})}{\partial m_j} \ , \tag{3.62}$$

which would give the minimum of E in one iteration for a linear relation $\mathfrak{F}$ between the data and the model. Due to the non-linearity of wave propagation, this needs to be iterated several times to converge toward the minimum (Virieux and Operto, 2009). In the update scheme shown here, referred to as Newton method, the inverse Hessian matrix used for gradient preconditioning addresses the problem that non-uniform illumination and geometrical spreading leads to decelerated convergence in some parts of the model. Due to the large memory requirements and computational costs related to the calculation and inversion of the large Hessian, several alternative preconditioning schemes have been proposed, referred to as quasi-Newton methods, which use approximations of the Hessian or scale the gradients based on the energy of the transmitted waves (Zhang et al., 2017). I use the latter type of preconditioning, as described in section 3.3.2. If no preconditioning is used, the misfit gradient is only scaled with a scalar step length, as shown in equation 3.56, and the optimization strategy is called steepest descent method.

The gradient of the misfit function with respect to the individual model parameters $\nabla_m E(\boldsymbol{m})$ is needed for all local optimization methods. It can be derived with the adjoint-state method, an efficient general method to calculate the gradient of a functional with respect to the model parameters. The functional has to depend on those model parameters through state variables, which are solutions of forward equations (Plessix, 2006). In FWI this holds for the misfit functional $E(\boldsymbol{d}_{\mathrm{syn}}(\boldsymbol{m}))$ that depends on the synthetic data $\boldsymbol{d}_{\mathrm{syn}}$, which themselves depend on the model parameters $\boldsymbol{m}$ as the solution of the forward problem, i.e. the wave modeling.
In order not to go beyond the scope of an overview, I directly introduce the viscoacoustic gradients obtained with the adjoint-state method as proposed by Kurzmann et al. (2015) or Yang et al. (2016):

$$\frac{\partial E}{\partial c_{\mathrm{ref}}} = -\frac{2}{c_{\mathrm{ref}}} \int \dot{P} \, \dot{P}^{\dagger} \, \mathrm{d}t \tag{3.63}$$

$$\frac{\partial E}{\partial \rho} = -\frac{1}{\rho} \int \dot{\boldsymbol{v}}^{\top} \, \boldsymbol{v}^{\dagger} \, \mathrm{d}t \tag{3.64}$$

$$\frac{\partial E}{\partial Q_{\mathrm{ref}}} = -\frac{1}{Q_{\mathrm{ref}}} \int \hat{R} \, P^{\dagger} \, \mathrm{d}t \qquad \text{with } \hat{R} = \frac{1}{L} \sum_{l=1}^{L} \frac{\dot{r}_l}{\omega_l} \tag{3.65}$$

The gradients are obtained by the convolution between one wavefield variable of the forward simulation, which takes the source wavelet of source s at position $\boldsymbol{x}_s$ as a disturbance, and one wavefield variable of the corresponding adjoint wavefield marked

with a dagger. Dots indicate derivatives taken with respect to time t. Using the L_2-norm as misfit function, the adjoint wavefield is obtained by injecting the time reversed residuals between the observed and synthetic data $\Delta\boldsymbol{d}(T_{\text{sim}}-t)$ at the receiver locations $\boldsymbol{x}_r$, the so-called adjoint sources, in one additional forward modeling per source. Thus, only two forward simulations per source are needed for the calculation of all gradients as proposed by Tarantola (1984). T_{sim} denotes the simulation time.
The same forward solver can be used for both the modeling of the "normal" and the adjoint wavefield. Only the source terms and the source locations have to be adjusted as described above (Plessix, 2006).
The gradient with respect to the reference quality factor Q_{ref} defined at the reference frequency f_{ref} is only needed in the viscoacoustic case. In the acoustic case speed of sound is non-dispersive, i.e. c_{ref} can be replaced by c.

3.3.2 Preconditioned conjugate gradient method

I introduce the conjugate gradient as proposed by Polak and Ribière (1969) to speed up the misfit convergence. Therefore, the steepest descent direction $-\nabla_m E(\boldsymbol{m}_i)$ in $\boldsymbol{h}_i$ is replaced with a linear combination of the misfit gradient at iteration i and the descent direction of the previous iteration $\boldsymbol{h}_{i-1}$ starting from the second iteration, yielding

$$\boldsymbol{h}_{\text{conj},i} = -\nabla_m E(\boldsymbol{m}_i) + \beta_i \, \boldsymbol{h}_{\text{conj},i-1} \ , \tag{3.66}$$

where

$$\beta_i = \frac{\nabla_m E(\boldsymbol{m}_i) \left(\nabla_m E(\boldsymbol{m}_i) - \nabla_m E(\boldsymbol{m}_{i-1})\right)}{\nabla_m E(\boldsymbol{m}_{i-1}) \, \nabla_m E(\boldsymbol{m}_{i-1})} \tag{3.67}$$

guarantees that $\boldsymbol{h}_{\text{conj},i}$ and $\boldsymbol{h}_{\text{conj},i-1}$ are conjugate (Fichtner, 2010).

Furthermore, I introduce preconditioning based on the waves' energy as implemented in IFOS2D.
The energy of waves is usually unevenly distributed within the propagation medium. In seismics, this is caused by geometrical spreading and the non-uniform illumination of the subsurface when sources and receivers are only located on the surface. In contrast to that, transducers are evenly distributed around the area of interest in medical ultrasound, but the sources are usually beam-forming, which results in higher energy levels in the middle and lower energy levels in the periphery, as shown in figure 2.5 in section 2.1.3. It is known that this phenomenon reduces the speed of convergence and the resolution of reconstructions in those "low-energy" regions (Zhang et al., 2011, 2017).
To counter this problem, the different gradients are scaled with the signal energy of the wavefield variables used for their calculation. Using the viscoacoustic parameterization shown in equation 3.53, we define the signal energy vector $\boldsymbol{W}$ as

$$\boldsymbol{W} = (\boldsymbol{W}_c, \boldsymbol{W}_\rho, \boldsymbol{W}_Q) \quad \text{with} \quad \begin{aligned} W_{c_n} &= \int_t P_n^2 \mathrm{d}t \\ W_{\rho_n} &= \int_t v_{x_n}^2 + v_{y_n}^2 \mathrm{d}t \\ W_{Q_n} &= \int_t \left(\tfrac{1}{L} \textstyle\sum_{l=1}^{L} r_{l_n}\right)^2 \mathrm{d}t \end{aligned} \tag{3.68}$$

and $n = 1, ..., N_{mathrmg}$, where $N_{mathrmg}$ is the total number of grid points. In practice, white noise specified by the small parameter ϵ_{prec} is added to avoid division by zero. Using this, the components of the preconditioned conjugate gradient of one source are given by

$$\eta_k = \frac{h_{\text{conj},k}}{W_k + \epsilon_{\text{prec}} W_{\max_k}} \tag{3.69}$$

with

$$W_{\max_k} = \begin{cases} \max(\boldsymbol{W}_c) & \text{for } k \leq N_{mathrmg} \\ \max(\boldsymbol{W}_\rho) & \text{for } N_{mathrmg} < k \leq 2N_{mathrmg} \\ \max(\boldsymbol{W}_Q) & \text{for } 2N_{mathrmg} < k \end{cases} \tag{3.70}$$

and $k = 1, ..., 3N_{mathrmg}$ in the viscoacoustic case. For the final descent direction $\boldsymbol{h}$ used for updating the models, as shown in equation 3.56, the gradients of all shots are summed up:

$$\boldsymbol{h} = \sum_{sources} \boldsymbol{\eta} \tag{3.71}$$

Additionally, it is possible to define a weighting matrix with values between 0 and 1 to manually manipulate the descent direction and thus enhance or suppress updates in certain areas of the model. Usually, this is done to prevent model updates in well-known areas, e.g. the water surrounding the breast in breast ultrasound, and in the vicinity of sources and receivers.

3.3.3 Parabolic line search method

In each update the descent direction $\boldsymbol{h}$ is scaled with a scalar step length μ, which controls the impact of the update on the model. During the first iterations, when the errors are large, large step lengths can be applied, while they have to be reduced in later iterations in order not to miss the minimum. For the estimation of optimal step lengths, I use a parabolic line search method proposed by Nocedal and Wright (2006).

The model is updated with two step lengths for a subset of N_{pls} sources, requiring $2N_{pls}$ forward simulations and the corresponding calculations of the misfit values. A parabolic fit of the misfit function based on these two values and the misfit of the actual iteration ($\mu = 0$) is performed. The optimal step length is obtained by determining the minimum of the obtained parabola.

3.3.4 Updates of density

Both, density and attenuation reconstructions, are mainly based on the amplitudes of observed waves. In contrast to that, the inversion of the speed of sound is based on the phase information. Due to dispersion, the phases are also minorly influenced by the attenuation.

Due to the reasons above, an appropriate density model is required to be able to obtain accurate reconstructions of the attenuation. Inverting the density is still greatly challenging, especially in viscoacoustic and viscoelastic FWI because there is a trade-off between the density and the quality factor specifying the attenuation.

According to Mast (2000), there exists a highly significant empirical linear relationship between speed of sound and density for a wide range of human soft tissues, including adipose, and fibroglandular tissues as well as body fluids. Considering that the acoustic properties of a tissue are well characterized by mixture laws, the relative proportions and acoustical properties of tissue constituents such as proteins, lipids, and water are supposed to be the cause of this nearly linear relationship. For example, speed of sound and density of lipids are lower than those of water, yielding a tissue with greater fat content having relatively lower speed of sound and density.

To solve the problem described in the beginning I propose to update the density $\boldsymbol{\rho}$ based on the current speed of sound model $\boldsymbol{c}$ at each iteration i using a linear relationship, i.e.

$$\boldsymbol{\rho}_i = A\,\mathbb{1} + B\,\boldsymbol{c}_i \ . \tag{3.72}$$

The symbol $\mathbb{1}$ specifies a vector of dimension $N_{mathrmg}$ filled with ones, where $N_{mathrmg}$ denotes the number of grid points. The coefficients A and B are obtained by a linear regression based on speed of sound and density estimations of different breast tissues (see figure 4.10 in section 4.4).

3.3.5 Source time function inversion

The application of FWI on measured data, e.g. field data in seismics or clinical data in medical ultrasound, requires the estimation of the N_{src} unknown true source time functions $\boldsymbol{S}_{\text{true}_s}$. If a wrong source term was used, the FWI algorithm would introduce artifacts in the reconstructed models to adapt the synthetic waveforms $\boldsymbol{d}_{syn_s}$ to the observed ones $\boldsymbol{d}_{obs_s}$. The data vectors specified with the index $s = \{1, ..., N_{\text{src}}\}$ denote subsets of the whole vectors, only containing the data of individual shot.

I use a source time function inversion approach in the frequency domain proposed by Pratt (1999). Therefore, the signals $f(t)$ have to be transformed from the time domain to the frequency domain $\tilde{f}(\omega)$ and vice versa with the Fourier transformation and the inverse Fourier transformation, respectively.
I try to find Wiener Filters $\boldsymbol{c}_s$ to filter the synthetic source signals $\boldsymbol{S}_{\text{syn}_s}$, used in the forward simulations to generate the synthetic data, in order to minimize the residuals between the spectra of the filtered synthetic and the true source terms:

$$\tilde{\boldsymbol{S}}_{\text{true}_s} - \boldsymbol{c}_s\,\tilde{\boldsymbol{S}}_{\text{syn}_s} \overset{!}{=} \min \tag{3.73}$$

With the source wavelet correction filters I could then approximate the true sources by the filtered synthetic ones. However, the true source terms are unknown and thus it is not possible to use condition 3.73 directly. By assuming that the true model is used for the forward simulations, the condition can be transformed into

$$\tilde{\boldsymbol{d}}_{obs_s} - \boldsymbol{c}_s \, \tilde{\boldsymbol{d}}_{syn_s} \stackrel{!}{=} \min \, . \tag{3.74}$$

The L_2-norm is used to define and minimize the residuals and a waterlevel ϵ_{stfi} is introduced to assure numerical stability by avoiding a division by zero. Then, the minimum is found when

$$\boldsymbol{c}_s = \frac{\tilde{\boldsymbol{d}}^{\top}_{obs_s} \, \tilde{\boldsymbol{d}}^{*}_{syn_s}}{\tilde{\boldsymbol{d}}^{\top}_{syn_s} \, \tilde{\boldsymbol{d}}^{*}_{syn_s} + \epsilon^2_{\text{stfi}}} \, . \tag{3.75}$$

One forward simulation per source is needed to invert the source time functions using this approach. Due to the assumption that the true model is known, this procedure is usually repeated several times during FWI to obtain better source estimations based on the more and more detailed model reconstructions. Using the multiscale approach, this has to be done at least once per frequency stage. One should be aware of the fact, that the inverted source time function would only be correct if the true model was considered.

3.4 Simulation of transducers

In contrast to seismics, the point approximation of sources and receivers is not sufficient in ultrasound because the size of ultrasound transducers is usually comparable to the wavelengths of generated ultrasound waves. This yields beamforming sources for which both the amplitude and phase of the generated waves strongly depend on the radiation angle. The same holds for the dependence of the observed waveforms at the receivers on the incidence angle.

This phenomenon can be described with the well-known formalism used in classical physics to describe the diffraction of waves (Szabo, 2014, chapter 6).
It is mainly based on two principles, namely the Huygens–Fresnel principle and the principle of superposition of waves. They state that every point on a wavefront becomes a source of a spherical wave itself and the sum of all secondary waves forms the subsequent wavefront. Depending on the size of the aperture or transducers, the radiation angle and the wavelength, which determine the phase shift between the individual secondary waves, they interfere constructively or destructively (Meschede, 2015).
There are various approaches to calculate the wavefield generated by an area source, e.g the Kirchhoff-Fresnel diffraction equation, the Fraunhofer approximation, valid in the far field, and the Fresnel approximation, valid in the near field. They can be calculated analytically for simple geometries of the transducer but have to be computed numerically for more complex situations (Meschede, 2015).

I follow another approach, which can be used to simulate the characteristics of both the sources and receivers. Based on the previously described Huygens–Fresnel principle and the principle of superposition of waves, the wavefield generated by an area source can be approximated by the superposition of the wavefields generated by many point sources located on that area with a distance less than half a wavelength. Analogously, the waveform recorded at an area receiver is given by the superposition of waves recorded at corresponding point receivers (Buddensiek et al., 2009; Assis et al., 2017). By doing so, any transducer geometry can easily be emulated.
I propose to calculate the individual wavefields of the point sources analytically if the propagation medium is homogeneous. For example, this is the case for the reference measurements of automated breast ultrasound systems. The three-dimensional analytical solution of source s is given by

$$P_{\mathrm{ana}}(\boldsymbol{x}, \boldsymbol{x}_s, t) = Q_s * G_{\mathrm{3D}} \ , \tag{3.76}$$

with the source term $Q_s(t)$ and the Green's function (Rienstra and Hirschberg, 2004)

$$G_{\mathrm{3D}} = \frac{\delta\left(t - s/c\right)}{4\pi\, c^2\, s} \ . \tag{3.77}$$

The solution only depends on the offset s and the speed of sound c. Thus, the source wavelet only has to be scaled with the factor $\left(4\pi\, c^2\, s\right)^{-1}$ and shifted in time by s/c. This is very easy to implement and the computational cost is low.

In section 5.3.5 I investigate how strong the generated and received waveforms are influenced by the finite size of the transducers at the KIT-IPE acquisition system and present some strategies to consider those effects in FWI.
For the sake of completeness, it should be mentioned that in some ultrasound systems source arrays are implemented in which single source elements are delayed and weighted in order to modify the beamforming characteristics (Szabo, 2014, chapter 7).

Chapter 4

Synthetic reconstruction tests

In this chapter I would like to examine the potential of full-waveform inversion for breast ultrasound under almost optimal but still realistic conditions by performing and evaluating various synthetic reconstruction tests. For designing those tests several steps are required.
First of all, a two-dimensional numerical breast model needs to be generated. As opposed to most former applications which use strongly simplified models, I consider an anatomically realistic model of a healthy breast provided by Lou et al. (2017) and add tumor phantoms in order to adapt it for the purposes of breast cancer detection. As a second step, a virtual acquisition system optimized for the application of full-waveform inversion is designed. To ensure realistic conditions, it is orientated towards two already existing automated breast ultrasound systems.
Based on those two steps, an appropriate spatial and temporal discretization is determined, a viscoacoustic forward simulation is computed to generate the "observed" data for the synthetic reconstruction tests and the resulting wavefields are analyzed.
Finally, various inversion tests are performed in order to investigate the achievable quality of the reconstructions of individual parameters, crosstalk between those parameters and different inversion strategies.

4.1 Model generation

In this section I present the numerical model used for the simulation of the "measured" data in the synthetic tests. The two-dimensional model is extracted from an anatomically realistic three-dimensional model based on magnetic resonance imaging data of a healthy breast. Due to the fact that the goal of this study is the analysis of the potential of medical ultrasound using FWI to detect and image breast cancer, two tumor phantoms are added. Each type of propagation medium in the model is parameterized with density ρ, speed of sound c_{ref} and quality factor Q_{ref} defined at the reference frequency f_{ref}.

Lou et al. (2017) published three anatomically realistic 3D breast models with different tissue compositions with respect to the overall density based on the BI-RADS classification (see section 2.2.1). I use the model of a healthy breast with scattered areas of fibroglandular tissue, which corresponds to the second of four categories of breast compositions with increasing mammographic density in the BI-RADS edition 2013. It distinguishes between skin, fat, fibroglandular tissue and blood vessels. The different tissues were segmented according to their intensities in contrast-enhanced magnetic resonance images with a resolution of 0.2 mm.

I modify the breast model by adding two tumor phantoms within the plane at $z = 43.2\,\text{mm}$ as shown in figure 4.1. The tumors are inserted at the interface of fibroglandular and adipose tissue based on the information given in section 2.2.1. A tumor phantom is created by inserting a predetermined ellipsoid at a desired location. Subsequently, random points within this ellipsoid are chosen. At each of these points, another ellipsoid with three random principal semi-axes, specified by a Gaussian distribution to limit the spatial extent, is inserted. Finally, possibly existent gaps within the union of all ellipsoids are assigned to the tumor.
This approach allows me to create irregularly shaped tumor phantoms as shown in the lower right image of figure 4.1 in order to emulate invasive cancer with a bulging surface which begins to infiltrate the surrounding tissue (as illustrated in figure 2.9 in section 2.2.1). This in turn makes it possible to assess the potential of medical ultrasound using FWI to image the irregular shape and margin of the resulting tumor phantoms which contain a high diagnostic value according to the BI-RADS classification.
By doing so, I added 3D tumor phantoms, although this could have been done directly with less efforts in the extracted 2D model, with the intension to create a model that could be used in further 3D reconstruction tests later on, e.g. to compare the results of 2D and 3D FWI.

In the next step, the different breast tissues and water surrounding the breast have to be parameterized in terms of density, speed of sound and attenuation. Keijzer et al. (2018) illustrate a large variance of different estimations of these parameters in a comparison of the results of previous related studies.

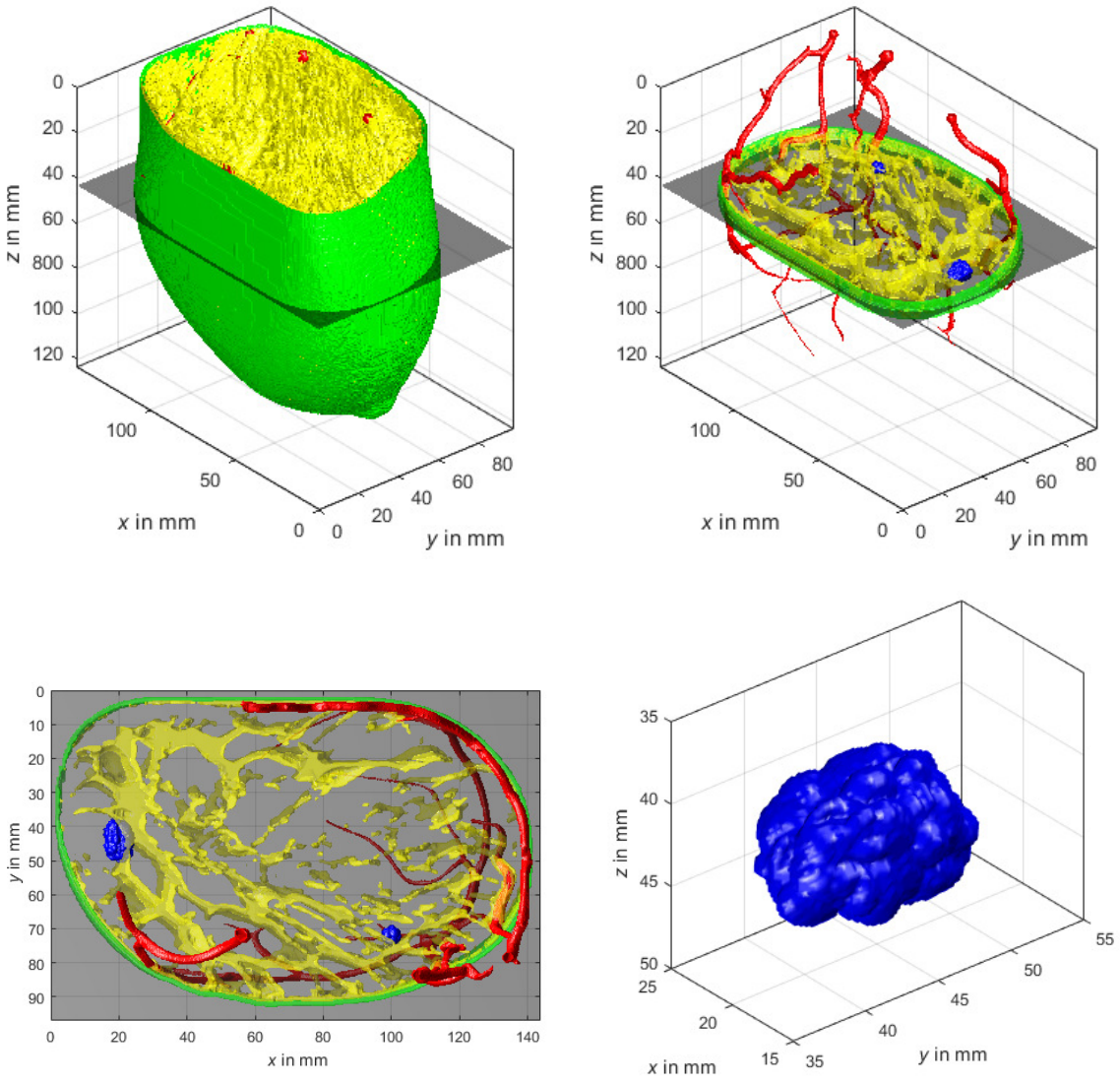

Figure 4.1: Modified version of a three-dimensional anatomically realistic numerical breast model provided by Lou et al. (2017). The gray plane at $z = 43.2\,\text{mm}$ specifies the level for which the two-dimensional model, used in the synthetic reconstruction tests, is extracted. Fibroglandular tissue is marked in yellow, skin is marked in green, tumors are marked in blue and blood vessels are marked in red. For the sake of improved visualization, fat, filling the remaining space, is not shown. In the upper left image, the whole model is shown. In the upper rigth image, only 4 mm of fibroglandular tissue and skin above and below the extracted plane are shown from the same perspective to enable a better view on the part of the model relevant for my tests. In the lower left image, the same structures are shown but from another perspective (vertically from above), in which the two-dimensional model is visualized (compare with figure 4.3). In the lower right image, the tumor phantom located at $x \approx 20\,\text{mm}$ and $y \approx 45\,\text{mm}$ is shown in detail.

Table 4.1: Information about the amplitude loss per distance per frequency $\hat{\alpha}$, the factor y specifying the frequency dependence and the corresponding references of various breast tissues and water.

Tissue	$\hat{\alpha}$ in $\mathrm{dB\,cm^{-1}\,MHz^{-y}}$	y	Reference
Water	0.002	2	Szabo (2014, appendix B)
Fibroglandular	0.91	1.5	Keijzer et al. (2018)
Fat	0.49	1.3	Keijzer et al. (2018)
Skin	0.42	1.7	Keijzer et al. (2018)
Blood vessels	0.06	1.6	Treeby et al. (2011)
Tumor	0.57	1.3	D'Astous and Foster (1986)

Furthermore, there is no individual study which proposes all parameters for all types of propagation media present in the used model and thus, unfortunately, the results from several studies, partially using different approaches to measure the parameters, have to be combined. To obtain a set of parameters as consistent as possible, I merge the results from studies which follow the same or at least a related approach and obtain similar estimations for common tissues. This finally leads to the parameters shown in table 4.2 on page 57.

The density and the speed of sound of skin, fat, fibroglandular tissue, blood vessels and water are directly obtained by Lou et al. (2017). The corresponding parameters for cancerous tissue refer to Weiwad et al. (2000).
The attenuation, specified by the amplitude loss per distance per frequency $\hat{\alpha}$, and the related references are shown in table 4.1. For blood vessels an estimation obtained for blood is used. Specifications in $\mathrm{Np\,cm^{-1}\,MHz^{-y}}$ were converted to $\mathrm{dB\,cm^{-1}\,MHz^{-y}}$ using equation 3.13. The corresponding frequency-dependent quality factors, presented in figure 4.2 are obtained by using equation 3.18. For viscoacoustic simulations using a generalized standard linear solid model as described in section 3.1.2 these curves have to be approximated within a limited frequency range using a least-squares optimization algorithm. In the optimal case it would be possible to individually emulate the frequency dependency of different tissues. However, within this framework it is only possible to approximate one single frequency dependence within the whole model. Furthermore, the accurate approximation of an exponential function requires many relaxation mechanisms. Each relaxation mechanism yields an additional partial differential equation which has to be solved in each timestep of the forward modeling and thus increases the computational cost. Hence, for the sake of simplicity, the quality factor of each tissue is approximated by $Q(f) = Q(f = f_{\mathrm{peak}}) = Q(f = 0.5\,\mathrm{MHz}) = \mathrm{const}$ within the entire used frequency range, which is a well-established strategy in seismics and prior applications of full-waveform inversion on ultrasound data. A constant function can be accurately approximated with only two relaxation mechanisms. By doing so within a frequency range of $0\,\mathrm{MHz} \leq f \leq 1\,\mathrm{MHz}$, I obtain the relaxation frequencies $f_1 = 113\,175\,\mathrm{Hz}$ and $f_2 = 963\,929\,\mathrm{Hz}$. The corresponding simulated frequency

dependence is exemplarily shown for fat in figure 4.2. In addition to the relaxation frequencies, the quality factor Q_{ref} defined at the reference frequency $f_{\text{ref}} = 0.5\,\text{MHz}$ must be specified at each gridpoint to completely describe attenuation. The quality factors of blood and water are clipped to 1000 because this value already corresponds to approximately no attenuation. Using this approximation and thus decreasing the range of Q_{ref} within the model makes the viscoacoustic inversion more stable.
In the previous paragraph, I anticipated that the peak frequency of the used source signal is $f_{\text{peak}} = 0.5\,\text{MHz}$ and most of the signal energy is transmitted within $0\,\text{MHz} \leq f \leq 1\,\text{MHz}$ (see figure 4.4 in section 4.2).

The final models of the density ρ, the reference speed of sound c_{ref} and the reference quality factor Q_{ref} are shown in figure 4.3 and the exact values are presented in table 4.2.

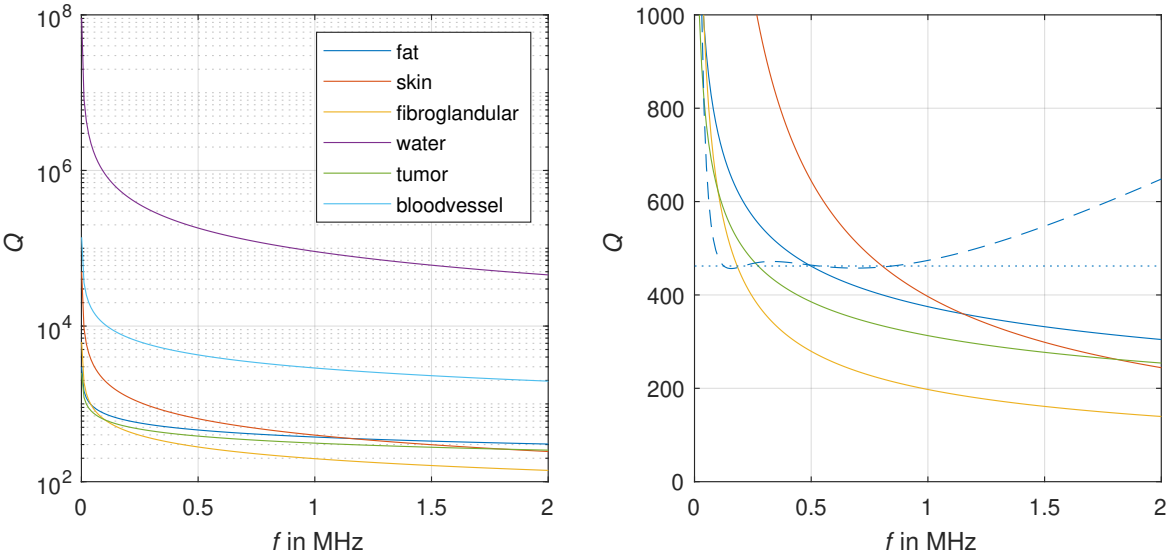

Figure 4.2: Frequency dependence of the quality factor Q of various propagation media. Due to the greatly varying magnitudes of Q, a logarithmic scale of the y-axis is used in the left image. In the right image the same functions are shown in a limited range of a linearly scaled Q-axis to show details for the quality factor of the relatively high attenuative breast tissues. Additionally, the used approximation (dashed line) of constant $Q(f = 0.5\,\text{MHz})$ (dotted line) within $0\,\text{MHz} \leq f \leq 1\,\text{MHz}$ is exemplarily shown for fat.

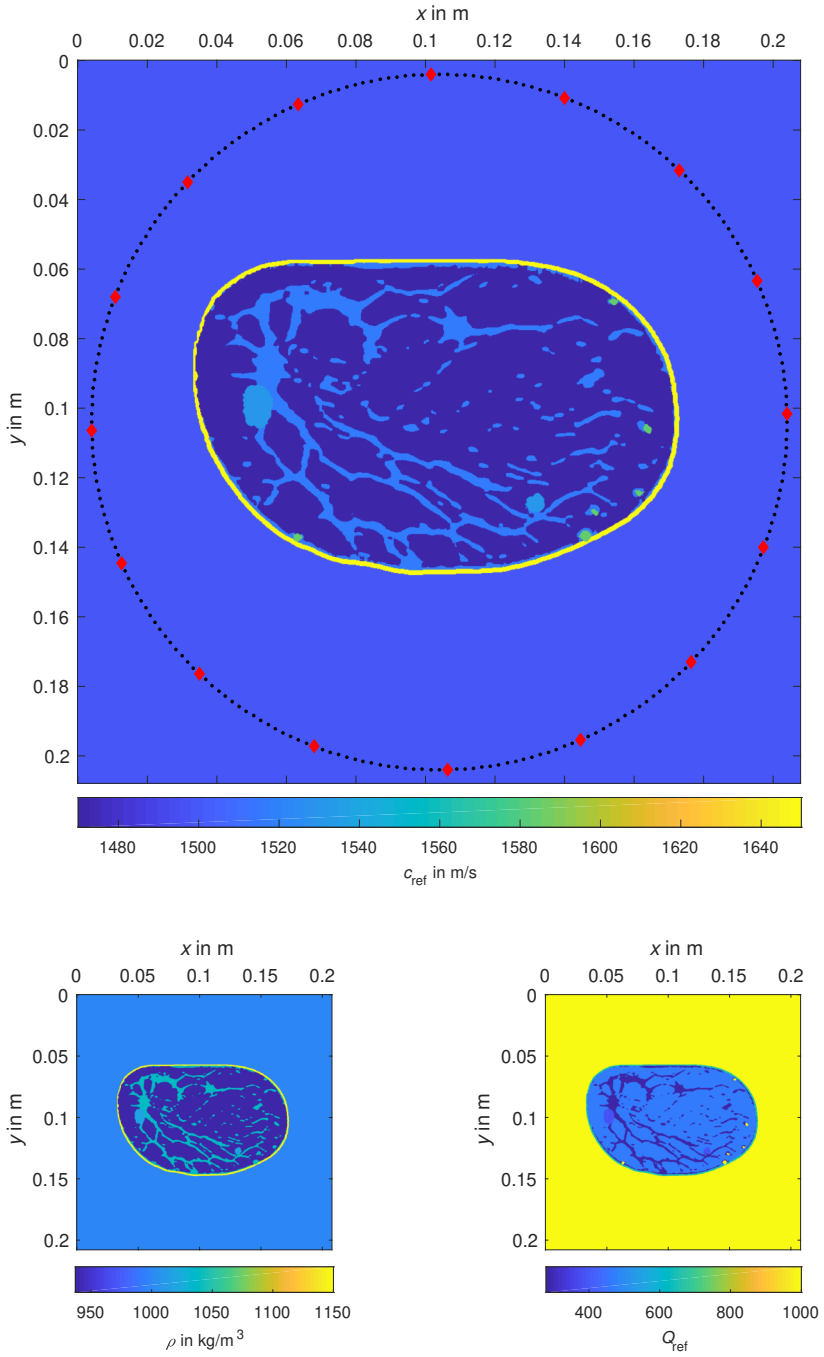

Figure 4.3: Synthetic models of density ρ, speed of sound c_{ref} and quality factor Q_{ref} defined at the reference frequency $f_{\text{ref}} = 0.5\,\text{MHz}$ and acquisition geometry. For the sake of completeness, the models of all parameters are shown. However, only one model is shown in a large view because the structures which correspond to different tissues (as specified in the lower left image of figure 4.1) are the same in each model and the exact parameters are presented in table 4.2. Furthermore, the uniform distribution of 16 sources (red diamonds) and 256 receivers (black dots) on a circular transducer array with a diameter of 20 cm are shown.

Table 4.2: Parameterization of various breast tissues and water in terms of density ρ, speed of sound c_{ref} and quality factor Q_{ref} defined at the reference frequency $f_{\text{ref}} = 0.5\,\text{MHz}$. The presented reference quality factors of blood and water are clipped values.

Tissue	c_{ref} in $\text{m}\,\text{s}^{-1}$	ρ in $\text{kg}\,\text{m}^{-3}$	Q_{ref}
Water	1500	1000	1000
Fibroglandular	1515	1040	279
Fat	1470	937	462
Skin	1650	1150	644
Blood vessels	1584	1040	1000
Tumor	1530	1020	385

4.2 Virtual data acquisition system

In this section I present the virtual data acquisition system which is used in the synthetic tests. It is designed to acquire data for ultrasound computed tomography using full-waveform inversion under optimal conditions. In order to implement it as realistically as possible, it is based on already existing acquisition systems.
The acquisition geometry is based on the CURE system (Duric et al., 2007) at the Karmanos Cancer Institute in Detroit, Michigan, USA, where 256 transducers are evenly distributed in a vertically movable solid-state ring with a diameter of 20 cm placed in a heated water tank. Each transducer can act as a source and a receiver. Based on the work of Vinard et al. (2014) introduced in section 2.2.3, only 16 of the 256 potential sources are used to reduce the number of forward simulations without significantly affecting the results. The sources are uniformly distributed on the transducer ring. According to Vinard et al. (2014), certain irregular distributions of sources could make it possible to use even fewer sources. This could be tested in further experiments in order to save even more computational costs.
The implemented distribution of sources and receivers is shown in figure 4.3.

One of the main disturbances is the movement of the breast during data acquisition. Thanks to a massively parallel data acquisition, the CURE system is able to perform the measurement of one shot in 300 µs (Duric et al., 2007). This time includes the observation of data and a waiting time to ensure that the amplitudes of waves generated by the prior shot decreased sufficiently. Considering 16 active sources the data acquisition per slice needs about 5 ms. This is much less than 0.5 s, the period of a cardiac cycle assuming a heart rate of 120 beats per minute for nervous patients. Thus, movements of the breast during data acquisition are supposed to be sufficiently small in order to not significantly disturb the results.

The complete measurement of a breast with 20 cm length is performed in about 20 s (Duric et al., 2007) which makes it possible to acquire the data during one single breath hold. Hence, also the second main cause of movements can be minimized.

Instead of using sources operating with a peak frequency of 1.5 MHz as implemented in the CURE system, I use sources with a peak frequency of 0.5 MHz which allows me to use much coarser discretization and thus dramatically reduces the computational cost. Furthermore, the inversion becomes much more stable. On the other hand, the achievable resolution decreases by using lower frequencies. However, the resolution is still sufficient as it will be shown in the reconstruction tests presented in section 4.4.1. Ultrasound transducers operating at such low frequencies already exist, e.g. the Panametrics V318 implemented in the Delft Breast Ultrasound Scanner (DBUS) (Heijnsdijk et al., 2018).

A shifted Ricker wavelet with a peak frequency $f_{\text{peak}} = 0.5\,\text{MHz}$, specified by

$$S(t) = \left(1 - 2\tau^2\right)\exp(-\tau^2) \quad \text{with} \quad \tau = \frac{\pi(t - 1.5/f_{\text{peak}})}{1.0/f_{\text{peak}}}\,, \tag{4.1}$$

is used as source signal $S(t)$ for all sources. The time-domain signal and its amplitude spectrum are shown in figure 4.4.

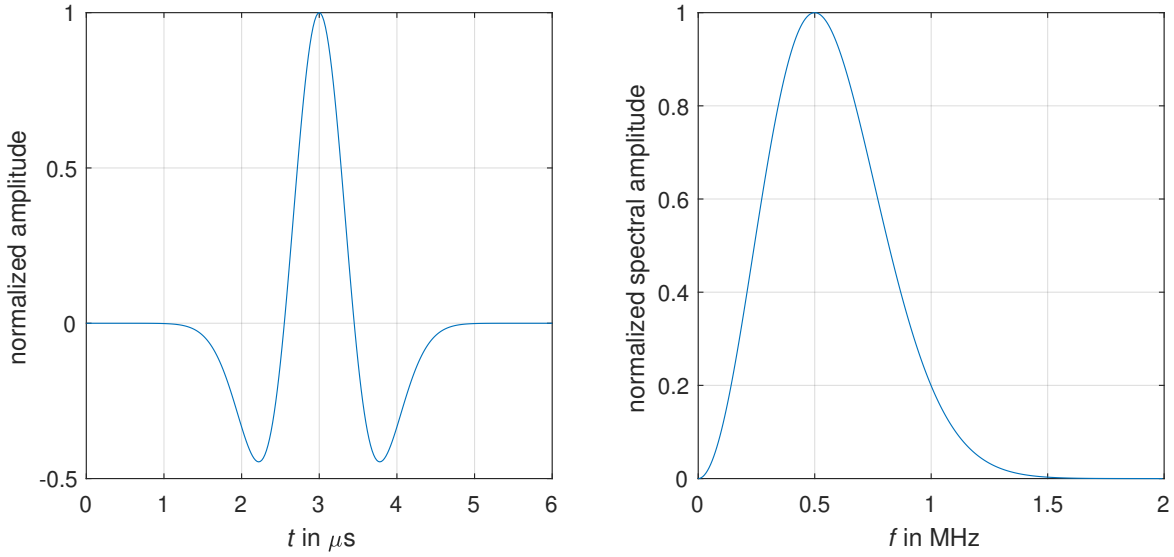

Figure 4.4: Source time function used in the synthetic tests. In the left image, a shifted Ricker wavelet with a peak frequency of 0.5 MHz and normalized amplitude is shown. In the right image, the corresponding amplitude spectrum is shown.

As opposed to real data acquisition system, all source signals are exactly the same and supposed to be known. Typically, in medical ultrasound a reference measurement in pure water is performed just before the breast is immersed in the water tank. Applying the source time function inversion, described in section 3.3.5, on the data acquired during this reference measurement makes it possible to obtain very accurate estimations of the source signals because the propagation medium is well known. Thus, this simplification is reasonable assuming that the source signals do not significantly change within two consecutive measurements. I refer to section 5.3.4 for an exemplary application of this strategy on a clinical dataset.
Sources and receivers are approximated as points. As described in section 3.4, this approximation is not valid for real ultrasound transducers because their size is comparable to the occurring wavelengths. Some strategies how the characteristics of finite-sized transducers could be taken into account in the forward modeling are presented in section 5.3.5.
Moreover, convolutional perfectly matched layers are implemented at all model boundaries to suppress artificial reflections. In real breast ultrasound systems propagating waves are reflected at the borders of the water tank but I assume those borders to be sufficiently far away to ensure no reflected wave energy reaches any receiver during recording time.

4.3 Forward simulation

In this section I discretize the model based on the specifications of the acquisition system given in the prior section and the methods presented in section 3.2.1. Subsequently, a viscoacoustic forward modeling is performed in order to obtain pseudo-observed data required for the reconstruction tests presented in section 4.4. For the sake of better understanding of wave propagation within a breast surrounded by water, the simulated wavefields are analyzed.

4.3.1 Discretization

In the following I determine the spatial and temporal sampling intervals Δh and Δt according to the strategy proposed in section 3.2.4.

I calculate sampling intervals based on the Nyquist–Shannon sampling theorem to prevent spatial and temporal aliasing, the criterion proposed by Köhn (2015) to obtain a first estimation of Δh and the Courant-Friedrichs-Lewy criterion to ensure numerical stability. Furthermore, finite-differences (FD) operators second-order accurate in time and second-, fourth-, sixth- and eighth-order accurate in space, minimum and maximum speed of sound $c_{\min} = 1470\,\mathrm{m\,s^{-1}}$ and $c_{\max} = 1650\,\mathrm{m\,s^{-1}}$ and the maximum frequency $f_{\max} = 1.5\,\mathrm{MHz}$ (see figure 4.4) are considered. The results are shown in table 4.3.
I use the criterion 3.51 based on the time shift generated by spatial and temporal dispersion to find sampling intervals as large as possible in order to minimize the product

of the number of grid points N_g and the number of time steps N_t and thus the computational cost. I use sixth order accurate spatial FD operators as a compromise based on the trade-off that higher orders allow to use larger Δh at the expense of smaller Δt. Considering a maximum propagation distance of 20 cm, I obtain $\Delta h = 0.2\,\mathrm{mm}$ and $\Delta t = 20\,\mathrm{ns}$ as shown in figure 4.5. Hence, it is possible to use a relatively large spatial sampling interval but the temporal sampling interval must be chosen much smaller than it is proposed by the Courant-Friedrichs-Lewy criterion to reduce temporal dispersion.
In this experiment I manually deal with the minimization problem but this procedure could also be automated using, for instance, a simplex algorithm or even a grid search due to the low computational cost of calculating equation 3.51. Therefore, the product of N_g and N_t would need to be minimized in terms of Δh, Δt and the spatial FD order under the constraint that criterion 3.51 is satisfied within a certain frequency range.

Lastly, in figure 4.6 the acoustic FD simulation in a homogeneous model of water (parameterized as stated in table 4.2) is compared with the analytical solution for different source-receiver distances for a final assessment of the achieved accuracy. The simulated waves tend to arrive a little bit earlier because the temporal dispersion slightly dominates in the used frequency range which yields an increased numerical velocity of propagation as shown in figure 4.5. However, the time shift is much smaller than the dominating period of the signal and the simulated waveforms are very similar to the analytical ones. Thus, the discretization is supposed to be reasonable.
In principle, an inappropriate discretization yielding strong numerical dispersion could be used within the framework of my synthetic reconstruction tests because the same forward solver is used for the generation of the pseudo-observed data and simulated data in FWI. This would not be possible in clinical applications because real measured data obviously do not suffer from numerical dispersion and, thus, artifacts in the model and in the estimated source time functions would be introduced to adapt the simulated waveforms to the measured data. In order to simulate conditions as realistic as possible in the synthetic tests, the discretization is determined as it would be necessary for the inversion of clinical data. Furthermore, accurate wave modeling is required to make it reasonable to analyze the wavefields in the anatomically realistic numerical breast model in section 4.3.2.

Considering $\Delta h = 0.2\,\mathrm{mm}$, a spatial model extension of 20 cm and 20 additional gridpoints on each side of the model for the implementation of the boundary layers, the grid consists of $N_\mathrm{g} = N_\mathrm{x}\,N_\mathrm{y} = 1040 \cdot 1040 = 1\,081\,600$ points. Based on the temporal sampling interval $\Delta t = 20\,\mathrm{ns}$ and the simulation time $T_\mathrm{sim} = 150\,\mu\mathrm{s}$, which ensures that the refracted wave is completely observed at receivers opposite to the active source, the FD time-stepping scheme needs to be solved $N_\mathrm{t} = 7500$ times.

Table 4.3: Comparison of the discretization proposed for the synthetic tests based on various criteria considering finite-difference operators second-order accurate in time and $2N$th-order accurate in space. The spatial and temporal sampling intervals Δh_{nyq} and Δt_{nyq} are calculated with the Nyquist–Shannon sampling theorems stated in equations 3.43 and 3.44. The spatial sampling interval $\Delta h_{\mathrm{köhn}}$ is calculated with the criterion proposed by Köhn (2015) stated in equation 3.45. The temporal sampling interval Δt_{cfl} is calculated with the Courant-Friedrichs-Lewy criterion stated in equation 3.42 considering $\Delta h_{\mathrm{köhn}}$. All calculations are based on the minimum and maximum speed of sound $c_{\mathrm{min}} = 1470\,\mathrm{m\,s^{-1}}$ and $c_{\mathrm{max}} = 1650\,\mathrm{m\,s^{-1}}$, respectively, as well as the maximum frequency $f_{\mathrm{max}} = 1.5\,\mathrm{MHz}$.

FD order $2N$	Δh_{nyq} in µm	Δt_{nyq} in ns	$\Delta h_{\mathrm{köhn}}$ in µm	Δt_{cfl} in ns
2	490	333	82	35
4	490	333	123	45
6	490	333	163	56
8	490	333	196	65

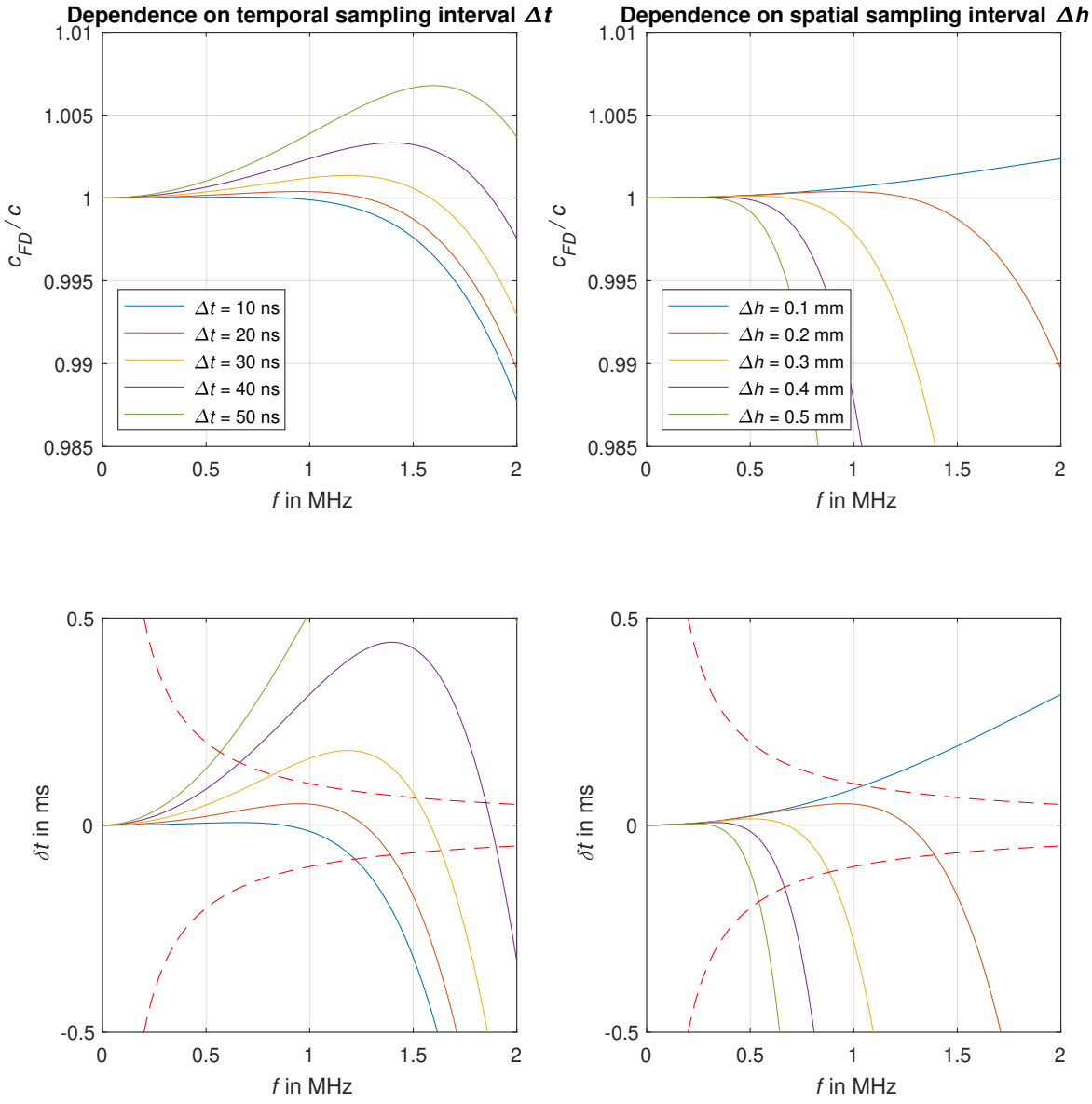

Figure 4.5: Analysis of numerical dispersion as a function of the discretization and frequency. On the left side, the spatial sampling interval is fixed at $\Delta h = 0.2\,\mathrm{mm}$ and several different temporal sampling intervals Δt are tested. Analogously, I investigate numerical dispersion for different spatial discretizations Δh with $\Delta t = 20\,\mathrm{ns}$. In the top row the ratio of the true speed of sound $c = 1500\,\mathrm{m\,s^{-1}}$ and the numerical velocity of propagation c_{FD} of a plane wave propagating in x-direction is shown. Finite-difference operators second-order accurate in time and sixth-order accurate in space are used. In the bottom row, the difference between the true and numerical traveltime δt for the propagation distance $s = 20\,\mathrm{cm}$ is shown. The red dashed lines are defined by $|\delta t| = 0.1\,T(f) = 0.1/f$, where $T(f)$ denotes the period of a monochromatic wave with frequency f.

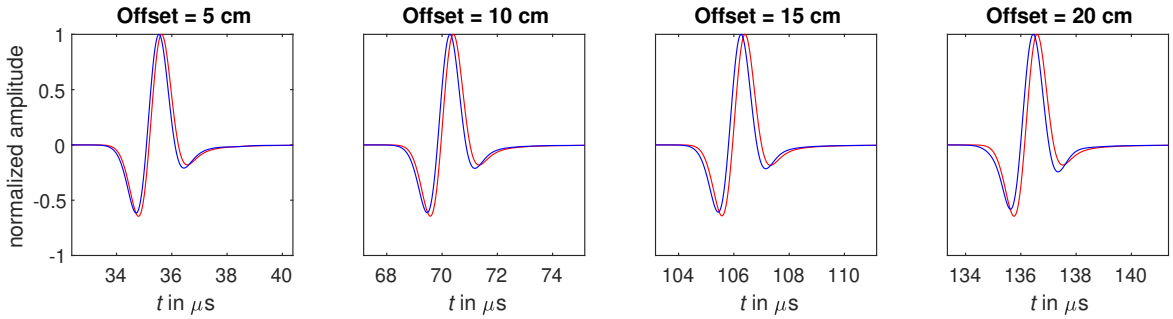

Figure 4.6: Comparison of finite-difference simulations (blue) and analytical solutions (red) at different source-receiver distances. Spatial and temporal sampling intervals $\Delta h = 0.2\,\mathrm{mm}$ and $\Delta t = 20\,\mathrm{ns}$, speed of sound $c = 1500\,\mathrm{m\,s^{-1}}$ and finite-difference operators second-order accurate in time and sixth-order accurate in space are considered. Note that the waveforms differ from the source signal shown in figure 4.4 due to the implicit line source assumption made in the two-dimensional approximation and the resulting interference of waves.

4.3.2 Wavefield analysis

To generate the pseudo-observed data in the framework of this synthetic reconstruction test, viscoacoustic wave modeling based on the specifications given in sections 4.1 and 4.2 is performed. The wavefields are analyzed to investigate the particularities of ultrasound wave propagation within a female breast.

Figure 4.7 shows snapshots of the propagating waves at four different points in time. The corresponding shot gather for both datasets (measurement with immersed breast and measurement in pure water) is presented in figure 4.8 in order to illustrate the effects of the breast on the wave propagation.
The direct wave exclusively propagating through water (1) contains no relevant information for the reconstruction of the breast. When it reaches the skin a small part of energy is reflected (3) due to the relatively high impedance contrast between water and skin and the remaining part of the energy is transmitted into the breast (2). By exiting the breast another relatively strong reflection is generated at the inside of the skin (3*).
While the transmitted aka refracted wave propagates through the breast, multiple scattering at small structures of fibroglandular tissue and blood vessels as well as multiple reflections and refractions at the interfaces between fat, large structures of fibroglandular tissue and tumor phantoms yield a complex wavefield, which is observed as the coda in the seismograms. At this point, it should be noted that the wavefield in a real three-dimensional propagation medium becomes even more complex due to out-of-plane scattering caused by obliquely oriented structures.
When waves hit the interface between the high-velocity skin and water or breast tissue under the critical angle, head waves (4), a special type of refracted waves, are generated which travel along the inner or outer boundary of the skin, respectively.

As shown in the shot gather, the refracted waves (2) have by far the highest amplitudes and thus dominate the misfit function. They contain much information about the speed of sound in their phases and about the density and anelastic attenuation in their amplitudes. To be precise, the phases also contain information about the attenuation due to anelastic dispersion. However, attenuation has a much greater impact on the amplitudes than on the phases. In comparison to direct waves propagating through water, the refracted waves arrive slightly delayed with decreased amplitudes due to scattering losses and anelastic attenuation. Due to the normalization the amplitude loss caused by geometrical spreading is not illustrated.
In figure 4.9, the normalized amplitude spectra of the true and reference data observed at the receiver at 225° distance to the active source are shown. I prefer to show the amplitude spectra of this exemplary receiver instead of the mean of all receivers because it would be strongly influenced by those receivers which exclusively observe the direct wave. It can be seen that mainly the high-frequency components are damped according to the exponential frequency dependence of anelastic attenuation in breast tissue. However, the damping in this experiment is relatively weak due to the low peak frequency of the sources.

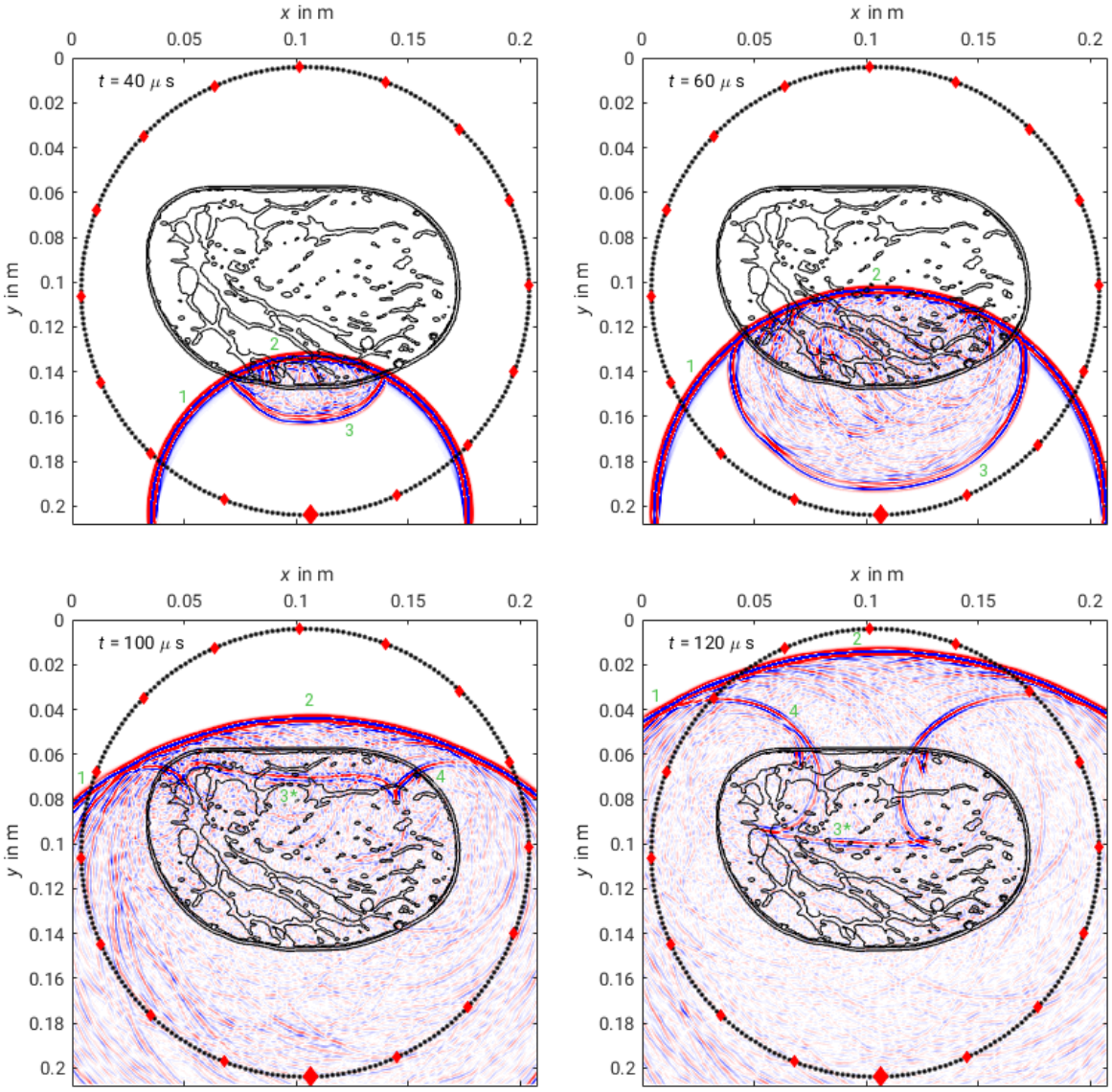

Figure 4.7: Snapshots of wave propagation in the numerical breast model at four points in time t. For the sake of better visualization of reflected and scattered phases, amplitudes, illustrated in red and blue, are clipped. Occurring wave types are marked as follows: direct wave (1), refracted wave (2), reflected wave generated at water-skin interface (3) and breast tissue-skin interface (3*) and head wave (4). Remaining phases are associated with multiple reflections and scattering. The interfaces between different tissues are shown as black lines. Sources are marked with red diamonds and receivers are marked with black dots. The active source is marked with a larger symbol.

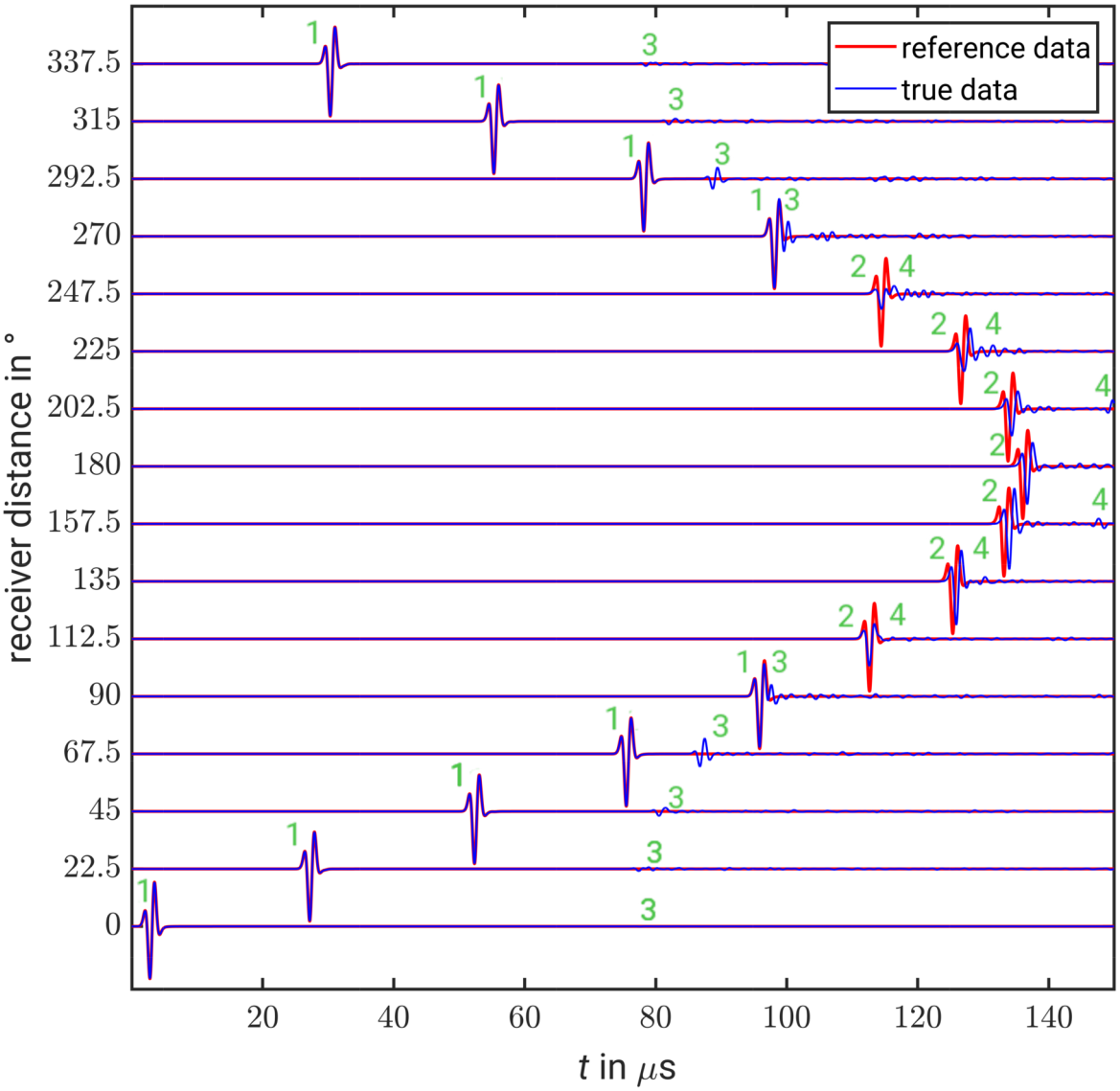

Figure 4.8: Shot gather of shot 1 (marked with a large symbol in figure 4.7). The angle specifying the receiver distance is counted anti-clockwise starting from the active source. In order to illustrate the effects of the breast on the wave propagation, both datasets, from the measurement with the immersed breast (true data) and in pure water (reference data), are shown. The amplitudes of both datasets are normalized with respect to the maximum of the reference data for each source-receiver distance. Wave types occurring in the true data are marked as follows: direct wave (1), refracted wave (2), reflected wave generated at water-skin interface (3) and head wave (4). Remaining phases are associated with multiple reflections and scattering.

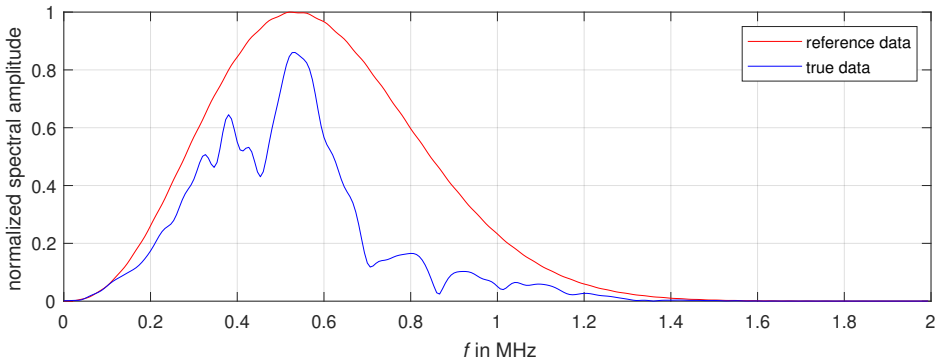

Figure 4.9: Amplitude spectrum of the receiver located at 225° distance to shot 1 (see figure 4.8). The spectral amplitudes of both datasets, from the measurement with the immersed breast (true data, blue) and in pure water (reference data, red), are normalized with respect to the maximum of the reference dataset.

4.4 Full-waveform inversion

In this section I present various synthetic reconstruction tests. In the following, I describe common aspects of their workflows and some general considerations. In section 4.4.1 four tests using different full-waveform inversion (FWI) strategies are described and their results are discussed. In section 4.4.2 two further tests are performed in order to investigate the crosstalk between speed of sound c, density ρ and quality factor Q.

According to section 3.3.4, in almost all tests the density is updated based on the current speed of sound model using an empirical relationship between both quantities. In order to determine the scalar parameters A and B which specify this relationship (see equation 3.72), a linear regression based on the parameters of different breast tissues presented in table 4.2 is calculated as shown in figure 4.10. I obtain $A = -506\,\mathrm{kg\,m^{-3}}$ and $B = 1\,\mathrm{kg\,m^{-4}\,s}$.

I use multistage workflows to specify the individual FWI strategies. In each stage it is determined which model parameters shall be inverted and the parameter ϵ_{prec}, which is related to the energy preconditioning as described in section 3.3.2, is set. A stage is performed until an individual stop criterion, defined as a minimum relative misfit decrease between two iterations, is reached. If ultrasound sources with higher frequencies were used it would be necessary to follow the multiscale approach, i.e. apply lowpass filters with increasing cutoff frequencies in later stages, or alternative strategies (see introduction of section 3.3) to prevent cycle skipping. However, due to the low peak frequency of the used sources and the resulting great robustness, this is not necessary. Thanks to this, fewer FWI iterations are needed and thus the computational cost is reduced.

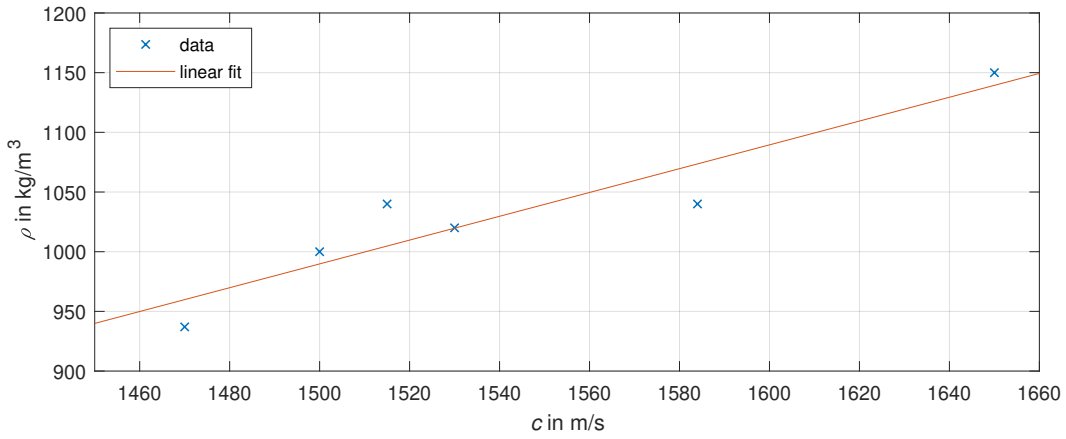

Figure 4.10: Estimation of a linear relationship between the speed of sound and the density of various breast tissues. A linear regression of the parameters shown in table 4.2 provides the coefficients $A = -506.4909\,\mathrm{kg\,m^{-3}}$ and $B = 0.9975\,\mathrm{kg\,m^{-4}\,s}$ of equation 3.72.

Even without following the multiscale approach the availability of low-frequency components and only small relative variations of the speed of sound between various breast tissues and water make it possible to use homogeneous initial models mimicking water in terms of its speed of sound and its density. In principle, it would also be possible to start with a corresponding homogeneous model of the quality factor but then many iterations would be needed to adapt the high values in water to those of breast tissues because allowing large step lengths μ makes the inversion unstable. Instead, a two-phased model is considered which distinguishes between water with $Q_{\text{ref}} = 1000$ and the breast with a mean value of $Q_{\text{ref}} = 400$.

For its generation I first need to introduce the gradient taper. As described in section 3.3.2 a two-dimensional taper is defined to prevent model updates in certain areas of the propagation medium. To be precise, I want to prevent updates of the model parameters outside the breast because the parameters specifying water (for a certain temperature) are well known. Moreover, this taper automatically prevents updates in the vicinity of sources and receivers, where usually artifacts are introduced during the inversion.

For both, the generation of the gradient taper and initial model of the quality factor, the outline of the breast has to be estimated. In the case of a synthetic reconstruction test the exact outline could directly be extracted from the known true models. However, I propose a method which is more suitable for realistic applications and can easily be automated. It only requires a rough model of speed of sound as could be provided, for instance, by first-arrival traveltime tomography which is usually performed prior to FWI to obtain an appropriate starting model anyway.

The single steps of the generation of the gradient taper are shown in the left image of figure 4.11. Exemplarily, a greatly smoothed version of the true speed of sound model is used as its resolution is comparable to that of a model obtained by first-arrival traveltime tomography. In step 1 all regions with $c_{\text{ref}} \geq 1510\,\text{m}\,\text{s}^{-1}$ are extracted in order to select the high-velocity skin bounding the breast. In step 2 a spherical buffer with a radius of 4 mm is applied on those regions to ensure that the whole breast is included despite the low resolution and potential inaccuracies of the reconstructed position of the skin. Furthermore, this step should close possibly existing gaps in the current selection as it is, for instance, the case on the left side of the shown example. In the third and final step the area enclosed by the selected region is added.

The gradient taper is then generated by setting the values inside this region to 1 and to 0 elsewhere. In order to generate the initial model of the quality factor I set Q_{ref} to 400 inside the selected region and to 1000 elsewhere. A transition zone between both regions, as shown in the right image in figure 4.11, is added to avoid the presence of a large contrast in the model because such "predetermined interfaces" are very difficult to be changed in FWI and thus increase the number of required iterations and the computational cost or even make the convergence of the misfit function unstable.

As described in section 4.2 the source time functions of all sources are supposed to be known and do not have to be estimated. For the parabolic step length estimation 8 of 16 sources are used and the inverted quality factor is restricted to a maximum value of 1000.
No noise was added to the pseudo-observed data. However, further synthetic tests which are not presented in this work indicate that a low level of white noise has only a very small impact on the results. In contrast to that, spatially correlated and non-white noise are supposed to be more complicated and their effects would need to be investigated in further studies.

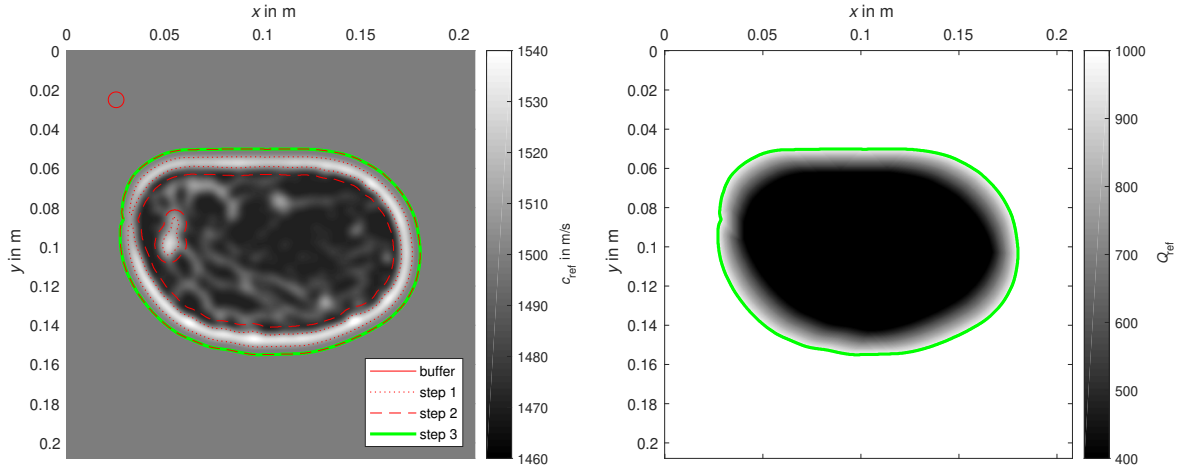

Figure 4.11: Generation of the gradient taper and the initial model of the reference quality factor Q_{ref} defined at the reference frequency $f_{\text{ref}} = 0.5\,\text{MHz}$. In the left image a smoothed version of the true reference speed of sound model c_{ref} and the results of the individual steps of selecting the extended outline of the breast, required for the generation of the gradient taper, are shown. In the right image the initial Q_{ref} model is shown.

4.4.1 Testing various inversion strategies

In this section I describe four synthetic reconstruction tests using different inversion strategies and discuss their results. Furthermore, I assess the quality of the reconstrcutions obtained under almost optimal but mostly realizable conditions to investigate the potential of FWI in breast ultrasound.

All tests are based on the same pseudo-observed data generated by viscoacoustic modeling in the synthetic models shown in figure 4.3 as described in section 4.3. The individual tests differ by their workflows which are specified in table 4.4. In the following, each test and its purpose are briefly described.
I try to make the tests as comparable as possible by changing only a single aspect of their workflow in each test. However, it must be noted that the results of those

tests depend on many parameters and options of the whole FWI workflow, e.g. the optimization strategy, optionally applied preprocessing on the data and the considered frequencies. Thus, the validity of the conclusions made at the end of this section is restricted to the set-up used in these tests and should not be generalized to applications with significantly differing specifications without further tests.

Viscoacoustic FWI
This test is used as a reference for the other ones. It is designed in accordance with three tested aspects of the workflow which are assumed to have a positive impact on the results. In each of the remaining tests one of those aspects is changed to examine the assumptions.
A viscoacoustic FWI is applied to reconstruct the reference speed of sound c_{ref} and quality factor Q_{ref} at the reference frequency $f_{\text{ref}} = 0.5\,\text{MHz}$. The density ρ is updated based on the current speed of sound model as described in section 3.3.4. An alternating inversion strategy is used in which c_{ref} and ρ are reconstructed separately from Q_{ref}. According to Li et al. (2014), I start with the inversion for c_{ref} because inaccurate phase velocity information is supposed to affect the attenuation reconstruction more drastically than how incomplete attenuation information affects the phase velocity reconstruction. Nevertheless, the accuracy of the reconstructed c_{ref} also depends on Q_{ref}. Hence, the procedure is repeated with smaller stop criteria as shown in table 4.4.
I use larger waterlevels of the gradient preconditioning ϵ_{prec} in early stages of the workflow in order to primarily reconstruct structures in well-illuminated regions first. In later stages smaller waterlevels are used which allow the reconstruction of details in poorly illuminated regions within already relatively accurately reconstructed models. This procedure has a positive impact on the stability of the misfit's convergence.

Density inversion
In section 3.3.4 I supposed that updating the density based on the current speed of sound model instead of inverting for the density improves the accuracy of the attenuation reconstruction and makes the viscoacoustic FWI more stable. I examine this hypothesis by performing a test that is equal to the "viscoacoustic FWI" test but in which the density is inverted based on its gradient as stated in equation 3.65.
Furthermore, it is interesting to investigate the potential of density inversion in this field of application due to the large diagnostic value of density. No other current tomography method or imaging technique in breast imaging is able to reconstruct the distribution of mass density directly, which would make FWI extremely valuable in this field if it provided reliable reconstructions of the density.

Simultaneous FWI
In this test I examine the recommendation of Li et al. (2014) to use an alternating inversion strategy. Therefore, I perform a test which is similar to the "viscoacoustic FWI" test but in which all parameters are simultaneously reconstructed. Due to the fact that the speed of sound and the quality factor have a different impact on the misfit function but one step length μ is applied on all gradients, it is reasonable to introduce

weighting factors for the gradients. Based on preliminary empirical tests, the gradient of the reference quality factor is given 175 times more weight than that of the speed of sound and density. It should be kept in mind, that these weigths have a huge impact on the convergence of the simultaneous FWI and thus the results are affected by them. Moreover, it should be noted that this is the only test in which the speed of sound is inverted until the relative misfit decrease between two iterations falls below 0.1% in order to perform the inversion of the quality factor until the same stop criterion as used in the other tests is reached.

Acoustic FWI

In the viscoacoustic forward modeling L additional equations per gridpoint have to be solved at each timestep compared to the acoustic case. The parameter L, specifying the number of considered relaxation mechanisms, is equal to two in the viscoacoustic modelings in this study. Hence, by using the acoustic approximation it is possible to significantly reduce the computational cost. These tests were computed in parallel on 400 cores of the ForHLR II cluster at the Karlsruhe Institute of Technology. Using the acoustic approximation instead of the viscoacoustic one, the computational time of one FWI iteration could be reduced from approximately 3 min to 2 min. However, obviously the quality factor, which has a high diagnostic value, cannot be reconstructed in this case.

In this test I investigate how well the viscoacoustic data can be explained without considering attenuation. It must be noted that the impact of the attenuation increases with higher frequencies. The same workflow as in the "viscoacoustic FWI" test is used but without the stages in which the quality factor is inverted.

Comparison of the results

In figure 4.12 the misfit curves and in figure 4.13 the achieved final data fits for all four tests are shown.

The "viscoacoutic FWI" is able to reduce the misfit the most to less than 1 % of its initial value. The "simultaneous FWI" converges faster during the first 33 iterations but then the convergence becomes slower. It needs the highest number of iterations until the stop criterion of the last stage is reached because the estimated optimal step lengths tend to be smaller whenever multiple parameters are inverted at once (strongly depends on the weighting factors) and it is the only test with such a small stop criterion pertaining to the inversion of speed of sound. The "density inversion" falls into a local minimum after only 37 iterations. The reconstructed models are able to explain the signals of the refracted waves but not the coda. As an exceptional case, the "acoustic FWI" starts with a larger misfit because it does not consider the initial model of the seismic quality factor. As might be expected, the final misfit is the largest of all tests because the amplitudes of refracted waves are overestimated and small errors in the phases are introduced due to the neglect of attenuation.

In figures 4.14, 4.15 and 4.16 the final reconstructed models of the reference speed of sound, the reference quality factor and the density are shown. They are used for a first visual assessment of the results.

Table 4.4: Stages of the full-waveform inversion workflows used in the synthetic reconstruction tests. In the third, fourth and fifth column it is stated which quantities are reconstructed in the respective stages. It must be noted that the density is only inverted in a strict sense in the "density inversion" test while it is updated by scaling the speed of sound, as described in section 3.3.4, in all other tests. The stop criterion is defined in terms of a minimum relative misfit decrease between two iterations. The coefficient ϵ_{prec} defines the waterlevel in the preconditioning as described in section 3.3.2.

Test	Stage	Rec. c	Rec. ρ	Rec. Q	Stop criterion	ϵ_{prec}
Density inversion	1	✓	✓	✗	5 %	10^{-7}
	2	✗	✗	✓	5 %	10^{-3}
	3	✗	✗	✓	1 %	10^{-5}
	4	✓	✓	✗	1 %	10^{-10}
	5	✗	✗	✓	0.1 %	10^{-7}
Simultaneous FWI	1	✓	✓	✓	5 %	10^{-3}
	2	✓	✓	✓	1 %	10^{-5}
	3	✓	✓	✓	0.1 %	10^{-7}
Acoustic FWI	1	✓	✓	✗	5 %	10^{-7}
	2	✓	✓	✗	1 %	10^{-10}
Viscoacoustic FWI	1	✓	✓	✗	5 %	10^{-7}
	2	✗	✗	✓	5 %	10^{-3}
	3	✗	✗	✓	1 %	10^{-5}
	4	✓	✓	✗	1 %	10^{-10}
	5	✗	✗	✓	0.1 %	10^{-7}

The reconstructions of the speed of sound in the "acoustic FWI", "viscoacoustic FWI" and "simultaneous FWI" are very detailed. The result of the "density inversion" test is significantly less sharp and there exist relatively strong artifacts in the water close to the breast where the gradient does not prevent model updates. Additionally, a speed of sound reconstruction obtained by traveltime tomography considering bent rays, as described by Dapp (2013), is shown. It is kindly provided by the Institute of Data Processing and Electronics at the Karlsruhe Institute of Technology and is based on the same viscoacoustic data which are used in the reconstruction tests. Obviously, the results obtained by FWI are superior to those obtained by traveltime tomography. Even fine details, e.g. small fibroglandular structures and the margin of the tumor phantoms, can be reconstructed accurately. However, it must be noted, that the resolution of the traveltime tomogram would increase if higher frequencies were used.
The inversion of the quality factor is clearly less stable than the inversion of the speed of sound. The "density inversion" failed as it fell into a local minimum very early on.

The "viscoacoustic FWI" introduced small artifacts, especially at the interfaces between different propagation media. The result obtained by the "simultaneous FWI" is smoother but the quality factor of fat is significantly underestimated. Both approaches tend to underestimate the quality factor or overestimate the attenuation in the vicinity of the skin, and they are not able to reconstruct the small-scale, high-contrast blood vessels. However, both reconstructions are suprisingly accurate regarding the fact that inverting the attenuation is still a great challenge in FWI, especially in consideration of the large number of propagated wavelengths and the resulting complexity of the wavefield.
The "density inversion" is not able to provide suitable reconstructions of the density. The estimations obtained by scaling the speed of sound model are clearly superior. However, these reconstructions are intended to stabilize the inversion and should not be interpreted as they were not independently obtained.

In tables 4.5 and 4.6, the mean values and standard deviations of the reference speed of sound and the reference quality factor, respectively, are calulcated seperately within the spatial boundaries of each tissue, as they are defined in the true model, for a quantitative assessment of the achieved accuracy. Due to the reasons mentioned above, the density is not assessed in this manner.
Regarding the speed of sound, the mean values can be reconstructed very precisely in the "simultaneous FWI", "viscoacoustic FWI" and "acoustic FWI". For larger structures such as fat, fibroglandular tissue and tumors the mean values differ by only a few meters per second, which demonstrates that the results are not only qualitatively but also quantitatively interpretable. Based on the calculated standard deviations, it is unambiguously possible to distinguish all tissues based on their reconstructed values, except fibroglandular and cancerous tissue. However, considering the visual impressions in the reconstructed model and additional knowledge of the interpreter about the typical appearance and location of cancer, the detection of suspicious masses based on such results seems to be promising. Surprisingly, using the acoustic approximation has no negative effects on the reconstructed speed of sound model, at least if such low frequencies are used. If higher frequencies were used, the anelastic attenuation and the related velocity dispersion would have a larger impact on the phases and, thus, on the speed of sound reconstruction.
The assessment of the quality factor shows that the "viscoacoustic FWI" is able to almost perfectly reconstruct the mean values within fat, fibroglandular and cancerous tissue with relatively high standard deviations while the "simultaneous FWI" reconstructs a smoother model with smaller standard deviations but less precise mean values.

Conclusion
Based on the presented results, I validate the assumptions made in section 3.3.4 which state that estimating the density based on the accurate reconstructions of the speed of sound, instead of inverting it, increases the robustness of the inversion, especially with respect to the inversion of attenuation. For the sake of completeness, a further test in which the density and attenuation are simultaneously inverted, was performed. It is

not presented in this work because the results are very similar to those of the "density inversion" test. Hence, it confirms the recommendation pertaining to the updates of the density model.
According to figure 4.14 and table 4.5 it is definitely reasonable to apply an acoustic FWI on low-frequency ultrasound data to exclusively reconstruct the spatial speed of sound distribution with significantly reduced computational cost. Nevertheless, viscoacoustic FWI is able to provide high-quality reconstructions of the attenuation which can be used for a joint tissue characterization.
Based on the speed of convergence, its simplicity and robustness, I agree with the recommendation of Li et al. (2014) to use an alternating inversion strategy starting with the inversion of speed of sound. Nevertheless, I assume that the "simultaneous FWI" could be improved further in order to increase its capacity to compete with the alternating approach, for instance by using a more complex step length estimation method providing individual step lengths for different gradients instead of using one step length for all gradients in combination with fixed gradient weights.
All in all, the results demonstrate the achievable high accuracy of speed of sound and quality factor reconstructions using FWI in breast ultrasound. Using low-frequency sources leads to sufficiently high resolution while making the inversion very robust as it is clearly demonstrated by obtaining accurate results despite considering very simple initial models and ignoring the multiscale approach.

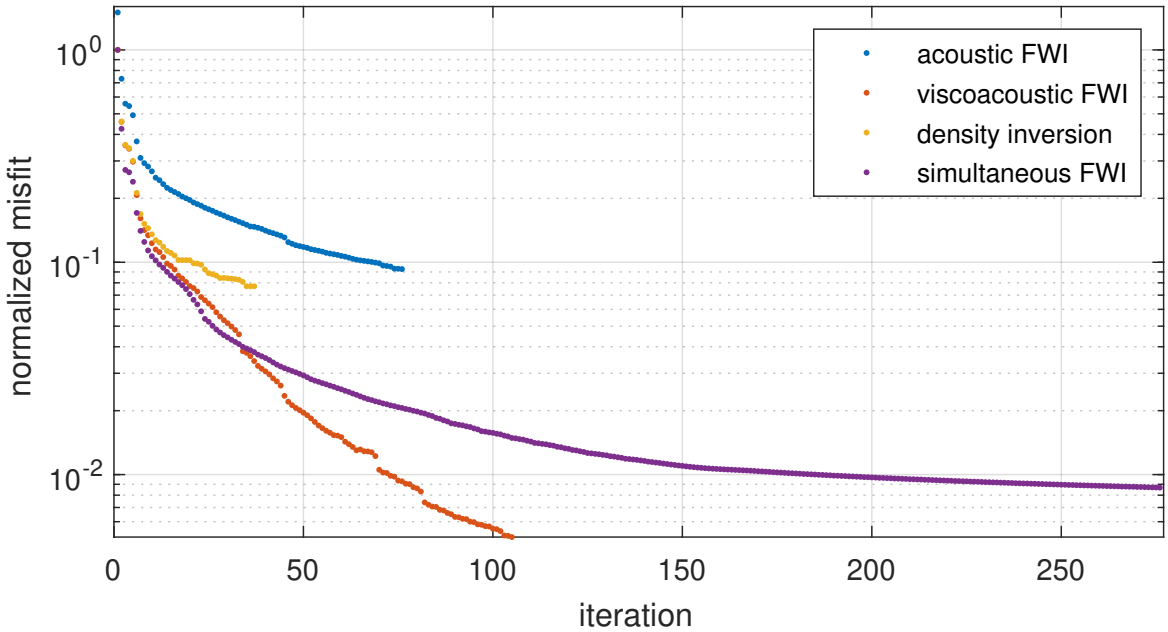

Figure 4.12: Misfit curves of the synthetic tests. The misfit is normalized to the initial misfit in the viscoacoustic test. The initial misfit in the acoustic case is larger because, in contrast to the other tests, no attenuation is considered. Leaps in the misfit curves correspond to the first iterations of new stages in the workflow.

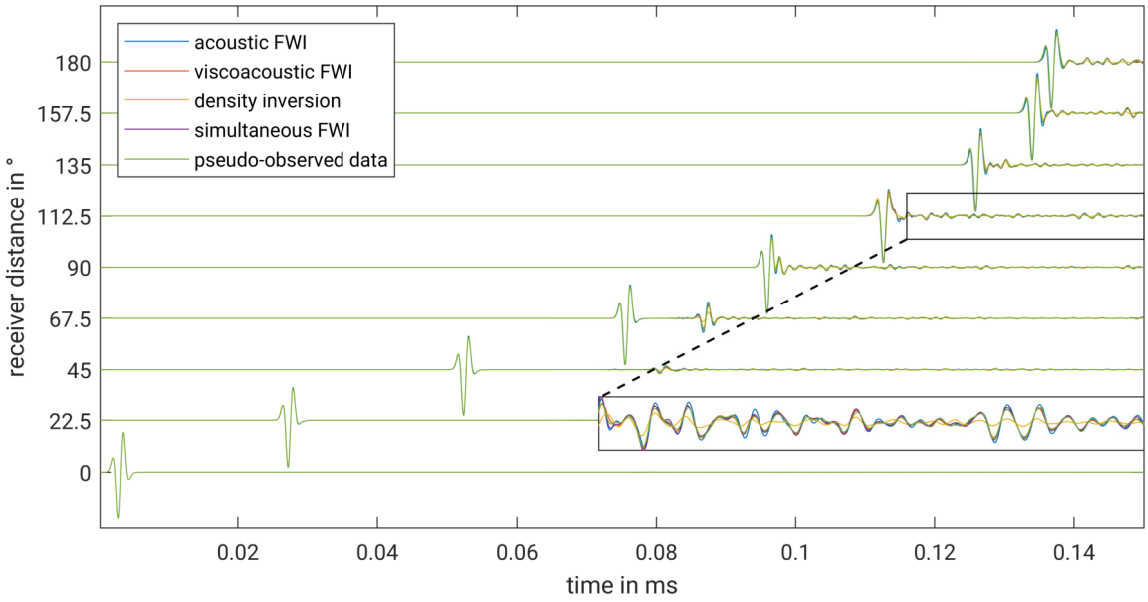

Figure 4.13: Data fit for selected receivers of source 1 (large symbol in figure 4.7) in the synthetic tests. Each trace is normalized to its maximum. In order to visualize the achieved accuracy, a magnified view of the coda of an exemplary trace is shown.

Table 4.5: Assessment of the achieved accuracy of the speed of sound reconstructions. If viscoacoustic wave modeling is considered the stated values refer to the reference speed of sound defined at the reference frequency $f_{\text{ref}} = 0.5\,\text{MHz}$.

		Density inversion		**Simultaneous FWI**		**Acoustic FWI**		**Viscoacoustic FWI**	
Propagation medium	c_{true} in $\text{m}\,\text{s}^{-1}$	$\bar{c}_{\text{den}}$ in $\text{m}\,\text{s}^{-1}$	$\sigma_{c_{\text{den}}}$ in $\text{m}\,\text{s}^{-1}$	$\bar{c}_{\text{sim}}$ in $\text{m}\,\text{s}^{-1}$	$\sigma_{c_{\text{sim}}}$ in $\text{m}\,\text{s}^{-1}$	$\bar{c}_{\text{ac}}$ in $\text{m}\,\text{s}^{-1}$	$\sigma_{c_{\text{ac}}}$ in $\text{m}\,\text{s}^{-1}$	$\bar{c}_{\text{vac}}$ in $\text{m}\,\text{s}^{-1}$	$\sigma_{c_{\text{vac}}}$ in $\text{m}\,\text{s}^{-1}$
Fat	1470	1477	6	1467	9	1470	6	1470	5
Fibroglandular	1515	1499	8	1529	17	1517	13	1518	11
Tumor	1530	1520	8	1533	8	1529	7	1528	6
Blood vessels	1584	1525	7	1586	22	1580	18	1566	16
Skin	1650	1538	13	1662	38	1637	37	1623	26

Table 4.6: Assessment of the achieved accuracy of the quality factor reconstructions. If viscoacoustic wave modeling is considered the stated values refer to the reference quality factor defined at the reference frequency $f_{\text{ref}} = 0.5\,\text{MHz}$.

		Density inversion		**Simultaneous FWI**		**Viscoacoustic FWI**	
Propagation medium	Q_{true}	$\bar{Q}_{\text{den}}$	$\sigma_{Q_{\text{den}}}$	$\bar{Q}_{\text{sim}}$	$\sigma_{Q_{\text{sim}}}$	$\bar{Q}_{\text{vac}}$	$\sigma_{Q_{\text{vac}}}$
Fat	462	995	68	376	51	459	171
Fibroglandular	279	604	427	307	50	263	125
Tumor	385	824	332	288	20	381	109
Blood vessels	1000	94	220	285	68	178	83
Skin	644	194	363	385	197	394	381

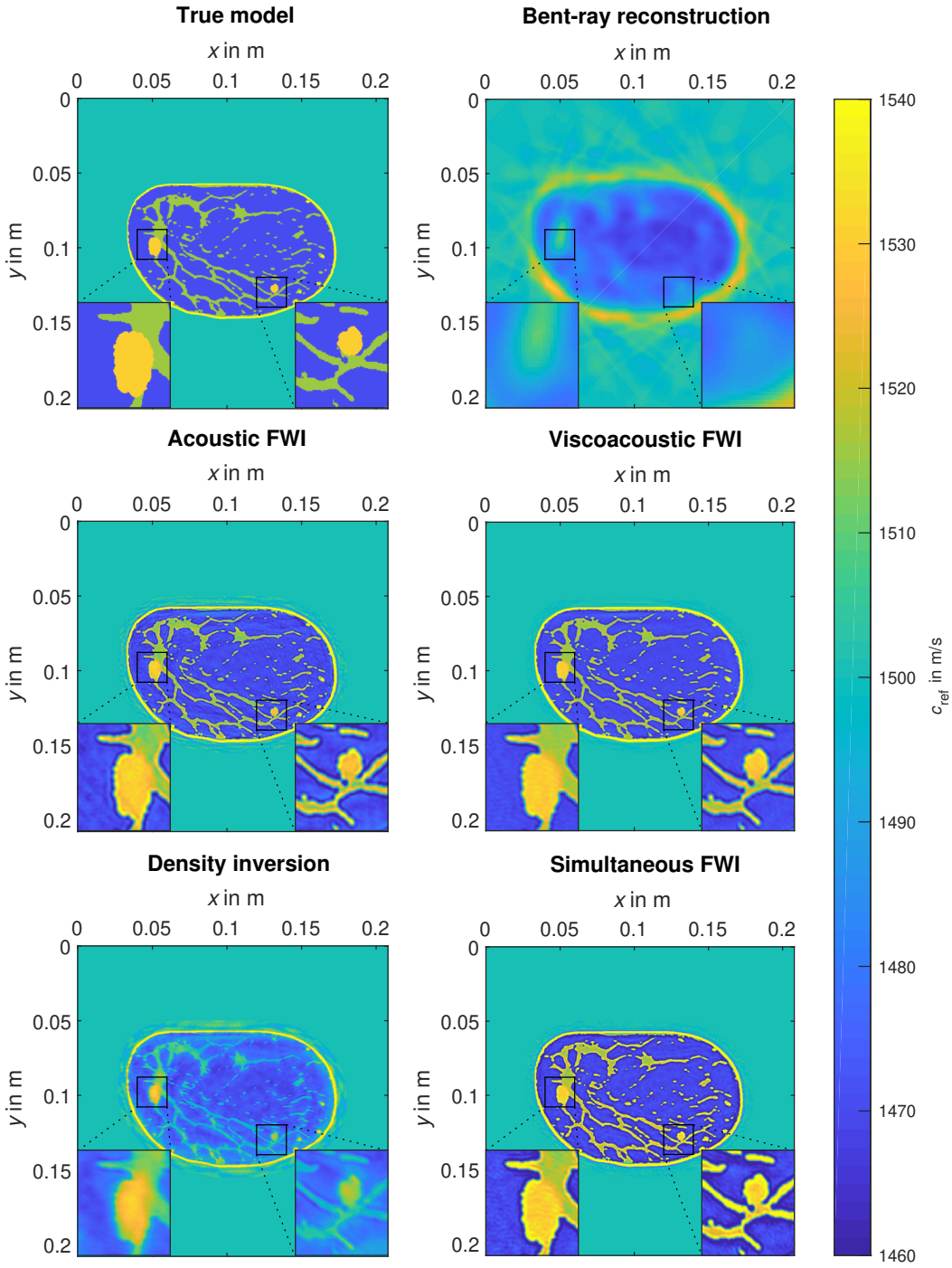

Figure 4.14: Reconstructions of the reference speed of sound c_{ref} at the reference frequency $f_{\mathrm{ref}} = 0.5\,\mathrm{MHz}$ obtained in the synthetic tests. Additionally, the true model and the result of a traveltime tomography considering bent rays, as described by Dapp (2013) and kindly provided by the Institute of Data Processing and Electronics at the Karlsruhe Institute of Technology, are shown. For the sake of better visualization the range of c_{ref} is clipped and magnified views of the tumor phantoms are shown. In the case of acoustic FWI and the traveltime tomogram, c_{ref} refers to the frequency-independent speed of sound c.

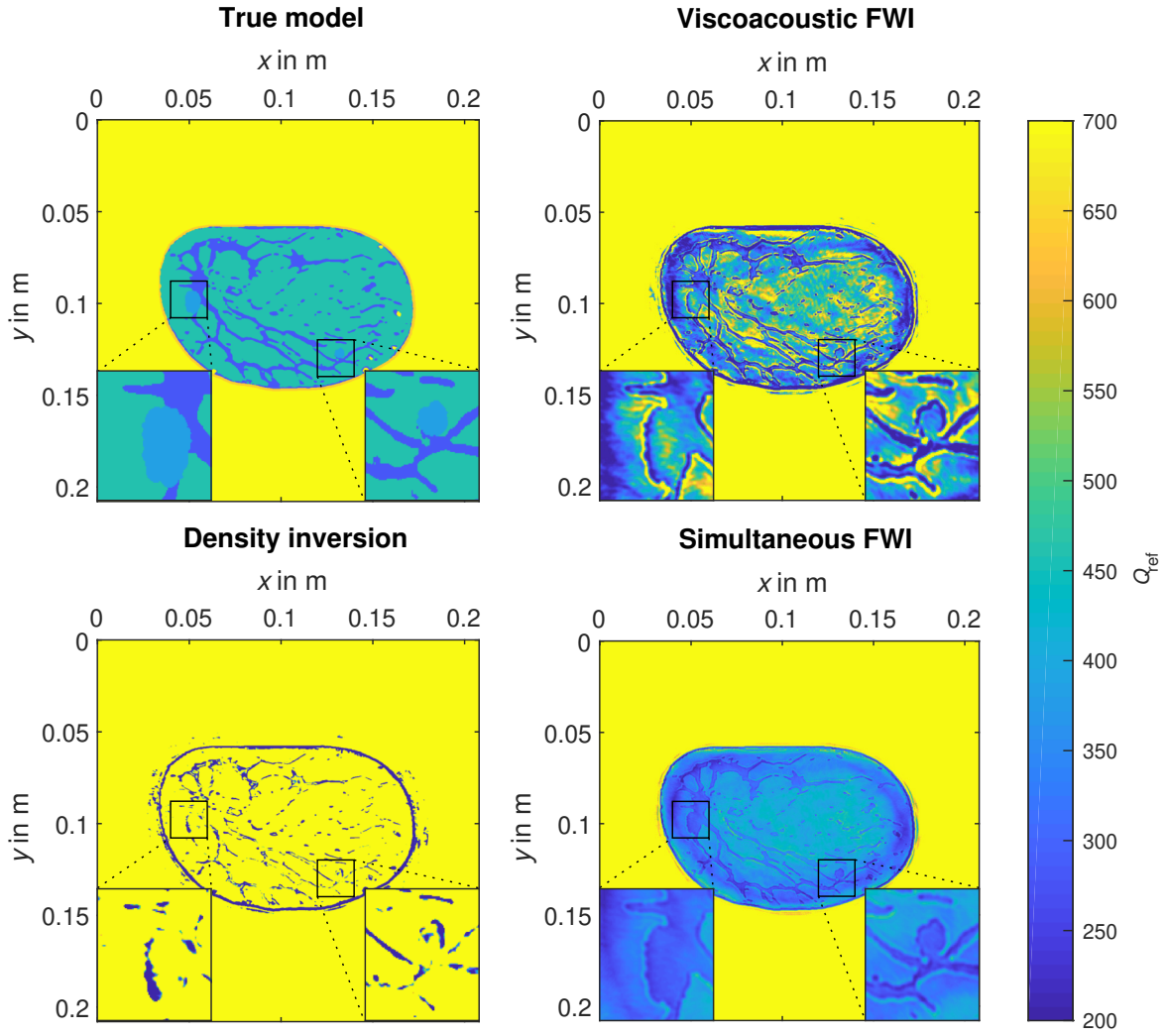

Figure 4.15: Reconstructions of the reference quality factor Q_{ref} at the reference frequency $f_{\mathrm{ref}} = 0.5\,\mathrm{MHz}$ obtained in the synthetic tests. Additionally, the true model is shown. For the sake of better visualization, the range of Q_{ref} is clipped and magnified views of the tumor phantoms are shown.

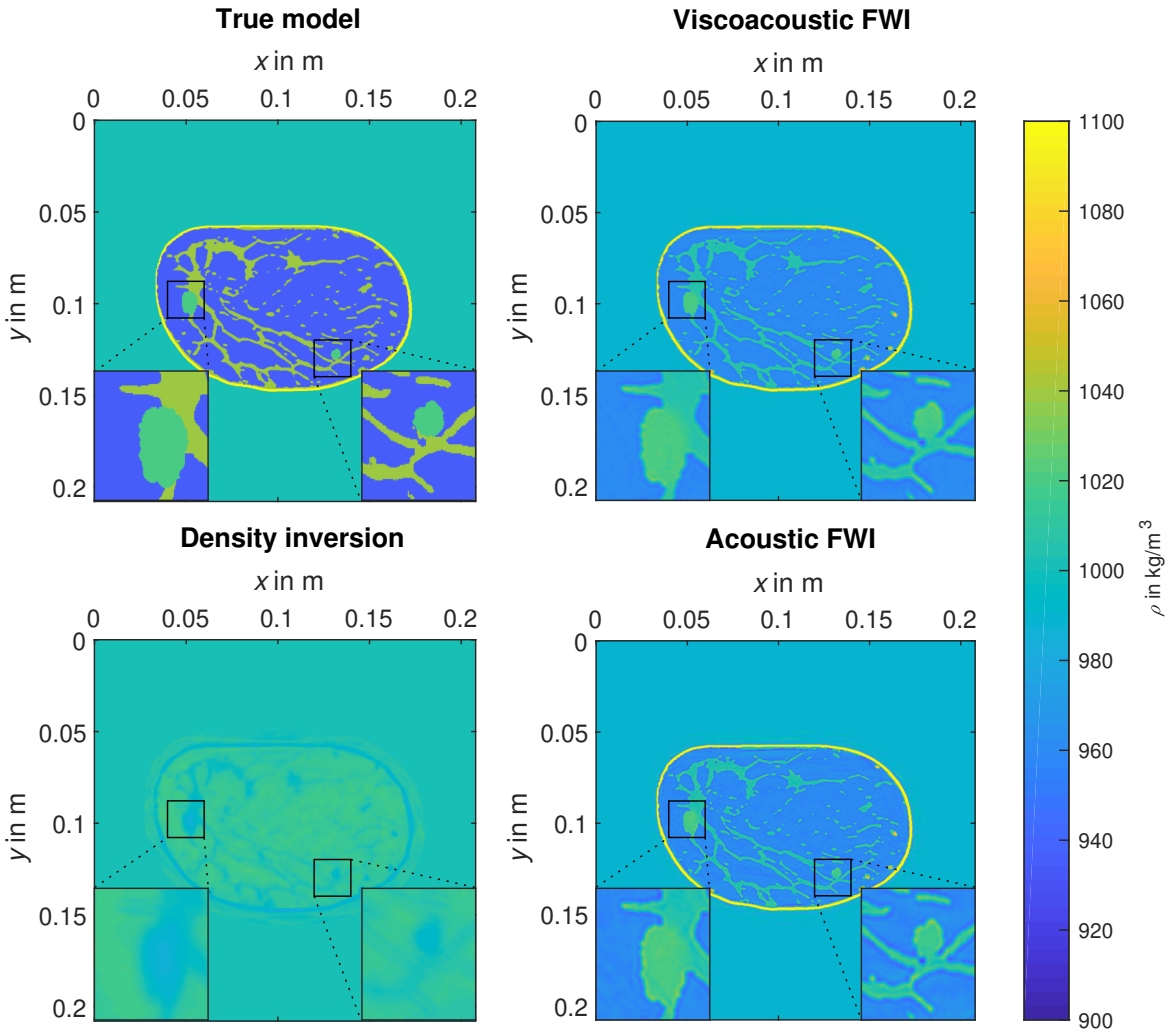

Figure 4.16: Reconstructions of the density ρ obtained in the synthetic tests. Additionally, the true model is shown. For the sake of better visualization the range of ρ is clipped and magnified views of the tumor phantoms are shown. Due to the low information content of a density model obtained by scaling the speed of sound model and only small differences to the acoustic and viscoacoustic FWI, the results from the simultaneous FWI are not shown here.

4.4.2 Crosstalk test

In this section I present two synthetic tests to investigate the crosstalk between the speed of sound, the density and the quality factor. I consider the speed of sound and density models as used in the previous test and an independent spatial distribution of the quality factor.

Crosstalk test 1
Based on the prior tests, I use the workflow as specified for the "viscoacoustic FWI" in table 4.4. The true and initial models are shown in figure 4.17. The quality factor model is specified with realistic values, namely a mean value of 400 within the breast and anomalies with a quality factor of 300. The inverted models demonstrate nearly no crosstalk from the quality factor to the reconstructed speed of sound model but very strong crosstalk vice versa. In the reconstructed quality factor the anomalies are not even detectable.

Crosstalk test 2
Based on the first crosstalk test, I use much lower quality factors (150 as a mean value within the breast and 80 for the anomalies as shown in figure 4.18) in this second test to enhance the effects of attenuation as would be the case if higher frequencies were used. Furthermore, I use the true speed of sound and density models shown in figure 4.17 as initial models and exclusively invert the attenuation to simulate optimal conditions.
Even in this case there is very strong crosstalk between the speed of sound and the quality factor. However, the structures in the quality factor model now become visible despite they are still superimposed by the structures which are existent in the speed of sound and density models. The mean values are reconstructed accurately.

Conclusion
The tests demonstrate very strong crosstalk from the speed of sound and density to the quality factor. However, the results from the reconstruction test presented in section 4.4.1 show, that the quality factor can accurately be reconstructed if the geometry of the structures is the same in all three models. Based on my best knowledge, it seems to be reasonable to consider this in realistic applications because the spatial distribution of all three parameters is determined by the distribution of breast tissues. Thus, the inversion for attenuation is supposed to provide adequate results despite the ability to reconstruct spatially independent anomalies is very restricted.

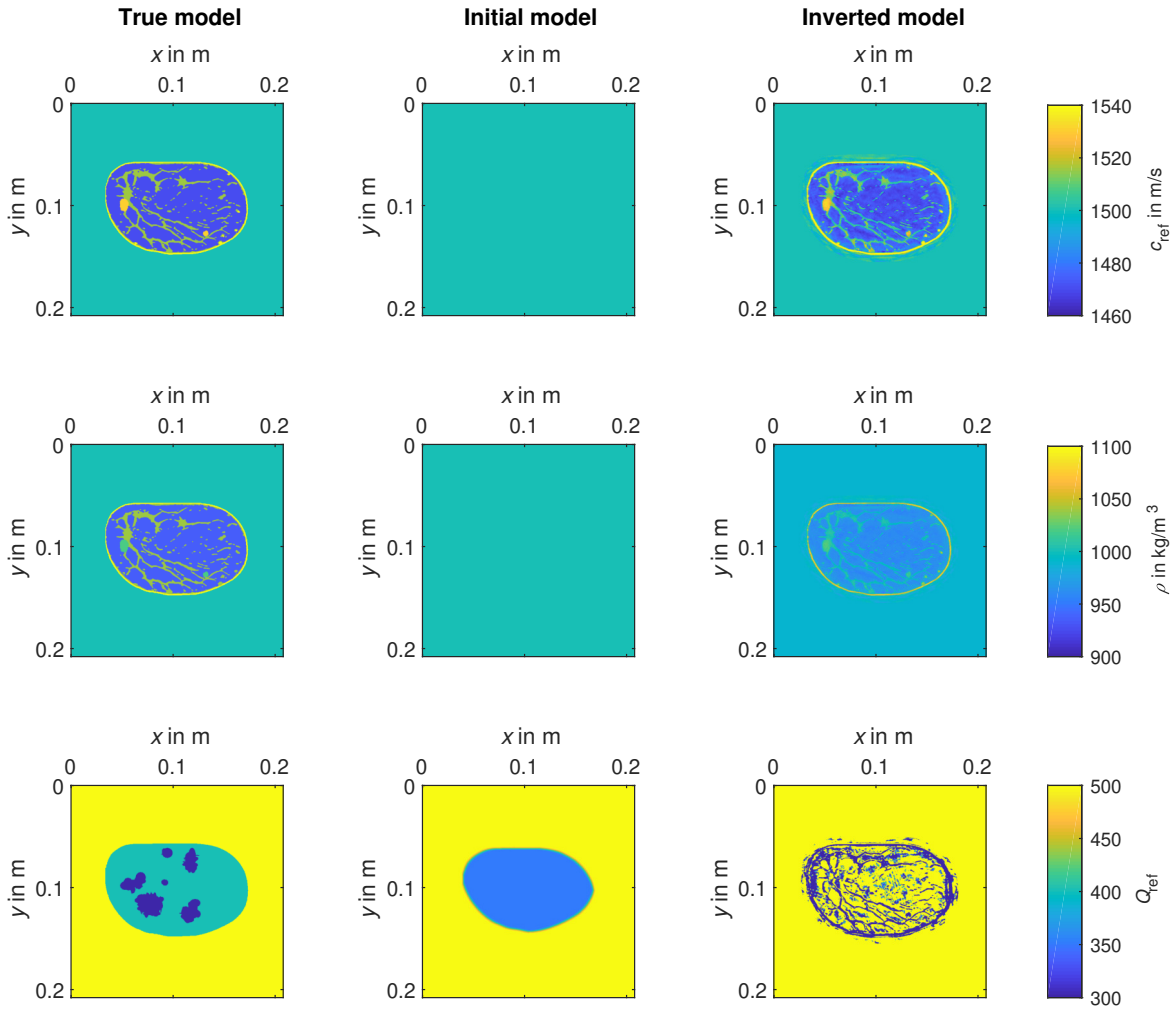

Figure 4.17: True, initial and final inverted models of the reference speed of sound c_{ref}, reference quality factor Q_{ref}, both defined at the reference frequency $f_{\mathrm{ref}} = 0.5\,\mathrm{MHz}$, and the density ρ in the first crosstalk test. For the sake of better visualization, the shown ranges of the parameters are clipped.

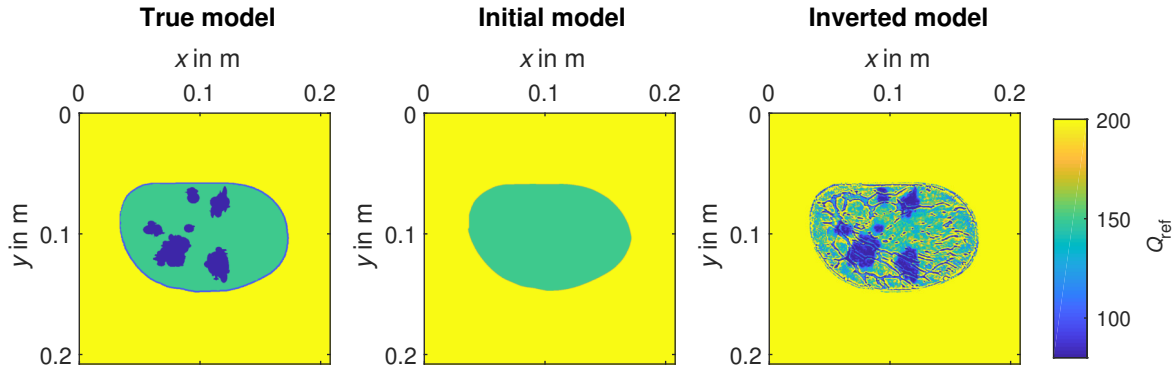

Figure 4.18: True, initial and final inverted models of reference quality factor Q_{ref} defined at the reference frequency $f_{\mathrm{ref}} = 0.5\,\mathrm{MHz}$ in the second crosstalk test. For the sake of better visualization, the shown range of the quality factor is clipped.

Chapter 5

Application of full-waveform inversion on KIT 3D USCT II clinical datasets – a feasibility study

The Institute of Data Processing and Electronics at the Karlsruhe Institute of Technology (KIT-IPE) is developing the first automated breast ultrasound system for in-vivo imaging with a full three-dimensional acquisition geometry to overcome the limitations of two-dimensional systems, which are described in section 2.2.3. The system is designed in order to create conditions as optimal as technically possible for ray-based migration and tomography algorithms and has already been tested in a first clinical study. It is described in section 5.1.

Within the scope of this work I perform a feasibility study based on a clinical dataset of a volunteer in order to address the question, whether it is possible to apply three-dimensional full-waveform inversion (FWI) on data acquired with the current prototype of the system, called KIT 3D USCT II. The main focus of this chapter lies on the identification of challenges and restricting factors related to the characteristics of this specific ultrasound data acquisition device and the application of 3D FWI on breast ultrasound datasets in general, which is described in section 5.3. Furthermore, I would like to propose potential approaches to deal with these difficulties.
For the sake of simplicity, limited computational resources and better illustration, several steps of this study are performed with a two-dimensional subset of the full three-dimensional dataset and the conclusions are extended to the three-dimensional case. This two-dimensional subset is described and analyzed in section 5.2. The used two-dimensional acquisition geometry is selected to be similar to the geometry used in the synthetic tests presented in chapter 4 in order to make the measured and ideal synthetic data comparable.

5.1 KIT 3D USCT II

In this section I describe and analyze the KIT 3D USCT II, the current prototype of the first automated breast ultrasound system for in vivo imaging with a full three-dimensional acquisition geometry developed at the KIT-IPE.
The data are acquired in a semi-ellipsoidal aperture with a diameter of 26 cm and a height of 18 cm embedded in a patient's bed, shown in figure 5.1, which contains the whole electronics. During data acquisition patients lie prone on top of the device with one breast freely suspended in the water-filled aperture which is equipped with 157 quadratic transducer array systems (TAS).

Technical specifications related to the data acquisition are given in section 5.1.1 and the acquisition geometry is described in detail in section 5.1.2.

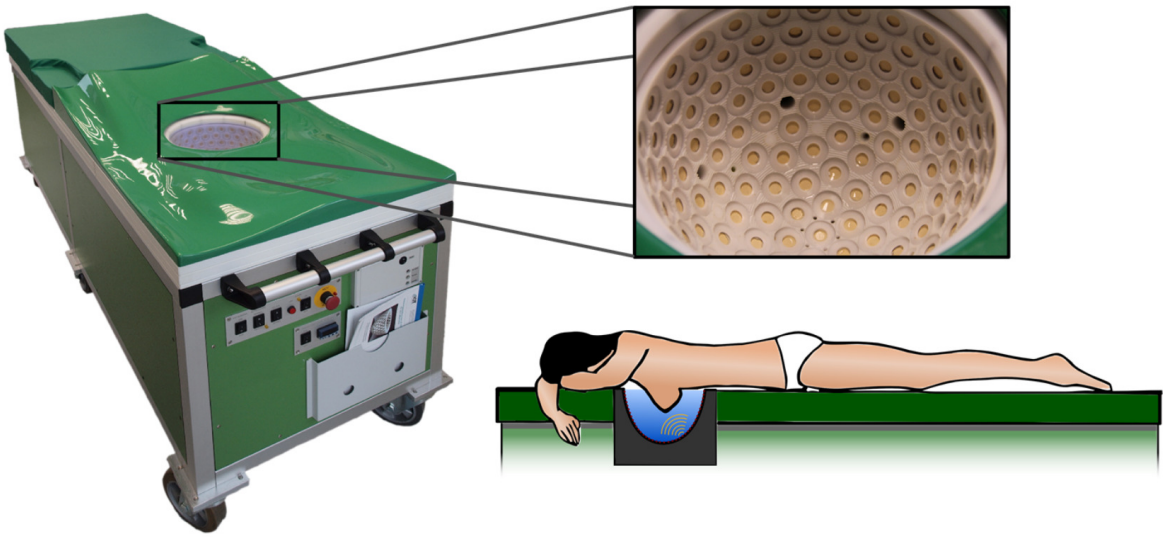

Figure 5.1: 3D ultrasound computer tomography system prototype developed by the Institute for Data Processing and Electronics at the Karlsruhe Institute of Technology. On the left side, the whole system is shown. At the top right, a magnified view of the transducer aperture consisting of 157 transducer array systems is shown. At the bottom right, the positioning of a patient during data acquisition is shown (Ruiter et al., 2018a).

5.1.1 Technical specifications

All technical specifications given in this section are taken from Ruiter et al. (2018a). Each of the 157 implemented TAS consists of nine receiver and four source elements whose structure and characteristics are investigated in detail in section 5.3.5. Hence, the data from 628 sources are observed at 1413 receivers yielding in total 887 364 seismograms, or A-scans, per measurement. A massive parallel data acquisition is implemented to reduce the acquisition time as much as possible in order to minimize

movements of the breast during the measurement and to make the procedure clinically applicable. Furthermore, the data are bandpass-filtered between 1.67 MHz and 3.33 MHz during data acquisition before the storage process in order to enable bandpass undersampling which allows to sample a bandpass-filtered signal below the sample rate determined by the Nyquist–Shannon sampling theorem (see equation 3.44) in such a way that it is still possible to correctly reconstruct the signal afterwards. By doing so, the data rate and the time needed for data storage is reduced by a factor of six. The memory required for storage is roughly reduced from 11 GB to 1.8 GB. However, these benefits go at the expense of the irreversible removal of the low-frequency components which are a crucial factor for the convergence and robustness of FWI.
The whole aperture is rotatable and vertically translatable to improve the illumination of the breast by changing the locations of the sources and receivers (more information follows in section 5.1.2). Usually the measurement is performed in ten different positions which yields a total storage size of 36 GB for the bandpass undersampled data or 220 GB for the raw data of both breast. Moreover, usually a reference measurement in pure water is performed prior to the actual measurement with immersed breast. The obtained data can be used for several purposes, e.g. the inversion of the source time function due to the great advantage that the propagation medium (pure water) is well known.

The waste heat of the technology and computing system placed in the patient's bed, which are used for data acquisition, data storage and fast computation of ray-based reconstructions of the breast, as well as heat transfer from the patient's breast lead to small spatial and temporal fluctuations of the temperature within the water bath despite a thermostat-controlled heating system being implemented. The water is heated in order to make the measurement process more comfortable for the patients. Furthermore, the desired water temperature ought to minimize the discrepancy between the temperature-dependent speed of sound in water and the mean speed of sound in the breast in order to improve the reflectivity reconstructions obtained with synthetic aperture focusing techniques which assume a constant speed of sound model.
However, the temperature is neither constant in space nor in time. Hence, one temperature sensor per TAS and two additional calibrated temperature sensors are implemented in the aperture which make it possible to reconstruct the temperature and the related speed of sound variations. In the following, I estimate the temperature fluctuations based on the temporarily averaged temperature data of each TAS for each position which are provided in addition to the actual pressure data.
The temperature averaged over all aperture positions observed at different TAS, which is shown in the left image of figure 5.2, is used to estimate spatial variations of the temperature. The water temperature ranges from 24.2 °C to 26.6 °C which corresponds to a speed of sound range from $1494.5\,\mathrm{m\,s^{-1}}$ to $1500.9\,\mathrm{m\,s^{-1}}$ according to an empirical fifth-order polynomial approximation of the speed of sound in water as a function of temperature under atmospheric pressure published by Marczak (1997). I assume the effects of spatial temperature fluctuations not to be negligible because the speed of sound variations within the breast which ought to be reconstructed are in the same or-

der of magnitude. As a simple approach, I propose to use the speed of sound averaged over all relevant TAS and aperture positions for the generation of the initial model and to allow model updates in the water to reconstruct the speed of sound variations related to temperature fluctuations. However, the gradient has to be tapered in the vicinity of sources and receivers to avoid artifacts in these regions.
Based on the temperature averaged over all TAS related to different aperture positions and times of measurement, which is shown in the right image of figure 5.2, I assume temporal fluctuations to be negligible. The temperature increases almost linearly by 0.25 °C during the whole measurement , assuming each measurement related to a different aperture position to take approximately the same time. Even if all aperture positions were considered the speed of sound variations would be less than $1\,\mathrm{m\,s^{-1}}$ according to Marczak (1997).
The density of water also depends on the temperature. Thus, it is reasonable to calculate the density used to parameterize water in the initial model in consideration of the available temperature data as well, e.g. as proposed by Kell (1975). However, the impact of these density variations on the acquired data is much smaller than from the aforementioned speed of sound variations.

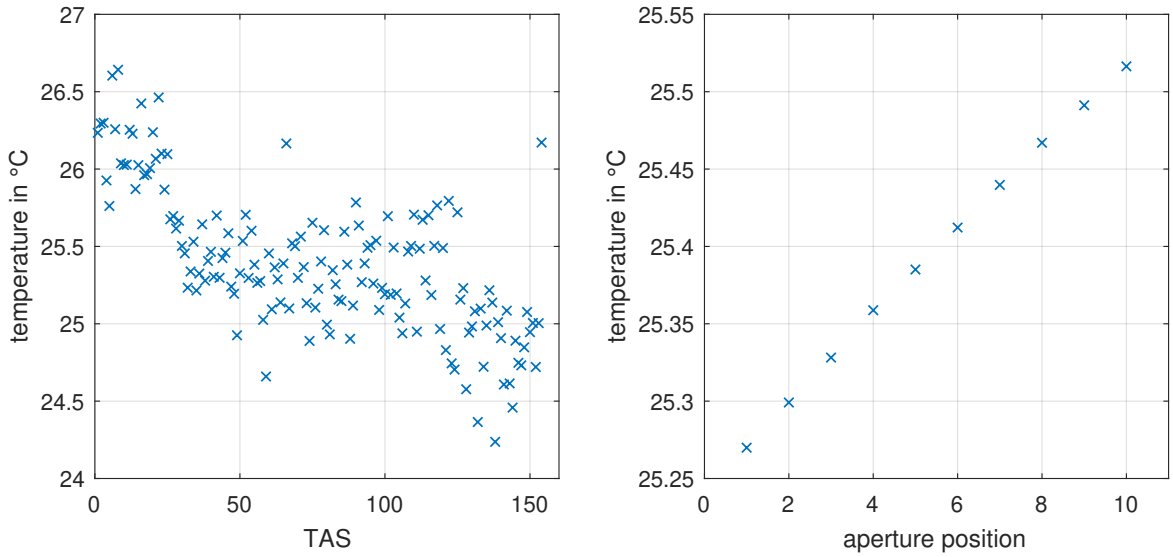

Figure 5.2: Spatial and temporal fluctuations of the water temperature during the data acquisition. In the left image, the average temperature of all aperture positions observed at different transducer array system (TAS) is shown. Higher numbers on the TAS-axis correspond to lower positions within the aperture. In the right image, the average temperature of all TAS for all ten aperture positions is shown. Higher numbers indicating the aperture position correspond to later measurements.

The data acquisition in one aperture position takes approximately ten seconds. This is much longer than the period of a cardiac cycle leading to movements of the breast. Ruiter et al. (2016) estimate the movements of breast during data acquisition based on reflectivity reconstructions related to individual aperture positions using an intensity-based image reconstruction algorithm. According to this work, breasts move on average

4.9 mm during data acquisition in one aperture position. In consideration of ultrasound waves having wavelengths in the same order of magnitude, e.g. the wavelength related to the center frequency of the implemented transducers $f_c = 2.5\,\mathrm{MHz}$ is about 0.6 mm, these movements definitely affect the results of FWI.
The movement of the aperture from one to another position takes approximately forty seconds, yielding a total duration of approximately eight minutes for data acquisition of one breast in ten aperture positions. Thus, the patient must breathe between measurements in different positions leading to additional movements of the breast. More information and potential ways to deal with problems related to movements of the breast are presented in section 5.3.1.
According to a first clinical study, the whole measurement procedure takes about one hour per patient. In addition to the actual time used for data acquisition, this includes a preparation time required for disinfection of the patient's bed, dealing with patient information, positioning of the patient and exchanging and heating the water in the aperture.

5.1.2 Acquisition geometry

The acquisition geometry is determined by the positions of the 157 implemented transducer array systems which are spread over a semi-ellipsoidal aperture as shown in the upper left image of figure 5.3. The whole aperture can be rotated and translated in the vertical direction. The resulting movements are shown for one exemplary TAS in the upper right image. The aperture is always elevated between two subsequent positions to ensure that the water bath is completely filled as the water can drain at the top edge of the aperture but no water should be added in order not to disturb the temperature field within the water bath (see section 5.3.2).
In the lower left image, the detailed structure of a TAS is shown. Each TAS consists of nine receiver and four source elements whose characteristics are analyzed in detail in section 5.3.5. Each element, in turn, consists of four internally connected quadratic subelements with a side length of 0.4 mm. They are implemented in two rows and two columns with a gap of 0.1 mm between each subelement.
In the lower right image, the acquisition geometry related to the two-dimensional subset presented in section 5.2 is shown. All three receiver elements of the central row and one source element of the lower row of each TAS placed in the second level in the fourth aperture position are used. However, some receiver and source elements (marked in red) did not perform properly and, thus, the affected data have to be ignored. The selection criteria for using these specific sources and receivers are described in section 5.2. More information about defective transducer elements is given in section 5.3.2. Furthermore, the rough position and shape of the breast is shown in black. This information is extracted from the reflectivity reconstruction shown in figure 5.12.

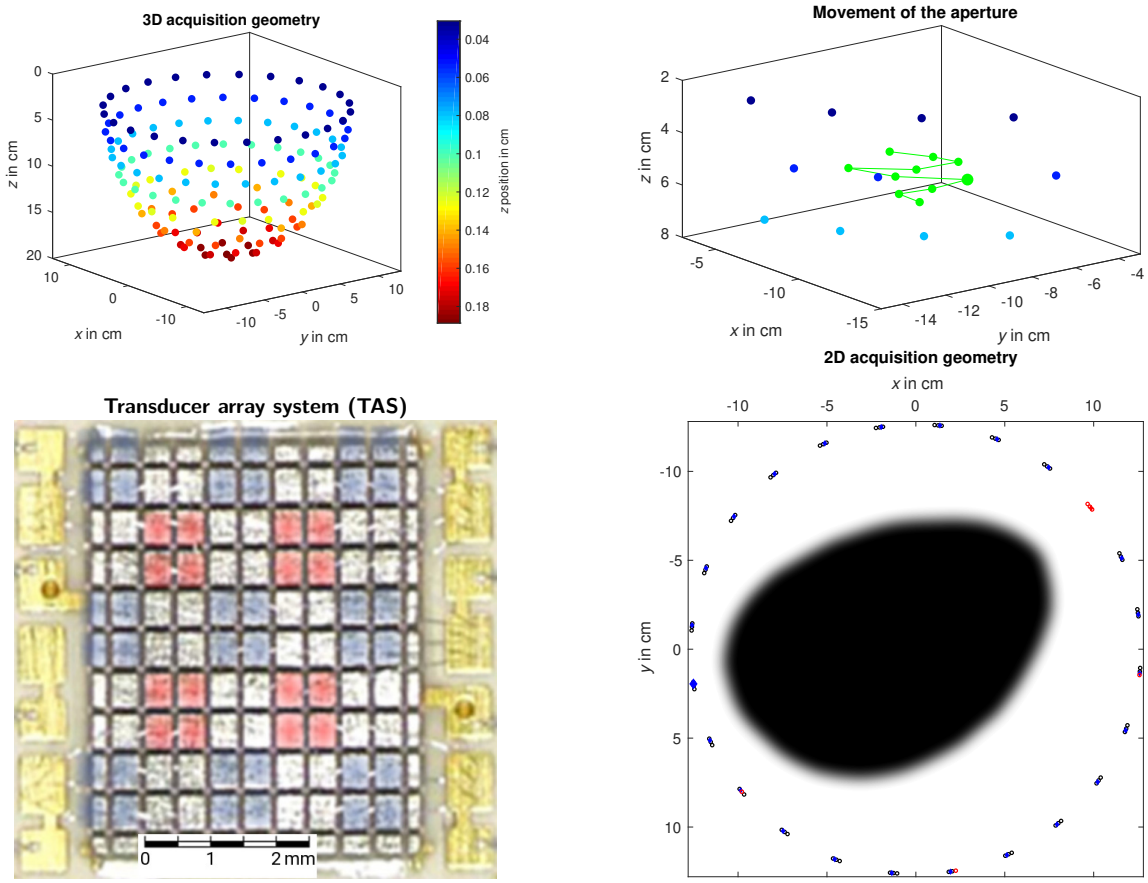

Figure 5.3: Acquisition geometry of the KIT 3D USCT II. In the top left image, the positions of the 157 transducer array systems (TAS) on the semi-ellipsoidal aperture are shown. The TAS are color-coded with respect to their z-coordinate in order to make it easier to differentiate between the various level heights. In the top right image, the movement of the aperture is shown in green in a magnified view of the acquisition geometry. The green dots mark the ten positions of an exemplary TAS to illustrate the movement. The lowest position corresponds to the first measurement. The acquisition geometry shown in the upper left image corresponds to the fourth position. In the lower left image, a magnified view of one TAS, consisting of nine receivers elements (blue) and four source elements (red), is shown. Each element, in turn, consists of four internally connected quadratic subelements. A scale bar was added to the original picture adopted from Zapf et al. (2018). In the lower right image, the acquisition geometry related to the two-dimensional subset presented in section 5.2 is shown. All three receiver elements of the central row (black circles) and one source element of the lower row (blue diamonds) of each TAS of the second level in the fourth position, which are marked with medium blue in the upper left image, are used. The large blue diamond marks the active source pertaining to the exemplary shot gather shown in figure 5.5. Defective source and receiver elements are marked in red. The approximate position and shape of the breast is shown in black.

5.2 Analysis of two-dimensional subset

In this section I analyze a clinical dataset which was kindly provided by the Institute for Data Processing and Electronics at the Karlsruhe Institute of Technology. The data were acquired with the KIT 3D USCT II in order to image a healthy breast of a volunteer for test purposes.
For the sake of simplicity and in order to improve the comparability between this clinical dataset and the dataset used in the synthetic tests (see section 4.3.2), the analysis is based on a two-dimensional subset of the full three-dimensional dataset. This approach is used in order to simplify the identification of wave phases and disturbances which were not considered in the ideal forward modeling of the synthetic data.

The acquisition geometry pertaining to the two-dimensional subset is shown in the lower right image of figure 5.3. The related sources and receivers were selected according to the following considerations:
The transducer array systems (TAS) and therefore the receivers are very sparsely distributed over the aperture which leads to problems regarding the spatial sampling of the wavefields (see section 5.3.7). In order to consider the maximum number of TAS in one plane, the selection is restricted to the first and second row of TAS (counting from top to bottom) as they are both equipped with 24 TAS while all other rows contain fewer TAS. I use the second row based on its larger distance to the highly reflective water surface and breastbone in order to avoid the existence of related reflected phases in the measured data. In the optimal case, the source and receiver elements would be located in the same plane. However, this is not possible due to the internal structure of a TAS as shown in the lower left image of figure 5.3. The vertical distance between the source and receiver elements is minimized to 1 mm by using neighboring rows. The decision to use receiver elements of the central row and source elements of the lower row is made in order to select as few as possible defective transducer elements.

As opposed to the synthetic tests, a sweep signal which excites ultrasound waves in a frequency range between approximately 1.5 MHz and 3.5 MHz is used by the KIT 3D USCT II. An estimation of the actual source signal is shown in figure 5.4. It corresponds to the electric signal which is send to the sources but additionally takes the effects of the implemented data acquisition hardware including amplifiers and frequency filters, e.g. the bandpass filter with a lower and upper cutoff frequency of 1.67 MHz and 3.33 MHz, respectively, which is applied to enable bandpass undersampling, into account. The accuracy of this estimation is evaluated in section 5.3.4.

In figure 5.5 an exemplary shot gather is shown. The active source is marked with a large symbol in the lower right image of figure 5.3. Additionally, the data related to the reference measurement which was performed in pure water prior to the actual measurement are shown in order to improve the interpretability of the measured data and to demonstrate the effects of the breast on the propagated waves.

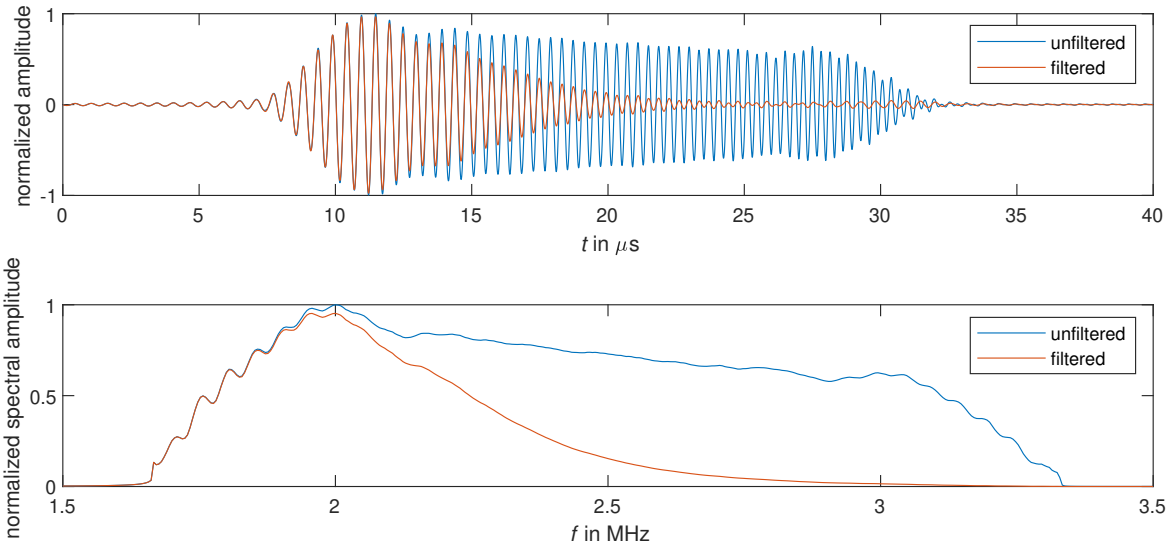

Figure 5.4: Estimation of the source signal used by the KIT 3D USCT II. In the upper image, the estimated time-domain source signal and the filtered signal using a twelfth-order Butterworth lowpass filter with a cutoff frequency of 2.2 MHz which is used for the discretization tests presented in section 5.3.3 are shown. Both signals are normalized with respect to the maximum of the unfiltered signal. In the lower image, the related amplitude spectra are shown.

Raw data are shown as I was not able to significantly increase the analyzability of the dataset by preprocessing it. Inter alia, various frequency filters and correlation with the estimated source wavelet were tested. The latter one is usually applied in seismics if sweep signals are used in order to reduce the complexity of seismograms. More information about the deconvolution are presented in section 5.3.6.
It is hardly possible to distinguish different phases in the shot gather due to the usage of the sweep signal. Furthermore, not only the amplitudes but also the waveforms depend heavily on the receiver distance or emission and incidence angle as is shown by the reference data (see section 5.3.5), making the identification of phases even more complicated. The receiver at a receiver distance of 0° is located at the same TAS which triggers the active source and suffers from strong electronic crosstalk. In fact, the signal between approximately 0 µs and 50 µs is caused by this phenomenon and is not related to observed pressure variations. The signals arriving at $t \approx 80\,\mu s$ at 0°, 30° and 330° receiver distance can be related to reflections at the skin. Signals arriving later are associated with reflections in the interior of the skin. The direct wave is neither visible on the measured nor on the reference data. The first signals arriving at receivers between 120° and 240° can clearly be associated with the refracted aka transmitted wave which is highly damped by the breast tissue. The effects of the anelastic attenuation are much larger on these measured data as compared to the synthetic, forward modeled data as much higher frequencies are used and the examined breast is significantly larger than the numerical model. Later arrivals are associated with the critically refracted wave, which propagates along the outer boundary of the skin, and scattered phases. The dominant signal observed at the remaining, intermediate receivers are associated

with the critically refracted wave based on the position and extent of the breast shown in figure 5.3 and the observation that the signals arrive slightly earlier than the direct wave recorded in the reference measurement. The critically refracted wave is supposed to be superimposed by the direct wave but this signal cannot be identified due to its low amplitude. Based on a purely visual evaluation, the signal-to-noise ratio seems to be reasonable.

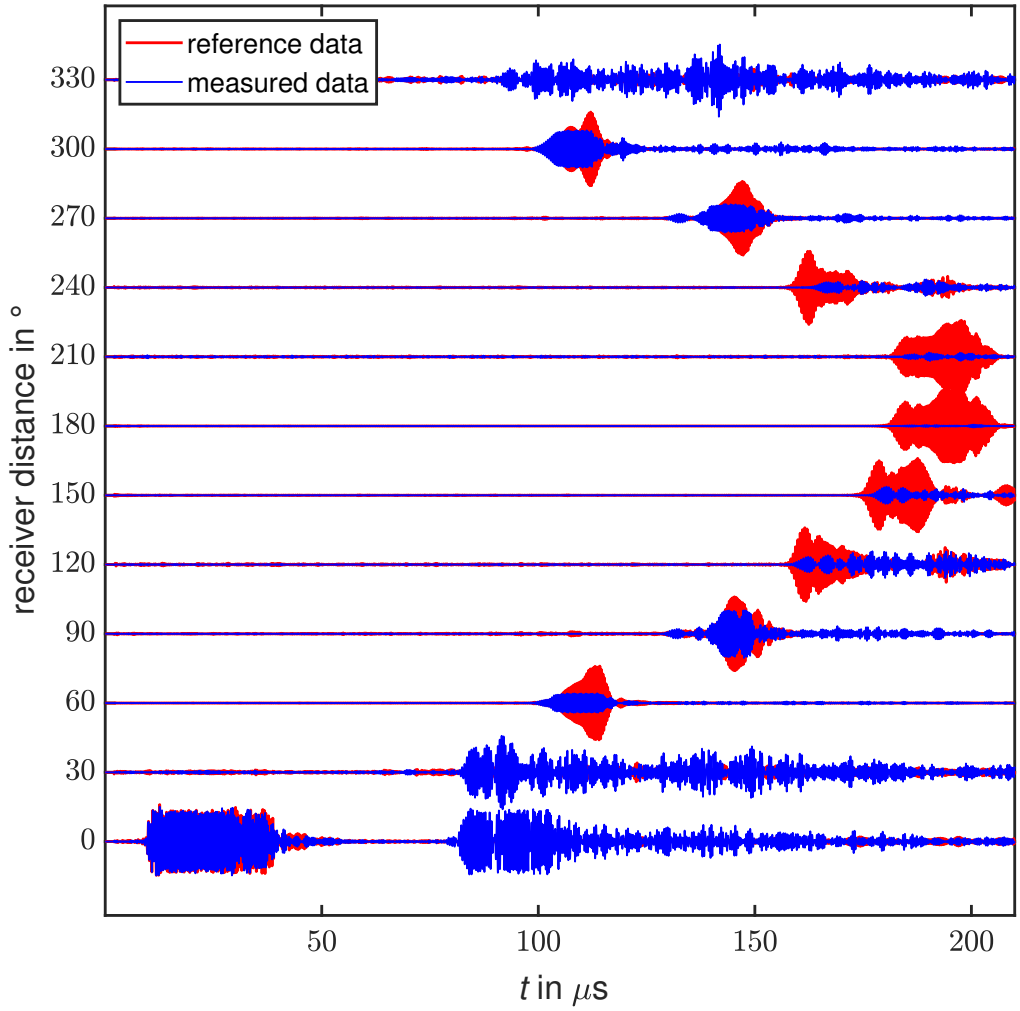

Figure 5.5: Exemplary shot gather pertaining to the source marked with a large symbol in the lower right image of figure 5.3. The angle specifying the receiver distance is counted counter-clockwise starting from the active source. In order to illustrate the effects of the breast on the wave propagation both datasets related to the measurement with the immersed breast (measured data) and in pure water (reference data) are shown. The amplitudes of both datasets are normalized with respect to the common maximum of both datasets for each source-receiver distance.

5.3 Challenges and limiting factors

This section is the central part of the feasibility study, in which I present several challenges related to the application of FWI on data acquired with the KIT 3D USCT II. The section is concluded with an assessment of the feasibility in consideration of all presented challenges and difficulties.

5.3.1 Changes of the propagation medium in space and time

In this section I discuss spatial and temporal changes of the propagation medium occurring during the data acquisition caused by temperature variations and movements of the breast.

Based on the information given in section 5.1.1 the temperature of the water increases during the measurement by approximately 0.25 °C when data are acquired in all ten aperture positions. Related variations of the speed of sound are less than $1\,\mathrm{m\,s^{-1}}$. A very pessimistic estimation for a maximum propagation path of approximately 25 cm and a variation of the speed of sound of $1500\,\mathrm{m\,s^{-1}} \pm 1\,\mathrm{m\,s^{-1}}$ along the whole propagation path would yield a traveltime perturbation of approximately 100 ns. The period of a wave with the center frequency $f_\mathrm{c} = 2.5\,\mathrm{MHz}$ is 400 ns. Considering that the actual occurring traveltime perturbations are even smaller because the water in the initial model can be parameterized with the speed of sound pertaining to the measured mean temperature. Furthermore, the waves do not propagate through water on the whole propagation path and the temperature and, thus, speed of sound within the breast are supposed to be approximately constant as humans are warm-blooded. Thus, the effects of temporal variations of the temperature are assumed to be negligible as related traveltime perturbations are significantly smaller than half a period.
The temperature data also indicate a spatial variation of the temperature within the water bath which is, however, relatively constant in time. This phenomenon can easily be considered during inversion by allowing model updates in the water. However, the gradient should be tapered in the vicinity of the sources and receivers to prevent the generation of artifacts in these regions. Due to the fact that all emitted and observed waves propagate through these regions, they have a great impact on the data. However, no updates are allowed there and, thus, the speed of sound in the initial model should be adapted to the individual temperature measurements of each TAS.

Movements of the breast during data acquisition are supposed to have a huge impact on reconstructions obtained by FWI. As described in section 5.1.1, the averaged sum of all moved distances of the breast in one aperture position is 4.9 mm, which corresponds to multiple wavelengths. If data acquired in multiple aperture positions are evaluated, the differences are expected to be even larger.
Due to the small recording time of 210 µs pertaining to one shot, movements occurring during a single shot are assumed to be negligible. However, numerous shots must be evaluated in FWI and, thus, the static position of the numerical breast model considered in the forward modelings does not always match the true position of the breast.

This could lead to the introduction of artifacts and produce great blurrings in the reconstructed models or even make the inversion unstable.
The position of the breast needs to be known accurately during the whole data acquisition in order to make it possible to consider the movements. This could be done, for instance, by migrating individual shots and extracting the information about the position of the breast as demonstrated by Ruiter et al. (2016). However, this approach would require additional high computational effort during FWI. Measurements in Doppler mode could probably be used to directly measure the displacement velocity of the breast with much lower computational effort. An assessment of the achievable accuracy and technical feasibility of this method goes beyond the scope of this work.
If accurate positions of the breast pertaining to the evaluated shots were available, then the position of the numerical breast model in the forward modelings could be translated to the true position. Furthermore, the calculated gradients of the individual shots would have to be shifted back to the initial position of the numerical breast model before they were summed and the model update applied. This approach assumes a simple three-dimensional translation, i.e. shearing and volumetric changes within the breast are neglected. In principle, there exist more sophisticated methods which could be adapted in order to consider deformation of the breast, e.g. a finite-element method proposed by Hopp et al. (2018) which is used to make the results from automated breast ultrasound and magnetic resonance imaging comparable, but they are realistic when taking into account the huge additional computational effort that would be required.

The effective suppression of breast movements is supposed to be the best option as complicated corrections with respect to the breast's position would not be necessary at all if it was successful. The SoftVue system, for instance, uses a soft anatomically-formed guide, called SEQUR breast interface, which touches the front of the breast to center, shape and steady it during the data acquisition (Delphinus Medical Technologies, 2018). However, I am not able to assess the effectiveness of such methods because there is very little public information available.

5.3.2 Disturbing signals

There may occur several signals during data acquisition that are not simulated and, thus, could lead to the introduction of artifacts in the reconstructed models. In the following, I discuss signals caused by the propagation of waves at structures which are not considered in the numerical models and the electronics of the KIT 3D USCT II.

Usually, absorbing boundary conditions or layers are considered at all boundaries of the model. However, in practice there exist highly reflective structures, e.g. the water surface, breastbone and bounding of the aperture. No reflections related to those structures could be identified in the analyzed shot gather (see figure 5.5) but they could be hidden as the usage of a sweep signal makes it almost impossible to distinguish between different phases using the raw data.

In principle, there could also propagate Scholte waves, a special type of surface waves which occur at the interface between a liquid and elastic solid medium, and critically refracted waves at the bounding of the aperture. However, the analyzed shot gather indicates that no such waves are generated as they would be expected to appear as nearly linear traveltime curves because the circle segments between neighboring transducers have the same length. At least the surface waves would be expected to be unambiguously identifiable due to their large amplitudes and dispersive propagation if they were excited during data acquisition. I assume those waves not to occur due to the beam-shaped radiation pattern of the sources which is discussed in detail in section 5.3.5.
The bounding of the aperture could be considered in the forward simulation if an accurate numerical model were available. However, the models used in the forward simulations would have to be extended and the range of the speed of sound that had to be considered for discretization would drastically increase. For the simulation of surface waves it would even be necessary to consider elastic or viscoelastic wave propagation. Both aspects would dramatically increase the computational cost. The water surface could be considered by using free surface conditions, e.g. described by Fichtner (2010), but the implementation would be complicated as the water surface is broken by the immersing breast.
Hence, I would suggest not to consider these structures in the forward modeling but taper the A-scans of measured and simulated data in order to remove related signals.

In the following, I discuss a second type of disturbing signals caused by the electronics of the acquisition device. As shown in the 0° trace in the shot gather in figure 5.5, receivers located at the TAS containing the active source suffer from strong electronic crosstalk. This cannot be correctly simulated and the related signal contains no information about the model at all. Thus, it must be muted.
Similar considerations apply for signals related to defective transducer elements as they can neither be simulated nor contain information about the propagation medium. Shot and receiver gathers pertaining to source or receiver elements which did not perform properly during data acquisition have to be ignored. In the full three-dimensional test dataset, 161 out of 1413 ($\approx 11\%$) receiver elements and 24 out of 628 ($\approx 4\%$) source elements are detected as defective based on their signal-to-noise ratio using a routine provided by the KIT-IPE.

5.3.3 Discretization & computational requirements

In this section I determine the spatial and temporal sampling intervals Δh and Δt analog to section 4.3.1 according to the strategy proposed in section 3.2.4. For the sake of simplicity, I calculate the discretization for the two-dimensional case and assume that it is also suitable for the three-dimensional case. I am aware of slight differences of the numerical dispersion occurring in two-dimensional and three-dimensional forward modeling. However, this approach is supposed to be reasonable for the purpose of an estimation of the size of the spatial grid and the number of timesteps in order to approximate the computational requirements.

Based on the results of the synthetic tests, I suggest to use the low-frequency components of the data exclusively. In order to obtain a reasonable estimation of the necessary discretization, I consider the estimation of the source wavelet which is filtered with a twelfth-order Butterworth lowpass filter specified by a cutoff frequency of 2.2 MHz, shown in figure 5.4. The filter is specified in order not to affect the maximum of the amplitude spectrum at 2 MHz.
I calculate sampling intervals based on the Nyquist–Shannon sampling theorem to prevent spatial and temporal aliasing, the criterion proposed by Köhn (2015) to obtain a first estimation of Δh and the Courant-Friedrichs-Lewy criterion to ensure numerical stability. Finite-difference operators second-order accurate in time and second-, fourth-, sixth- and eighth-order accurate in space, the minimum and maximum speed of sound $c_{\min} = 1400\,\mathrm{m\,s^{-1}}$ and $c_{\max} = 1700\,\mathrm{m\,s^{-1}}$ and the maximum frequency $f_{\max} = 3\,\mathrm{MHz}$ are considered. The results are shown in table 5.1.

Table 5.1: Comparison of the discretization proposed for the 3D KIT-IPE ultrasound system based on various criteria considering finite-difference operators second-order accurate in time and $2N$th-order accurate in space. The spatial and temporal sampling intervals Δh_{nyq} and Δt_{nyq} are calculated with the Nyquist–Shannon sampling theorems stated in equations 3.43 and 3.44. The spatial sampling interval $\Delta h_{\mathrm{köhn}}$ is calculated with the criterion proposed by Köhn (2015) stated in equation 3.45. The temporal sampling interval Δt_{cfl} is calculated with the Courant-Friedrichs-Lewy criterion stated in equation 3.42 considering $\Delta h_{\mathrm{köhn}}$. All calculations are based on the minimum and maximum speed of sound $c_{\min} = 1400\,\mathrm{m\,s^{-1}}$ and $c_{\max} = 1700\,\mathrm{m\,s^{-1}}$, respectively, as well as the maximum frequency $f_{\max} = 3\,\mathrm{MHz}$.

FD order $2N$	Δh_{nyq} in µm	Δt_{nyq} in ns	$\Delta h_{\mathrm{köhn}}$ in µm	Δt_{cfl} in ns
2	233	167	39	16
4	233	167	58	21
6	233	167	78	26
8	233	167	93	30

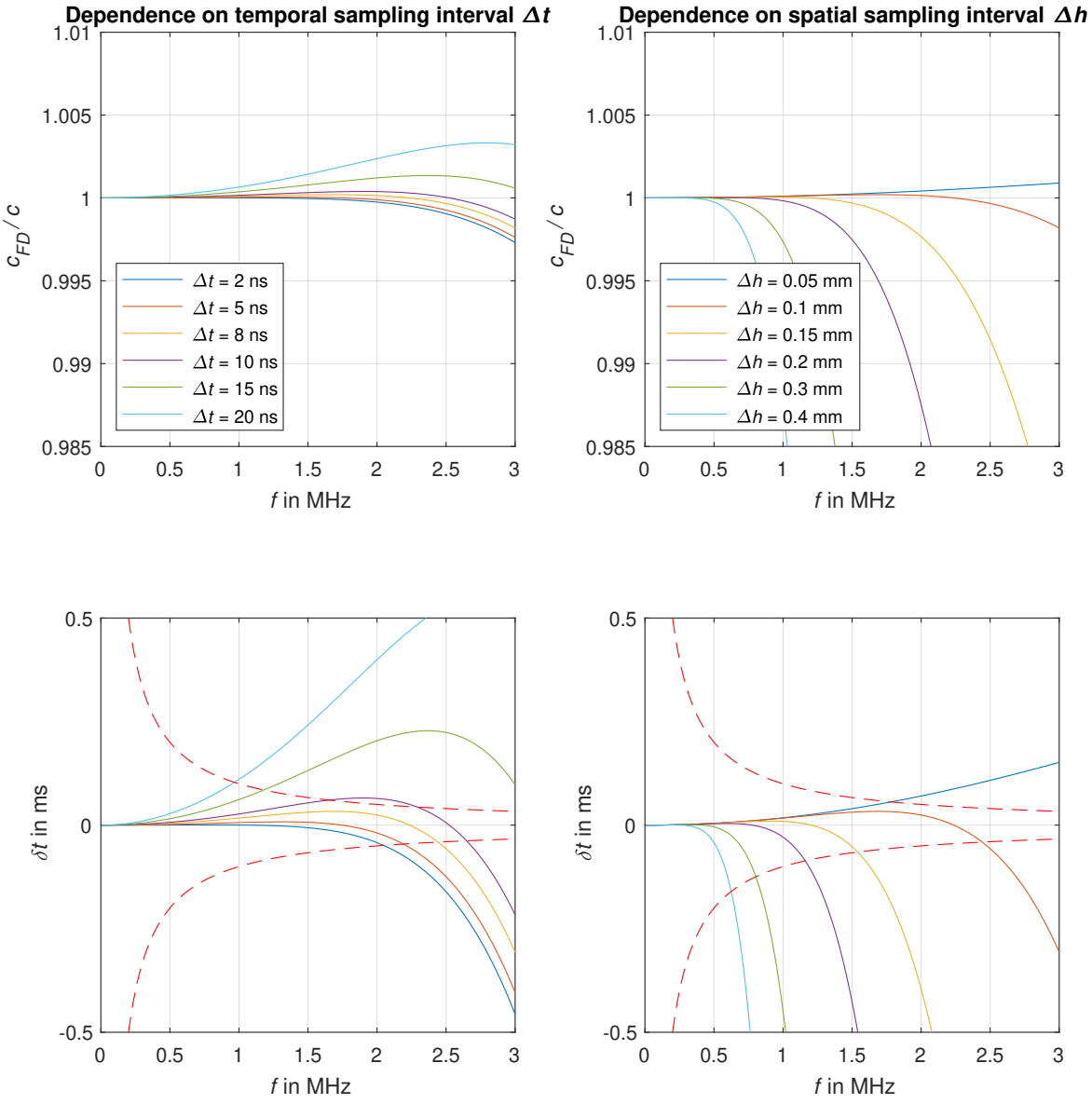

Figure 5.6: Analysis of numerical dispersion as a function of the discretization and frequency. On the left side, the spatial sampling interval is fixed at $\Delta h = 0.1\,\mathrm{mm}$ and several different temporal sampling intervals Δt are tested. Analogously, I investigate numerical dispersion for different spatial discretizations Δh with $\Delta t = 8\,\mathrm{ns}$. In the top row, the ratio of the true speed of sound $c = 1500\,\mathrm{m\,s^{-1}}$ and the numerical velocity of propagation c_{FD} of a plane wave propagating in x-direction is shown. Finite-difference operators second-order accurate in time and sixth-order accurate in space are used. In the bottom row, the difference between the true and numerical traveltime δt for the propagation distance $s = 25.32\,\mathrm{cm}$ is shown. The red dashed lines are defined by $|\delta t| = 0.1\,T(f) = 0.1/f$, where $T(f)$ denotes the period of a monochromatic wave with frequency f.

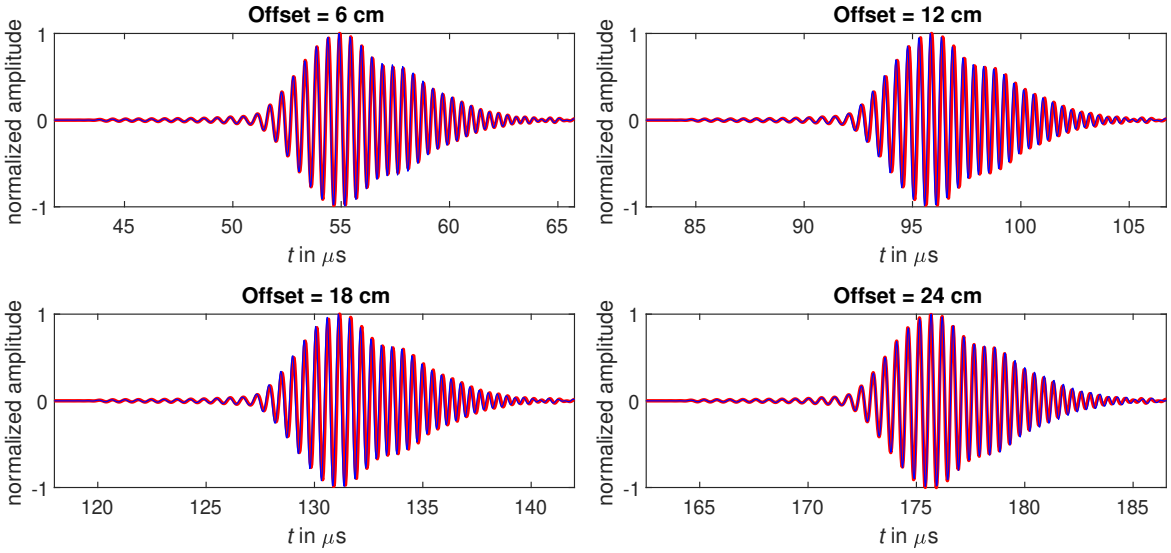

Figure 5.7: Comparison of finite-difference simulations (blue) and analytical solutions (red) at different source-receiver distances. Spatial and temporal sampling intervals $\Delta h = 0.1\,\mathrm{mm}$ and $\Delta t = 8\,\mathrm{ns}$, speed of sound $c = 1500\,\mathrm{m\,s^{-1}}$ and finite-difference operators second-order accurate in time and sixth-order accurate in space are considered. Data were generated with the filtered source signal estimation shown in figure 5.4.

The final discretization is determined according to criterion 3.51 in consideration of sixth-order accurate spatial FD operators, a speed of sound of $1500\,\mathrm{m\,s^{-1}}$ and a maximum propagation distance of 25.32 cm. As shown in figure 5.6, I obtain $\Delta h = 0.1\,\mathrm{mm}$ and $\Delta t = 8\,\mathrm{ns}$.
For a final assessment of the achieved accuracy the acoustic FD simulation in a homogeneous water model is compared with the analytical solution for different offsets. The discretization assures sufficiently accurate FD simulations as shown in figure 5.7.

Considering $\Delta h = 0.1\,\mathrm{mm}$, a spatial model extension of 25.32 cm by 25.32 cm by 15.92 cm in order to include all source and receiver elements and 20 additional gridpoints on each side of the model for the implementation of convolutional perfectly matched layers, the spatial grid would consist of $N_\mathrm{g} = N_\mathrm{x} \cdot N_\mathrm{y} \cdot N_\mathrm{z} = 2572 \cdot 2572 \cdot 1632 \approx 10^{10}$ points. Based on the temporal sampling interval $\Delta t = 8\,\mathrm{ns}$ and a recording time of 210 µs the FD time-stepping scheme would need to be solved $N_\mathrm{t} = 26250$. Hence, huge computational effort would be required for the forward simulations.

In the synthetic tests, a viscoacoustic forward simulation of one shot was computed in about 5 s on 400 cores of the ForHLR2 cluster at the Karlsruhe Institute of Technology. Performing a whole FWI required on average roughly 6 hours.
The product of N_g and N_t is proportional to the number of necessary floating-point operations and, thus, proportional to the required computational time. In consideration of a linear scaling between the number of used cores and the required computational time, one additional partial differential equation which needs to be solved in the 3D

forward modeling and the ratio between the product of N_g and N_t pertaining to the synthetic tests and the KIT 3D USCT II based on the estimations shown above, roughly 17 million cores as implemented in the ForHLR2 would be needed to be able to perform a viscoacoustic forward simulation of one shot in the three-dimensional model in about 5 s. Based on this estimation, I conclude that a modern supercomputer would be needed in order to apply FWI on a dataset acquired with the KIT 3D USCT II.
The usage of lower frequencies would reduce the computational costs, e.g. if transducers were used which would excite a source signal with a similar frequency content than in the synthetic tests (center frequency of 0.5 MHz, see section 4.2) and thus the same discretization could be used. The computational costs would then be reduced by roughly 94%. Nevertheless, even if such transducers were implemented in a future prototype, huge computational resources would still be required. As mentioned in section 2.2.3, much research is done in order to accelerate FWI, e.g. by developing efficient implementations on graphical processing units.

5.3.4 Source signal estimation

When FWI is applied on measured data, the source signal is a priori not accurately known and needs to be estimated for accurate modeling of the wavefields. For this purpose, I use the source time function inversion described in section 3.3.5. In the following, I invert the source signals of the 23 source elements related to the two-dimensional subset which is discussed in section 5.2 in order to examine the consistency of the source signals excited by different source elements.
The estimation of the source signals is performed using the provided filtered sweep shown in figure 5.4 as initial synthetic source wavelet and the filtered data of the reference measurement. The application of a twelfth-order Butterworth lowpass filter specified by a cutoff frequency of 2.2 MHz on the source signal and data allows me to discretize the model and wavefields for the required wave modeling according to section 5.3.3.
As opposed to the usual approach used in seismics where the source time function inversion is performed multiple times during FWI due to the increasing quality of reconstructed models of the subsurface in later iterations, the source time estimation in breast ultrasound only needs to be performed once prior to the application of FWI because the propagation medium in the reference measurement is well known. However, only the three receivers contained by the TAS located opposite to the active source element can be considered due to the transducer characteristics which are discussed in section 5.3.5.
The wave modeling required for the source time function inversion is performed using the two-dimensional approximation which implicitly considers line sources extended in the out-of-plane direction. Thus, the measured reference data must be transformed to correspond to such line sources. Therefore, I apply the direct wave transformation proposed by Forbriger et al. (2014), which, however, assumes the measured three-dimensional data to be excited by point sources. Although the point approximation is not valid for the implemented transducers, this approach is suitable for the consid-

ered receivers located opposite to the active source because there, the simulated data considering point sources and receivers agree with the data excited by the transducers except for a constant amplitude factor (see section 5.3.5).

According to the results shown in figure 5.8 the excited source wavelets are very similar to each other but they are delayed slightly differently. The provided source signal estimation also shows large agreement with the inverted source signals except for the delay and small differences in the amplitude.

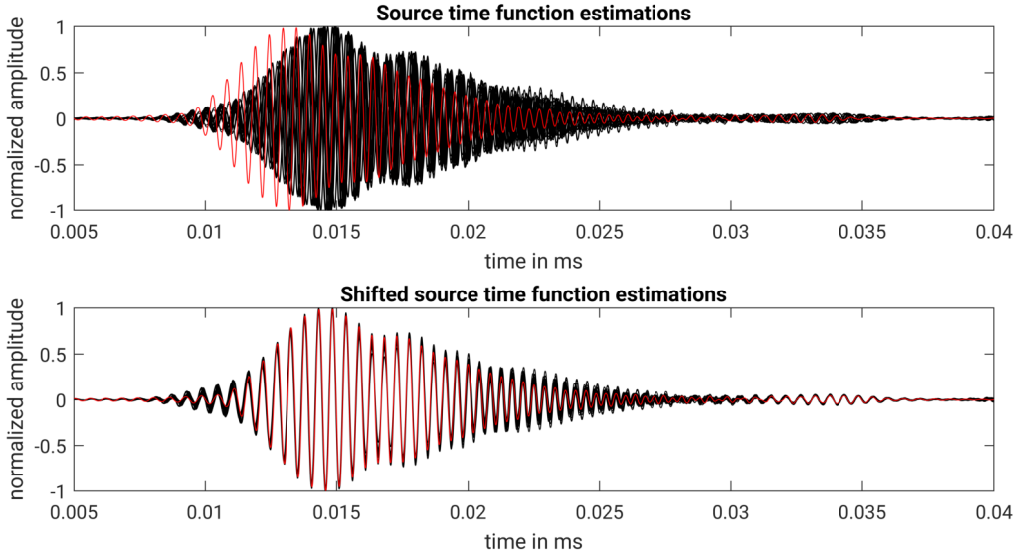

Figure 5.8: Estimated source time functions of the 23 used source elements for the two-dimensional subset described in section 5.2. The data were filtered with a twelfth-order Butterworth lowpass filter specified by a cutoff frequency of 2.2 MHz. In the upper image, the inverted source time functions are shown in black and the source signal estimation provided by the KIT-IPE is shown in red. In the lower image, the same signals are shown but they are time-shifted in order to obtain maximum agreement between the individual signals according to their crosscorrelations. Each signal is normalized to its maximum.

The inversion of the source signals excited by source elements related to TAS located at lower rows of the aperture is more complicated as there are no receivers located opposite to the active source elements with a nearly parallel orientation for which the transducer effects are negligible. This problem would be solved if it was possible to accurately simulate the transducer characteristics. This is investigated in section 5.3.5. Furthermore, an approach is proposed which transforms the measured data as they were approximately emitted and observed by point sources and receivers, respectively. Following this approach, it is not necessary to know the exact source signals and, thus, it also solves the problem regarding the source signal estimation of source elements related to TAS of the lower rows.

5.3.5 Transducer characteristics

The measured data pertaining to the reference measurement which are shown in figure 5.5 in section 5.2 clearly demonstrate that the point approximation which is usually considered in seismics is not valid for the implemented ultrasound sources and receivers as the amplitude and phase of observed waves heavily depends on the source-receiver distance or emission and incidence angle.
In the following, I simulate the transducers according to section 3.4 in order to analyze their emission and recording characteristics. At the end of this section, I propose a method how these characteristics could be considered in FWI.

In the first step of the analysis I investigate the radiation pattern of the source elements. Therefore, I consider the structure of the source elements which consist of four quadratic subelements with a side length of 0.4 mm which are arranged in two rows and columns with a gap of 0.1 mm between each subelement as shown in figure 5.3. On each subelement eleven times eleven point sources are evenly distributed as shown in the upper left image of figure 5.9 with a distance of 0.04 mm which is much smaller than the occurring wavelengths. The inverted source time function of the shot marked with a large symbol in figure 5.3 is used as source signal because the radiation pattern depends on the frequency content of the source wavelet. In order to observe the emitted waves in all directions I distribute 101 times 101 point receivers equiangularly with respect to the azimuth θ and elevation angle ϕ as shown in the upper right image of figure 5.9.
In the lower left image the emitted signal power measured at the point receivers is shown as a function of θ and ϕ. As all receivers are placed with the same distance to the center of the simulated source element, geometrical spreading does not distort the result. It is clearly visible that the source elements are heavily beam-forming as most of the energy is emitted orthogonally to the source element within a narrow central intensity maximum which is limited by the first-order minima caused by destructive interference. This phenomenon is clearly recognizable in the lower right image, in which the amplitude spectra of emitted signals for $\phi = 0°$ are shown as a function of θ. The red dashed lines approximately mark the first order diffraction minima as a function of θ and the frequency f or wavelength λ. They are calculated for a quadratic aperture with the side length a and the speed of sound $c = 1500\,\mathrm{m\,s^{-1}}$ for which the nth-order diffraction minima according to the Fraunhofer diffraction approximation are defined by (Szabo, 2014, chapter 6)

$$a\,\sin(\theta) = n\,\lambda \quad \Longleftrightarrow \quad f = \frac{c}{a\,\sin(\theta)}\,. \tag{5.1}$$

For the sake of simplicity, the source element is approximated as a single quadratic aperture with $a = 0.9\,\mathrm{mm}$ for the estimation of the first-order minima. Although the gap between the subelements is neglected, this estimation accurately predicts the position of the minima. For detailed information about beamforming and how it can be described using the diffraction formalism I refer to Szabo (2014, chapter 6).

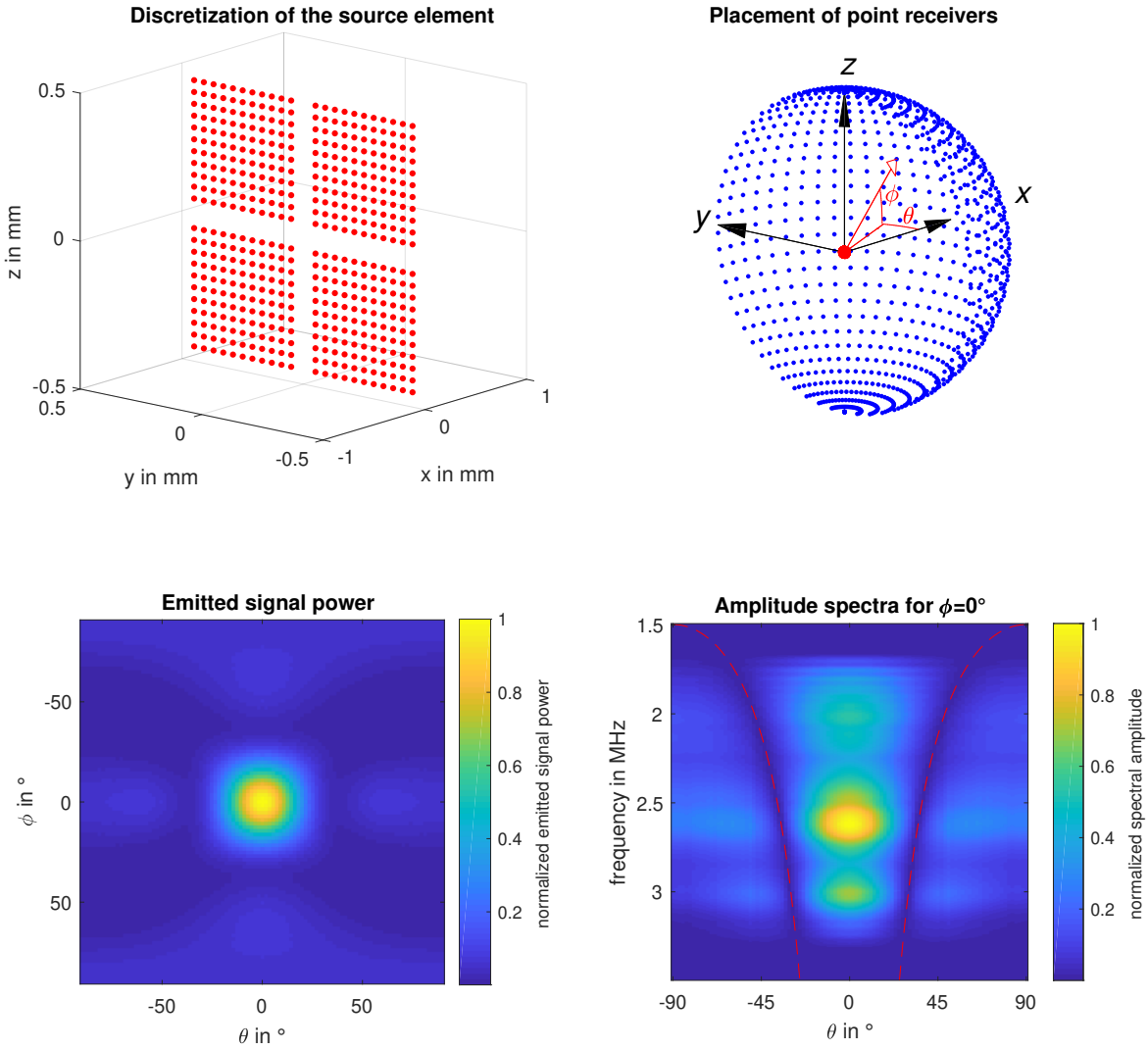

Figure 5.9: Simulation of the radiation pattern of a source element of the KIT 3D USCT II. In the upper left image, the placement of point sources on the four subelements of a source element is shown. In the upper right image, the placement of point receivers and the definition of the azimuth θ and the elevation angle ϕ are shown. In the lower left image, the emitted signal power normalized to the maximum at $\theta = 0°$ and $\phi = 0°$ is shown as a function of the emission angles. In the lower right image, the amplitude spectra of emitted signals for $\phi = 0°$ are shown as a function of θ. The spectral amplitude is normalized to its global maximum. The red dashed lines approximate the first-order diffraction minima caused by destructive interference.

In the second step of the analysis, I examine how accurate the transducer characteristics can be simulated with the presented approach. Therefore, I compare simulated data considering extended and individual point-approximated sources and receivers with the measured reference data. This is exemplarily performed for the two-dimensional acquisition geometry shown in figure 5.3.
For the simulation of the extended transducer elements, both source and receiver elements are discretized as shown in the upper left image of figure 5.9. Furthermore, their exact position and orientation as well as the inverted source signal of the simulated source element are considered. The water is parameterized with $c = 1498\,\mathrm{m\,s^{-1}}$ which corresponds to the speed of sound of water according to Marczak (1997) in consideration of the measured mean temperature. Speed of sound variations caused by inhomogeneity of the temperature field in the water bath are neglected.
In figure 5.10 the measured and simulated data observed at certain receiver elements are shown. In figure 5.11 the corresponding amplitude spectra observed at one receiver element of each available TAS are shown. The position of the receivers is specified by the angle $\theta = \theta_s - 180°$ with the source-receiver distance θ_s (counted counter-clockwise) so that the receiver element located opposite to the source corresponds to $\theta = 0°$. The results clearly demonstrate that the point approximation is not suitable for simulating the transducers except for $\theta = 0°$. The simulation considering extended source and receiver elements explains the measured data much better than the point approximation. The simulated amplitude spectra qualitatively agree with the measurement fairly well. Nevertheless, the achieved accuracy would not be sufficient for FWI as the simulated and measured waveforms differ too much, especially at large θ.
The causes of these differences are unknown but discrepancies between the true and numerical model due to temperature fluctuations (see section 5.1.1), inaccuracies related to edge effects (see lower left image of figure 5.3), uneven characteristics of the subelements (e.g. different delays regarding the excitation of the source signal) and the embedment of the TAS in the aperture (see upper right image of figure 5.1) are worth considering. The latter could probably have a shielding effect which could explain the absence of a measured wave at $\theta = 150°$.

To be able to successfully apply FWI on a dataset acquired with the KIT 3D USCT II, the transducer characteristics have to be considered. The presented first attempts to simulate these characteristics directly in the forward modeling indicate that this is quite challenging because only considering the spatial extent of the source and receiver elements is not sufficient.
In the following I propose an alternative approach which is able to consider even unknown effects which affect the radiation pattern of sources and the receiver characteristics. Furthermore, it allows to use the point approximation for sources and receivers in wave modeling.
I propose to calculate an individual Wiener filter for each source-receiver combination which transforms the measured reference data to the simulated data considering a homogeneous water model, point sources and receivers and the source signal estimation shown in figure 5.4.

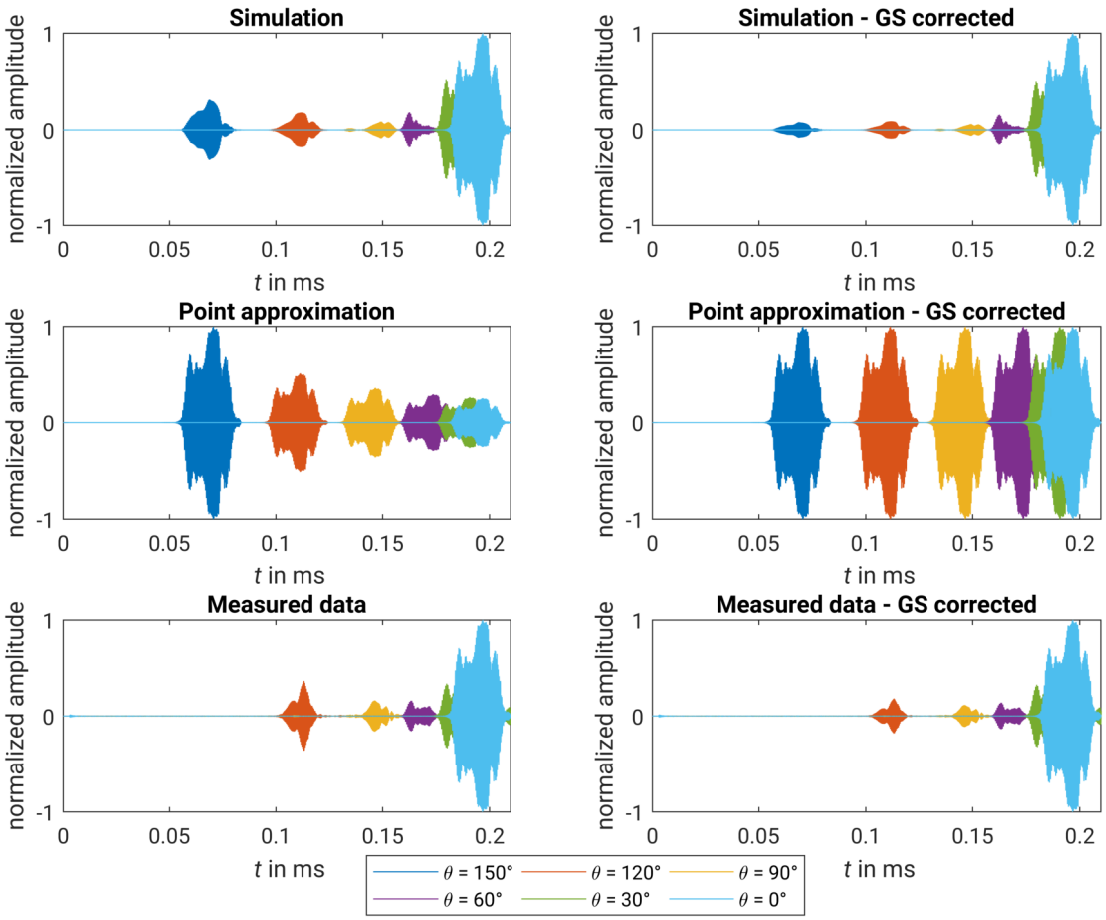

Figure 5.10: Simulated and measured A-scans of the reference measurement related to the two-dimensional acquisition geometry shown in figure 5.3. The position of the receivers is specified by the angle $\theta = \theta_s - 180°$ with the source-receiver distance θ_s (counted counter-clockwise) so that the receiver element located opposite to the source corresponds to $\theta = 0°$. In the upper row, the simulated data for extended source and receiver elements are shown. In the middle row, the simulated data for individual point sources and receivers are shown. In the lower row, the measured reference data are shown. In the left column, the raw observed data are shown. In the right column, the observed data were corrected with respect to geometrical spreading losses. The amplitudes are normalized to the maximum amplitude occurring in each individual plot.

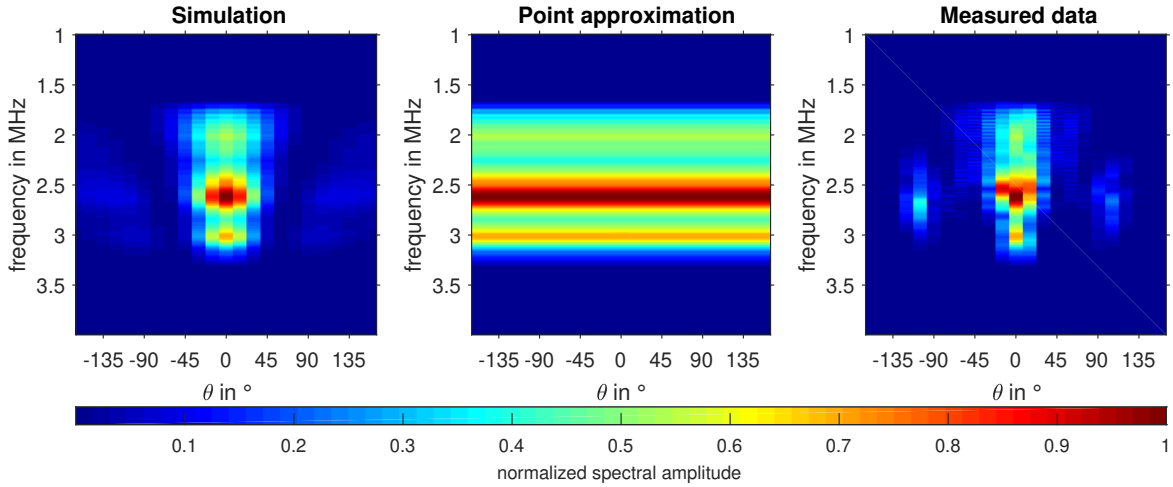

Figure 5.11: Amplitude spectra of simulated and measured A-scans of the reference measurement related to the two-dimensional acquisition geometry shown in figure 5.3. The position of the receivers is specified by the angle $\theta = \theta_s - 180°$ with the source-receiver distance θ_s (counted counter-clockwise) so that the receiver element located opposite to the source corresponds to $\theta = 0°$. The presented spectral amplitudes are normalized with respect to the maximum of each plot.

The obtained Wiener filters could then be applied on the measured data, which modifies them as they were excited and recorded by sources and receivers as specified in the forward modeling used for the generation of the filter. However, these Wiener filters are only valid for the direct wave and approximately for the transmitted wave as its path of propagation is very similar to that of the direct wave in a homogeneous model due to the relatively small variations of speed of sound within the breast. Consequently, other phases would have to be removed, e.g. by tapering the measured and simulated data to remove signals based on their traveltimes. However, this is supposed to be complicated, e.g. for the critically refracted wave which has for certain offsets very similar traveltimes compared to the refracted wave.
Due to the consideration of only one A-scan for calculating the Wiener filter pertaining to a certain source-receiver pair, measures must be taken to avoid that noise in the measured data distorts the results. This could be done by tapering the noise before and after the direct wave arrives. Due to the well-known model in the reference measurement, the required arrival times could even be estimated analytically. However, noise on top of the direct wave signal could not be removed with this procedure and, thus, a high signal-to-noise ratio is crucial for the success of this approach anyway.
In principle, it would also be possible to apply the inverse filter on the simulated data but this would lead to much larger computational cost as the filter operation would need to be applied after each forward simulation while the application of the filter on the measured data only needs to be performed once in the preprocessing. The calculation of the Wiener filters requires one forward simulation per source just like the source time function inversion but if they are applied, the source time function inversion does not need to be performed anymore.

It should be pointed out that the presented approach is in its initial stage. Many tests are necessary, for instance to examine if the Wiener filter is actually able to correctly transform the transmitted wave.

5.3.6 Robustness of the misfit convergence

The convergence of the misfit function is problematic as there exists a high risk of cycle-skipping due to the high complexity of the wavefield caused by a lack of low frequencies, the large number of propagated wavelengths, the usage of a sweep signal, three-dimensional scattering effects and suboptimal initial models. Furthermore, the previously presented challenges, e.g. the movements of the breast during data acquisition and the transducer characteristics, negatively affect the convergence. Even when these circumstances are considered, they hamper the stability because it is always necessary to make certain assumptions to be able to handle the related phenomena.

I definitely recommend to use the multiscale approach described in section 3.3 in order to increase the stability of the inversion. For the sake of completeness, it should be mentioned that there exist further strategies to increase the robustness of FWI, e.g. the adaptive waveform inversion proposed by Warner and Guasch (2016) and the combination of wave-equation reflection traveltime inversion with dynamic warping and full-waveform inversion proposed by Ma and Hale (2013). However, these methods go beyond the scope of this work.

An accurate initial model is a crucial factor regarding the convergence. The KIT-IPE provides three-dimensional reconstructions of the speed of sound obtained with a bent-ray tomography algorithm according to Dapp (2013) and the reflectivity obtained with a synthetic aperture focusing technique (SAFT) algorithm according to Kretzek and Ruiter (2014). The results are shown on figure 5.12. The speed of sound reconstruction is not suitable as an initial model in FWI because speed of sound values significantly lower than $1450\,\mathrm{m\,s^{-1}}$ and the pattern of the broad disjointed high-velocity zones which probably correspond to the skin indicate the existence of artifacts which would let the misfit fall into a local minimum very early on. The reflectivity reconstruction has a significantly higher resolution and could probably be used to extract the outer shape of the breast which, in turn, could be used for the creation of two-phased initial models of the speed of sound and quality factor distinguishing between water and breast tissue. The water could be parameterized according to the temperature measurements and the breast could be parameterized with mean values of breast tissue. The quality factor could simply be estimated by the ratio of the amplitudes of the direct wave in the reference measurement and the corresponding damped refracted wave in the measurement with immersed breast, e.g. as proposed by Sandhu (2015). The initial density model could be obtained by scaling the speed of sound model according to section 3.3.4. However, such two-phased models are probably not sufficient if no low frequencies are available.

Hence, more sophisticated methods are necessary for the generation of accurate speed of sound and quality factor models, e.g. an iterative bent-ray traveltime tomography algorithm as proposed by Li et al. (2009). On the one hand, such methods have relatively high computational requirements. On the other hand, the more accurate the initial model, the fewer FWI iterations are needed. In consideration of the estimated high computational cost of one three-dimensional forward modeling presented in section 5.3.3, spending much computational effort in the generation of initial models as accurate as possible is actually supposed to be worthwile regarding the total computational cost.

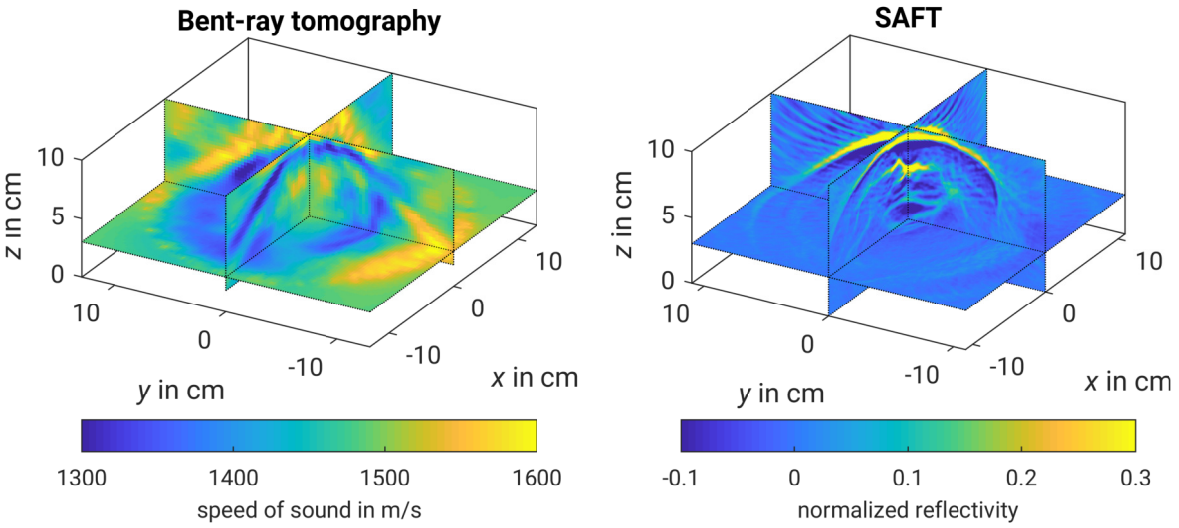

Figure 5.12: Results of a three-dimensional bent-ray tomography according to Dapp (2013) and synthetic aperture focusing technique (SAFT) reconstruction according to Kretzek and Ruiter (2014) which were kindly provided by the KIT-IPE. The reflectivity reconstructed with SAFT is normalized to its maximum. For the sake of better visualization, the z-axis is reversed, borders and intersections of the slices are highlighted with dotted lines and the shown speed of sound values and the normalized reflectivity are clipped.

When sweep signals are used in seismics, the measured data are usually crosscorrelated with the pilot source signal according to the convolutional model of the Earth. Under the assumption of stationary wave propagation, i.e. the shape of the waveform does not change with traveltime, this allows to replace the complex superposition of sweep signals with a series of much narrower signals, viz. the autocorrelation of the source signal, in order to increase the distinguishability of different phases and, thus, decrease the complexity of the data. If the measured data are preprocessed like that, the actual source signal must be replaced by its autocorrelation in the forward simulations of FWI (Yilmaz, 2001).
The direct application of this strategy on the observed data is not suitable due to the transducer characteristics discussed in section 5.3.5 according to which the emitted and received waveforms strongly depend on the emission and incidence angle, respectively.

Accordingly, the source signal does not appear in its original shape in the measured data which are, however, assumed to be a superposition of multiple differently scaled and delayed source wavelets in the scope of this approach. Consequently, the cross-correlation does not yield a series of distinct narrow signals. In principle, it should be possible to perform the crosscorrelation after applying the Wiener filters described in section 5.3.5 which transform the measured data as they were acquired with point sources and receivers. However, this would need to be tested rigorously. Even if this procedure were successful, non-stationarity of the waveforms, mainly caused by the anelastic attenuation within the breast, would still distort the results. Although there also exist methods to deal with this problem, e.g. inverse Q filtering (Yilmaz, 2001), I would not recommend this strategy as it is doubtful whether FWI could be applied successfully on such highly altered data due to the implicit approximations made in each processing step. Instead, I would suggest to directly use an impulse source for data acquisition even though it would emit less energy and, thus, lower the signal-to-noise ratio.

5.3.7 Spatial aliasing

In the KIT 3D USCT II 1413 receiver elements clustered at 157 TAS are implemented. According to Ruiter et al. (2018a) and Simonetti and Huang (2009),

$$N_{\mathrm{numRec3D}} \geq \left(\frac{2\,\pi\,r_{\mathrm{ROI}}}{\lambda}\right)^2 \tag{5.2}$$

receivers equiangularly distributed over a semisphere would be required in order to prevent spatial aliasing based on the Nyquist–Shannon sampling theorem. Considering a radius of the region of interest $r_{\mathrm{ROI}} = 6\,\mathrm{cm}$ which corresponds to a typical spatial extent of a breast and the wavelength $\lambda = c\,/\,f = 0.6\,\mathrm{mm}$ related to the center frequency of the sources $f_{\mathrm{c}} = 2.5\,\mathrm{MHz}$ and the speed of sound $c = 1500\,\mathrm{m\,s^{-1}}$, approximately 400 000 receivers would be required. This means, as it stands the sampling criterion is not even nearly fulfilled which yields strong grating lobe artifacts in the obtained gradients.

In the following, the impact of the resulting grating lobe artifacts is investigated. For the sake of simplicity, this is performed for the two-dimensional acquisition geometry shown in figure 5.3. According to Simonetti et al. (2007),

$$N_{\mathrm{numRec2D}} \geq \frac{4\,\pi\,r_{\mathrm{ROI}}}{\lambda} \tag{5.3}$$

equiangularly distributed receivers are required to fulfill the sampling criterion for a circular aperture. Considering the same parameters as above, 1256 receivers would be necessary to prevent spatial aliasing. Actually, 72 receivers clustered at 24 TAS are implemented without taking the defective receivers into account. The ratio of the number of implemented and required receivers is one order higher for the two-dimensional acquisition geometry and thus the impact of grating lobe artifacts in the

three-dimensional case is expected to be even larger.
In figure 5.13 the gradient with respect to the speed of sound obtained at the first iteration of acoustic FWI applied on the reference data is shown. As the FWI is only performed for illustration of occurring grating lobe artifacts in the gradient, a very poor FWI workflow is applied that neither uses a gradient taper to prevent the generation of artifacts in the vicinity of sources and receivers nor considers any transducer characteristics and adapts the measured data to the two-dimensional experiment with the direct wave transformation proposed by Forbriger et al. (2014) which is only valid for point sources. A homogeneous model parameterized with a speed of sound of $1498\,\mathrm{m\,s^{-1}}$ and a density of $998\,\mathrm{kg\,m^{-3}}$ according to the measured mean temperature is used as the initial model. Hence, an irregular pattern would be expected in the gradient in order to reconstruct speed of sound variations caused by temperature fluctuations. However, a radially symmetric pattern dominates the gradient which is associated with the presence of grating lobes in the response function of the receiver array due to spatial undersampling (Simonetti et al., 2007). Further synthetic tests not presented here, in which gradients obtained with different numbers of receivers were compared, confirm that these artifact are not caused by the neglect of the transducer characteristics but by the small number of receivers.

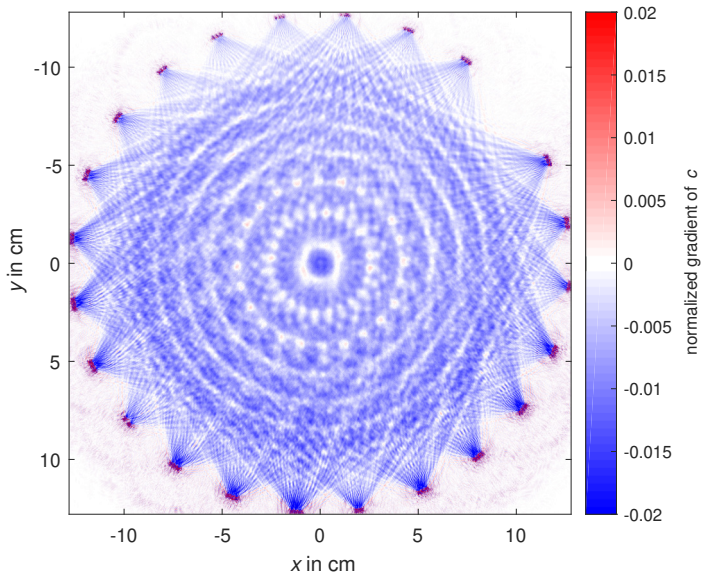

Figure 5.13: Gradient with respect to the speed of sound obtained at the first iteration of FWI applied on the reference data acquired with the two-dimensional acquisiton geometry shown in figure 5.3. The gradient is normalized to its maximum. Due to very strong artifacts in the vicinity of sources and receivers, the shown values are clipped. The radially symmetric artifacts, called grating lobe artifacts, are caused by spatial aliasing.

Antialiasing filters which are applied in the wavenumber domain can be used to remove artifacts caused by spatial undersampling. However, they yield a loss of information and drastically reduce the achievable resolution if the sampling criterion is violated as

much as it is the case for the KIT 3D USCT II. There exist further strategies, e.g. the introduction of virtual receivers at which a pseudo-measurement via interpolation of the recorded data is performed (Shi and Huthwaite, 2018), but their effectiveness is restricted. Thus, it would be inevitable to implement more transducers in order to make a successful application of FWI possible. However, it is hardly possible to implement 400 000 receivers due to technical limitations and the huge amount of data that would be acquired. From my point of view, the best way to deal with this problem would combine the implementation of more receivers and the usage of lower frequencies as the number of required receivers to fulfill the sampling criterion 5.2 is proportional to the squared frequency.

5.3.8 Assessment of the feasibility

In this section I assess the feasibility of applying three-dimensional FWI on a dataset acquired with the KIT 3D USCT II based on the analysis of the challenges presented in the prior sections.
While it is possible to deal with most of the difficulties, the lack of a sufficient number of receivers and the resulting grating lobe artifacts occurring in the obtained gradients make a successful application of FWI with the current prototype of the KIT 3D USCT impossible. In principle, it would be possible reduce the grating lobe artifacts by applying antialiasing filters but due to the small number of receivers they would reduce the achievable resolution so drastically that applying FWI would not be worth the required huge computational effort. In order to change this, many more receivers need to be implemented and lower frequencies should be used as this would significantly reduce the number of required receivers. The latter would also have a positive impact on two further limiting factors as it would increase the robustness of the inversion while reducing the extremely high computational requirements. Furthermore, the usage of lower frequencies would reduce the transducer characteristics which are primarily determined by the ratio between the transducer size and the emitted or recorded wavelength.
Moreover, accurate measurements or reconstructions of the position of the breast at each shot are necessary to be able to consider the movements during data acquisition. Defective transducers have to be detected to ignore related signals during the inversion and all phases except the direct and refracted wave have to be removed to allow the application of Wiener filters which could be used to consider the exact source signal and the transducer characteristics. However, this approach which is presented in section 5.3.5 is in its initial stage and requires further development and must be tested in order to examine its validity. Due to the high risk of cycle skipping and the large computational cost of three-dimensional viscoacoustic forward modelings, I recommend to generate initial models as accurate as possible in order to reduce the risk of cycle skipping and the number of necessary iterations. Last but not least, the usage of an impulse source instead of a sweep signal would make the data easier to analyze and avoid the necessity to apply further preprocessing on the data.

Chapter 6

Conclusions & Outlook

In this work, I performed reconstruction tests for an anatomically realistic numerical breast model using two-dimensional time-domain viscoacoustic full-waveform inversion (FWI) under optimal conditions. Sources with a center frequency of 0.5 MHz were used and clearly demonstrated the benefits related to the availability of such low frequencies as the inversion was stable enough to converge without any a priori information but still provided a sufficiently high resolution. This holds in particular for the speed of sound reconstructions in which even small details, e.g. the irregular margin of the tumor phantoms, could be resolved, even by performing acoustic FWI which neglects the velocity dispersion caused by the anelastic attenuation.
The accurate reconstruction of the attenuation was much more challenging. Various tests demonstrated that considering a linear relationship between the speed of sound and density instead of inverting the density is able to drastically increase the quality of attenuation reconstructions. Despite the introduction of artifacts that could not completely be prevented, different tissues can be identified and the mean values of the inverted attenuation within fat, fibroglandular tissue and the tumors could be reconstructed accurately. However, only poor results could be obtained for small-scale structures such as the blood vessels and skin. Furthermore, crosstalk tests demonstrated that the spatial correlation of all parameters is a crucial factor for the successful inversion of the attenuation. This is, however, supposed to be a reasonable assumption as all parameters are determined by the distribution of different breast tissues.

A feasibility study for the application of three-dimensional FWI on data acquired with the KIT 3D USCT II was performed in chapter 5. According to this study, datasets acquired with the current prototype of the data acquisition system are unsuitable for the application of three-dimensional FWI as there are not enough receivers, which leads to the occurrence of grating lobe artifacts in the gradients. In principle, there exist strategies to deal with spatial undersampling but their effectiveness is limited and they yield a significant loss of resolution. Since the achievable resolution with respect to the number of implemented receivers would thus be very low, I conclude that the application of three-dimensional FWI is not worth the required extremely high computational effort.

Furthermore, the main challenges related to the evaluation of measured data were addressed and analyzed. Simulations of the transducers demonstrated that diffraction effects yield a strong dependence of the signals excited by the sources and the waveforms recorded at the receivers on the emission and incidence angle, respectively, due to the comparable size of ultrasound transducers and the occurring wavelengths. Hence, the point approximation which is usually considered for sources and receivers in seismic wave modeling, is not suitable. The application of Wiener filters on the measured data, which modify them as if they were excited and recorded by point sources and receivers, were proposed as a potential strategy to consider the transducer characteristics in the scope of FWI.
Movements of the breast during the data acquisition in the order of multiple wavelengths have to be considered in order to prevent blurrings and artifacts in the model reconstructions. Therefore, it is necessary to know the exact position of the breast for each shot. Moreover, an accurate initial model is required to permit the convergence of the misfit since the high complexity of the wavefields caused by the large number of propagated wavelengths related to the usage of high frequencies, three-dimensional scattering effects and the usage of a sweep signal leads to a high risk of cycle skipping. Based on the results from the synthetic tests and the feasibility study, I recommend to apply three-dimensional FWI on data with a lower frequency content because of the related increased stability, weakening of the transducer characteristics and a significant reduction of the number of required receivers or rather the impact of spatial aliasing.

Due to time constraints, many aspects which were mentioned in this work could not be investigated in sufficient detail and, thus, require further studies.
The proposed discretization criterion needs to be tested systematically in order to examine its scope of validity, e.g. with respect to heterogeneous media and viscoacoustic and elastic wave simulations. Moreover, its application could be automated in order to find the optimal discretization which minimizes the product of the number of spatial grid points and timesteps and, consequently, the computational requirements while satisfying the proposed criterion. Furthermore, the seismic quality factors of different breast tissues were assumed to be constant in the forward simulations which does not match their real behavior. The effects of this approximation need to be examined. The proposed strategies to deal with the challenges related to the application of FWI on measured data, e.g. the application of Wiener filters in order to consider the transducer characteristics, are in their initial stages and have to be tested rigorously. Since three-dimensional acquisition systems require a huge number of receivers in order to fulfill the spatial sampling criterion but technical restrictions limit the number of transducers that might be implemented, extensive studies on potential approaches to reduce the effects of spatial undersampling are necessary. Moreover, FWI has to be optimized with respect to its computational requirements in order to make it clinically applicable.

All in all, I see great potential for medical ultrasound imaging using FWI as it was demonstrated to be able to significantly exceed the resolution limit of standard ray-based methods. As computational power continues to rapidly increase with a simulta-

neous decrease in cost and much research is underway to accelerate FWI algorithms, e.g. by source encoding and the development of efficient parallel implementations on graphical processing units, FWI is expected to become increasingly important for clinical applications in the future.

Bibliography

Agudo, O. C., Guasch, L., Huthwaite, P., and Warner, M. (2018). 3D imaging of the breast using full-waveform inversion. In Hopp, T., Ruiter, N., Bamber, J. C., Duric, N., and van Dongen, K. W., editors, *Proceedings of the International Workshop on Medical Ultrasound Tomography: 1.-3. Nov. 2017, Speyer, Germany*. KIT Scientific Publishing, Karlsruhe.

Aiello, E. J., Buist, D. S. M., White, E., Seger, D., and Taplin, S. H. (2004). Rate of Breast Cancer Diagnoses among Postmenopausal Women with Self-Reported Breast Symptoms. *The Journal of the American Board of Family Practice*, 17(6):408–415.

Aki, K. and Richards, P. G. (2002). *Quantitative Seismology*. University Science Books, 2nd edition.

Assis, C. A. M., Oliveira, S. A. M., Misságia, R. M., and de Ceia, M. A. R. (2017). Source wavelet and local wave propagation effects on the amplitude-variation-with-offset response of thin-layer models: A physical modeling study. *GEOPHYSICS*, 82(4):27–41.

Blanch, J. O., Robertsson, J. O. A., and Symes, W. W. (1995). Modeling of a constant Q: Methodology and algorithm for an efficient and optimally inexpensive viscoelastic technique. *GEOPHYSICS*, 60(1):176–184.

Blitz, J. and Simpson, G. (1995). *Ultrasonic Methods of Non-destructive Testing*. Non-Destructive Evaluation Series. Springer Netherlands.

Bohlen, T. (1998). *Viskoelastische FD-Modellierung seismischer Wellen zur Interpretation gemessener Seismogramme*. PhD thesis, Kiel University.

Bohlen, T. (2002). Parallel 3-D Viscoelastic Finite Difference Seismic Modelling. *Comput. Geosci.*, 28(8):887–899.

Bohlen, T. and Pan, Y. (2018). Seismic Modelling. Lecture notes. Karlsruhe Institute of Technology.

Bohlen, T. and Saenger, E. H. (2006). Accuracy of heterogeneous staggered-grid finite-difference modeling of Rayleigh waves. *GEOPHYSICS*, 71(4):109–115.

Borup, D. T., Johnson, S. A., Natterer, F., Olsen, S. C., Wiskin, J. W., Wubeling, F., and Zhang, Y. (1999). Apparatus and method for imaging with wavefields using inverse scattering techniques. *US Patent US6005916A*.

Boyd, N. F., Guo, H., Martin, L. J., Sun, L., Stone, J., Fishell, E., Jong, R. A., Hislop, G., Chiarelli, A., Minkin, S., and Yaffe, M. J. (2007). Mammographic density and the risk and detection of breast cancer. *New England Journal of Medicine*, 356(3):227–236.

Buddensiek, M. L., Krawczyk, C. M., Kukowski, N., and Oncken, O. (2009). Performance of piezoelectric transducers in terms of amplitude and waveform. *GEOPHYSICS*, 74(2):T33–T45.

Bunks, C., Saleck, F. M., Zaleski, S., and Chavent, G. (1995). Multiscale seismic waveform inversion. *GEOPHYSICS*, 60(5):1457–1473.

Carcione, J. M., Kosloff, D., and Kosloff, R. (1988). Wave propagation simulation in a linear viscoelastic medium. *Geophysical Journal*, 95(3):597–611.

Casarotto, R. A., Adamowski, J. C., Fallopa, F., and Bacanelli, F. (2004). Coupling agents in therapeutic ultrasound: acoustic and thermal behavior. *Archives of Physical Medicine and Rehabilitation*, 85(1):162–165.

Chen, T. H.-H., Yen, A. M.-F., Fann, J. C.-Y., Gordon, P., Chen, S. L.-S., Chiu, S. Y.-H., Hsu, C.-Y., Chang, K.-J., Lee, W.-C., Yeoh, K. G., Saito, H., Promthet, S., Hamashima, C., Maidin, A., Robinson, F., and Zhao, L.-Z. (2017). Clarifying the debate on population-based screening for breast cancer with mammography: A systematic review of randomized controlled trials on mammography with Bayesian meta-analysis and causal model. *Medicine*, 96(3).

Christensen, R. (1982). *Theory of Viscoelasticity: An Introduction*. Elsevier Science, 2nd edition.

Cooper, G. (1992). *Elements of Human Cancer*. Biology Series. Jones and Bartlett Publishers.

Courant, R., Friedrichs, K., and Lewy, H. (1928). Über die partiellen Differenzengleichungen der mathematischen Physik. *Mathematische Annalen*, 100:32–74.

Dapp, R. (2013). *Abbildungsmethoden für die Brust mit einem 3D-Ultraschall-Computertomographen*. PhD thesis, Karlsruhe Institute of Technology.

D'Astous, F. T. and Foster, F. S. (1986). Frequency dependence of ultrasound attenuation and backscatter in breast tissue. *Ultrasound in Medicine and Biology*, 12(10):795–808.

Delphinus Medical Technologies (2018). Discover SoftVue. website. `http://delphinusmt.com/` (accessed August 23, 2018).

Dempsey, P. J. (2004). The History of Breast Ultrasound. *Journal of Ultrasound in Medicine*, 23(7):887–894.

Donald, I., Macvicar, J., and Brown, T. (1958). Investigation of abdominal masses by pulsed ultrasound. *The Lancet*, 271(7032):1188–1195. Originally published as Volume 1, Issue 7032.

D'Orsi, C. and Acr (2013). *ACR BI-RADS Atlas: Breast Imaging Reporting and Data System*. American College of Radiology.

Duric, N., Littrup, P., Li, C., Roy, O., Schmidt, S., Cheng, X., Seamans, J., Wallen, A., and Bey-Knight, L. (2014). Breast imaging with SoftVue: initial clinical evaluation. *Proceedings of SPIE - the International Society for Optical Engineering*, 9040.

Duric, N., Littrup, P., Poulo, L., Babkin, A., Pevzner, R., Holsapple, E., Rama, O., and Glide, C. (2007). Detection of breast cancer with ultrasound tomography: First results with the Computed Ultrasound Risk Evaluation (CURE) prototype. *Medical Physics*, 34(2):773–785.

Duric, N., Littrup, P. J., Li, C., Sak, M., Sandhu, Y., Bergman, K., Boone, M., and Chen, D. (2018). Ultrasound Tomography for Breast Cancer Screening. In Hopp, T., Ruiter, N., Bamber, J. C., Duric, N., and van Dongen, K. W., editors, *Proceedings of the International Workshop on Medical Ultrasound Tomography: 1.-3. Nov. 2017, Speyer, Germany*. KIT Scientific Publishing, Karlsruhe.

Ervik, M., Lam, F., Ferlay, J., Mery, L., Soerjomataram, I., and Bray, F. (2016). Cancer Today: International Agency for Research on Cancer, World Health Organization. website. `http://gco.iarc.fr/today` (accessed August 17, 2018).

Fichtner, A. (2010). *Full Seismic Waveform Modelling and Inversion*. Advances in Geophysical and Environmental Mechanics and Mathematics. Springer Berlin Heidelberg.

Forbriger, T. and Friederich, W. (2005). A proposal for a consistent parametrization of earth models. *Geophysical Journal International*, 162(2):425–430.

Forbriger, T., Groos, L., and Schäfer, M. (2014). Line-source simulation for shallow-seismic data. Part 1: theoretical background. *Geophysical Journal International*, 198(3):1387–1404.

Fry, E. K., Kossoff, G., and Hindman, H. A. (1972). The Potential of Ultrasound Visualization for Detecting the Presence of Abnormal Structures Within the Female Breast. In *Proceedings of the IEEE Ultrasonic Symposium: New York 1972*, pages 25–30.

Garcia, J. P. J., Garcia, P. M., and Rosen, R. B. (2005). Wide-field handheld high frequency ultrasonography using a variable high frequency ultrasound system. *Ophthalmic Surgery, Lasers & Imaging*, 36(2):139–141.

Greenleaf, J. F. (2018). Ultrasound Computed Tomography: Historically Guided Musings. In Hopp, T., Ruiter, N., Bamber, J. C., Duric, N., and van Dongen, K. W., editors, *Proceedings of the International Workshop on Medical Ultrasound Tomography: 1.- 3. Nov. 2017, Speyer, Germany*. KIT Scientific Publishing, Karlsruhe.

Greenleaf, J. F. and Bahn, R. C. (1981). Clinical imaging with transmissive ultrasonic computerized tomography. *IEEE Trans Biomed Eng*, 28(2):177–185.

Greenleaf, J. F., Johnson, S. A., Lee, S. L., Hermant, G. T., and Woo, E. H. (1974). *Algebraic Reconstruction of Spatial Distributions of Acoustic Absorption within Tissue from Their Two-Dimensional Acoustic Projections*, pages 591–603. Springer US, Boston, MA.

Heijnsdijk, L., Jansen, E., Taskin, U., den Bok, H., Bergsma, E., Noothout, E., de Jong, N., and van Dongen, K. W. (2018). First steps towards the Delft Breast Ultrasound Scanning System (DBUS). In Hopp, T., Ruiter, N., Bamber, J. C., Duric, N., and van Dongen, K. W., editors, *Proceedings of the International Workshop on Medical Ultrasound Tomography: 1.-3. Nov. 2017, Speyer, Germany*. KIT Scientific Publishing, Karlsruhe.

Hopp, T., Cotic Smole, P., and Ruiter, N. (2018). Comparison of registration strategies for USCT–MRI image fusion: preliminary results. In Hopp, T., Ruiter, N., Bamber, J. C., Duric, N., and van Dongen, K. W., editors, *Proceedings of the International Workshop on Medical Ultrasound Tomography: 1.-3. Nov. 2017, Speyer, Germany*. KIT Scientific Publishing, Karlsruhe.

Jellins, J., Kossoff, G., Reeve, T., and Barraclough, B. (1971). Ultrasonic visualization of the breast. *Med. J. Aust.*, 1(6):305–307.

Jellins, J., Kossoff, G., Reeve, T., and Barraclough, B. (1975). Ultrasonic grey scale visualization of breast disease. *Ultrasound in Medicine & Biology*, 1(4):393–404.

Jensen, J. A., Kortbek, J., Nikolov, S. I., Hemmsen, M., and Tomov, B. (2010). Implementation of Synthetic Aperture Imaging in Medical Ultrasound: The Dual Stage Beamformer Approach. In *8th European Conference on Synthetic Aperture Radar*, pages 1–4.

Karmakar, M. K. and Kwok, W. H. (2016). Anesthesia Key – Ultrasound-Guided Regional Anesthesia. website. `https://aneskey.com/ultrasound-guided-regional-anesthesia/` (accessed August 10, 2018).

Keijzer, L., Lagendijk, M., Stigter, N., van Deurzen, C. H. M., Verhoef, C., van Lankeren, W., Koppert, L. B., and van Dongen, K. W. (2018). Measurement of the speed of sound, attenuation and mass density of fresh breast tissue. In Hopp, T., Ruiter, N., Bamber, J. C., Duric, N., and van Dongen, K. W., editors, *Proceedings of the International Workshop on Medical Ultrasound Tomography: 1.-3. Nov. 2017, Speyer, Germany*. KIT Scientific Publishing, Karlsruhe.

Kell, G. S. (1975). Density, Thermal Expansivity, and Compressibility of Liquid Water from 0° to 150 °C: Correlations and Tables for Atmospheric Pressure and Saturation Reviewed and Expressed on 1968 Temperature Scale. *Journal of Chemical & Engineering Data*, 20(1):97–105.

Köhn, D. (2015). *Time domain 2D elastic full waveform tomography*. PhD thesis, Kiel University.

Komatitsch, D. and Martin, R. (2007). An unsplit convolutional perfectly matched layer improved at grazing incidence for the seismic wave equation. *GEOPHYSICS*, 72(5):155–167.

Krebs, J. R., Anderson, J. E., Hinkley, D., Neelamani, R., Lee, S., Baumstein, A., and Lacasse, M.-D. (2009). Fast full-wavefield seismic inversion using encoded sources. *GEOPHYSICS*, 74(6):177–188.

Kretzek, E. and Ruiter, N. V. (2014). GPU based 3D SAFT reconstruction including phase aberration. In *SPIE Medical Imaging Conference 2014, San Diego, California, 15-20 February 2014*.

Kurzmann, A. (2012). *Applications of 2D and 3D full waveform tomography in acoustic and viscoacoustic complex media*. PhD thesis, Karlsruhe Institute of Technology.

Kurzmann, A., Shigapov, R., and Bohlen, T. (2015). Viscoacoustic Full Waveform Inversion for Spatially Correlated and Uncorrelated Problems in Reflection Seismics. In *77th EAGE Conference and Exhibition, Expanded Abstracts*.

Ladyzhenskaya, O. A. (1985). *The Method of Finite Differences*, pages 212–307. Springer New York.

Lailly, P. (1983). The seismic inverse problem as a sequence of before stack migrations. In Bednar, J. B., Redner, R., Robinson, E., and Weglein, A., editors, *Conference on Inverse Scattering: Theory and Application*, pages 206–220. SIAM Philadelphia.

Levander, A. R. (1988). Fourth-order finite-difference P-SV seismograms. *GEOPHYSICS*, 53(11):1425–1436.

Li, C., Duric, N., Littrup, P., and Huang, L. (2009). In vivo Breast Sound-Speed Imaging with Ultrasound Tomography. *Ultrasound in Medicine & Biology*, 35(10):1615–1628.

Li, C., Sandhu, G. S., Roy, O., Duric, N., Allada, V., and Schmidt, S. (2014). Toward a practical ultrasound waveform tomography algorithm for improving breast imaging. *Proceedings of SPIE - the International Society for Optical Engineering*, 9040.

Littrup, P. J., Duric, N., Li, C., Sak, M., Sandhu, G., Bergman, K., Boone, M., and Chen, D. (2018). Current challenges in Breast Screening and Diagnosis: From Molecules to Peritumoral Regions and Radiomics – The Emerging Imaging of Whole Breast Stiffness. In Hopp, T., Ruiter, N., Bamber, J. C., Duric, N., and van Dongen, K. W., editors, *Proceedings of the International Workshop on Medical Ultrasound Tomography: 1.-3. Nov. 2017, Speyer, Germany*. KIT Scientific Publishing, Karlsruhe.

Liu, H.-P., Anderson, D. L., and Kanamori, H. (1976). Velocity dispersion due to anelasticity; implications for seismology and mantle composition. *Geophysical Journal*, 47:41–58.

Liu, Y. and Sen, M. K. (2009). An implicit staggered-grid finite-difference method for seismic modelling. *Geophysical Journal International*, 179(1):459–474.

Liu, Y. and Sen, M. K. (2011). Scalar Wave Equation Modeling with Time-Space Domain Dispersion-Relation-Based Staggered-Grid Finite-Difference Schemes. *The Bulletin of the Seismological Society of America*, 101:141–159.

Lou, Y., Zhou, W., Matthews, T. P., Appleton, C. M., and Anastasio, M. A. (2017). Generation of anatomically realistic numerical phantoms for photoacoustic and ultrasonic breast imaging. *Journal of Biomedical Optics*, 22(4).

Ma, Y. and Hale, D. (2013). Wave-equation reflection traveltime inversion with dynamic warping and full-waveform inversion. *GEOPHYSICS*, 78(6):223–233.

Madjar, H. (2018). Challenges in Breast Ultrasound. In Hopp, T., Ruiter, N., Bamber, J. C., Duric, N., and van Dongen, K. W., editors, *Proceedings of the International Workshop on Medical Ultrasound Tomography: 1.-3. Nov. 2017, Speyer, Germany*. KIT Scientific Publishing, Karlsruhe.

Marczak, W. (1997). Water as a standard in the measurements of speed of sound in liquids. *The Journal of the Acoustical Society of America*, 102(5):2776–2779.

Mast, T. D. (2000). Empirical relationships between acoustic parameters in human soft tissues. *Acoustics Research Letters Online*, 1(2):37–42.

Meschede, D. (2015). *Gerthsen Physik*. Springer-Lehrbuch. Springer Heidelberg.

Miller, D., Smith, N., Bailey, M., Czarnota, G., Hynynen, K., and Makin, I. (2012). Overview of Therapeutic Ultrasound Applications and Safety Considerations. *J. Ultrasound Med.*, 31(4):623–634.

Müller, G. (2007). *Theory of Elastic Waves*. Scientific Technical Report 2007: GeoForschungsZentrum Potsdam.

Netter, F. (2017). *Atlas of Human Anatomy*. Netter Basic Science. Elsevier Health Sciences.

Nocedal, J. and Wright, S. J. (2006). *Numerical Optimization*. Springer, New York, 2nd edition.

Ozmen, N., Dapp, R., Zapf, M., Gemmeke, H., Ruiter, N. V., and van Dongen, K. W. A. (2015). Comparing different ultrasound imaging methods for breast cancer detection. *IEEE Transactions on Ultrasonics, Ferroelectrics, and Frequency Control*, 62(4):637–646.

Pica, A., Diet, J. P., and Tarantola, A. (1990). Nonlinear inversion of seismic reflection data in a laterally invariant medium. *GEOPHYSICS*, 55(3):284–292.

Plessix, R.-E. (2006). A review of the adjoint-state method for computing the gradient of a functional with geophysical applications. *Geophysical Journal International*, 167(2):495–503.

Polak, E. and Ribière, G. (1969). Note sur la convergence de méthodes de directions conjuguées. *R.I.R.O.*, 3(16):35–43.

Pratt, R. G. (1999). Seismic waveform inversion in the frequency domain, Part 1: Theory and verification in a physical scale model. *GEOPHYSICS*, 64(3):888–901.

Pratt, R. G. (2008). Waveform tomography – Successes, cautionary tales, and future directions. In *70th EAGE Conference & Exhibition, Expanded Abstracts*.

Pratt, R. G. (2018). Medical ultrasound tomography: lessons from exploration geophysics. In Hopp, T., Ruiter, N., Bamber, J. C., Duric, N., and van Dongen, K. W., editors, *Proceedings of the International Workshop on Medical Ultrasound Tomography: 1.-3. Nov. 2017, Speyer, Germany*. KIT Scientific Publishing, Karlsruhe.

Pratt, R. G., Huang, L., Duric, N., and Littrup, P. (2007). Sound-speed and attenuation imaging of breast tissue using waveform tomography of transmission ultrasound data. *Proc. SPIE*, 6510.

Pykett, I. L., Newhouse, J. H., Buonanno, F. S., Brady, T. J., Goldman, M. R., Kistler, J. P., and Pohost, G. M. (1982). Principles of nuclear magnetic resonance imaging. *Radiology*, 143(1):157–168.

Rienstra, S. W. and Hirschberg, A. (2004). *An Introduction to Acoustics*. Eindhoven University of Technology.

Robertsson, J. O. A., Blanch, J. O., and Symes, W. W. (1994). Viscoelastic finite-difference modeling. *GEOPHYSICS*, 59(9):1444–1456.

Roy, O., Jovanović, I., Hormati, A., Parhizkar, R., and Vetterli, M. (2010). Sound speed estimation using wave-based ultrasound tomography: theory and GPU implementation. *Proceedings of SPIE - the International Society for Optical Engineering*, 7629.

Ruiter, N., Hopp, T., Zapf, M., Kretzek, E., and Gemmeke, H. (2016). Analysis of patient movement during 3D USCT data acquisition. *Proceedings of SPIE - the International Society for Optical Engineering*, 9790.

Ruiter, N., Hopp, T., Zapf, M., Menshikov, A., Kaiser, C., and Gemmeke, H. (2018a). 3D Ultrasound Computer Tomography for Breast Cancer Diagnosis at KIT: an Overview. In Hopp, T., Ruiter, N., Bamber, J. C., Duric, N., and van Dongen, K. W., editors, *Proceedings of the International Workshop on Medical Ultrasound Tomography: 1.-3. Nov. 2017, Speyer, Germany*. KIT Scientific Publishing, Karlsruhe.

Ruiter, N., Zapf, M., Hopp, T., and van Dongen, K. (2018b). USCT data exchange and collaboration. website. `http://ipeusctdb1.ipe.kit.edu/~usct/challenge/?page_id=92` (accessed August 10, 2018).

Sak, M., Duric, N., Littrup, P., Bey-Knight, L., Ali, H., Vallieres, P., Sherman, M. E., and Gierach, G. L. (2017a). Using Speed of Sound Imaging to Characterize Breast Density. *Ultrasound in Medicine & Biology*, 43(1):91–103.

Sak, M., Duric, N., Littrup, P., Sherman, M., and Gierach, G. (2017b). Ultrasound tomography imaging with waveform sound speed: Parenchymal changes in women undergoing tamoxifen therapy. *Proceedings of SPIE - the International Society for Optical Engineering*, 10139.

Sandhu, G., Littrup, P. J., Sak, M., Li, C., and Duric, N. (2018). Tissue Characterization With Ultrasound Tomography Machine Learning. In Hopp, T., Ruiter, N., Bamber, J. C., Duric, N., and van Dongen, K. W., editors, *Proceedings of the International Workshop on Medical Ultrasound Tomography: 1.-3. Nov. 2017, Speyer, Germany*. KIT Scientific Publishing, Karlsruhe.

Sandhu, G. Y. (2015). *Frequency Domain Ultrasound Waveform Tomography: Breast Imaging Using a Ring Transducer*. PhD thesis, Wayne State University.

Sandhu, G. Y., Li, C., Roy, O., Schmidt, S., and Duric, N. (2015). Frequency Domain Ultrasound Waveform Tomography: Breast Imaging Using a Ring Transducer. *Phys. Med. Biol.*, 60(14):5381–5398.

Sandhu, G. Y., West, E., Li, C., Roy, O., and Duric, N. (2017). 3D frequency-domain ultrasound waveform tomography breast imaging. *Proceedings of SPIE - the International Society for Optical Engineering*, 10139.

Satomura, S. (1956). A new method of mechanical vibration measurement and its application. *Memoirs of Institute of Scientific and Industrial Research Osaka University*, 13:125.

Schneider, W. A. (1978). Integral Formulation for Migration in Two and Three Dimensions. *GEOPHYSICS*, 43(1):49–76.

Shannon, C. E. (1949). Communication in the Presence of Noise. *IEEE Proceedings*, 37:10–21.

Shi, F. and Huthwaite, P. (2018). Ultrasonic Wave-Speed Diffraction Tomography With Undersampled Data Using Virtual Transducers. *IEEE Transactions on Ultrasonics, Ferroelectrics, and Frequency Control*, 65:1226–1238.

Shin, C., Yoon, K., Marfurt, K. J., Park, K., Yang, D., Lim, H. Y., Chung, S., and Shin, S. (2001). Efficient calculation of a partial-derivative wavefield using reciprocity for seismic imaging and inversion. *GEOPHYSICS*, 66(6):1856–1863.

Simonetti, F. and Huang, L. (2009). Synthetic aperture diffraction tomography for three-dimensional imaging. *Proceedings of the Royal Society of London A: Mathematical, Physical and Engineering Sciences*, 465(2109):2877–2895.

Simonetti, F., Huang, L., and Duric, N. (2007). On the spatial sampling of wave fields with circular ring apertures. *Journal of Applied Physics*, 101(8).

Sourbier, F., Operto, S., Virieux, J., Amestoy, P., and L'Excellent, J.-Y. (2009). FWT2D: A massively parallel program for frequency-domain full-waveform tomography of wide-aperture seismic data—Part 1: Algorithm. *Computers & Geosciences*, 35(3):487–495.

Szabo, T. L. (2014). *Diagnostic Ultrasound Imaging: Inside Out*. Academic Press, Boston, 2nd edition.

Tarantola, A. (1984). Inversion of seismic reflection data in the acoustic approximation. *GEOPHYSICS*, 49(8):1259–1266.

Toksöz, M. N. and Johnston, D. H. (1981). *Seismic Wave Attenuation*. Geophysics Reprint Series No 2. Society of Exploration Geophysicists.

Treeby, B. E., Zhang, E. Z., Thomas, A. S., and Cox, B. T. (2011). Measurement of the Ultrasound Attenuation and Dispersion in Whole Human Blood and its Components From 0-70 MHz. *Ultrasound in Medicine & Biology*, 37(2):289–300.

Vinard, N., Martiartu, N. K., Boehm, C., Balic, I. J., and Fichtner, A. (2014). Optimized transducer configuration for ultrasound waveform tomography in breast cancer detection. *Proceedings of SPIE - the International Society for Optical Engineering*, 10580.

Virieux, J. (1986). P-SV wave propagation in heterogeneous media: Velocity-stress finite-difference method. *GEOPHYSICS*, 51(4):889–901.

Virieux, J. and Operto, S. (2009). An overview of full-waveform inversion in exploration geophysics. *GEOPHYSICS*, 74(6).

Wang, K., Matthews, T., Anis, F., Li, C., Duric, N., and Anastasio, M. A. (2015). Waveform inversion with source encoding for breast sound speed reconstruction in ultrasound computed tomography. *IEEE Transactions on Ultrasonics, Ferroelectrics, and Frequency Control*, 62(3):475–493.

Warner, M. and Guasch, L. (2016). Adaptive waveform inversion: Theory. *GEOPHYSICS*, 81(6):429–445.

Weiwad, W., Heinig, A., Goetz, L., Hartmann, H., Lampe, D., Buchmann, J., Millner, R., Spielmann, R. P., and Heywang-Koerbrunner, S. H. (2000). Direct Measurement of Sound Velocity in Various Specimens of Breast Tissue. *Investigative Radiology*, 35(12).

Wells, P. and Evans, K. (1968). An immersion scanner for two-dimensional ultrasonic examination of the human breast. *Ultrasonics*, 6(4):220–228.

Wild, J. J. and Reid, J. M. (1952). Further Pilot Echographic Studies on the Histologic Structure of Tumors of the Living Intact Human Breast. *Am. J. Pathol.*, 28(5):839–861.

Wild, J. J. and Reid, J. M. (1954). Echographic Visualization of Lesions of the Living Intact Human Breast. *Cancer Research*, 14(4):277–283.

Wiskin, J. W., Borup, D., Johnson, S., Berggren, M., Abbott, T., and Hanover, R. (2007). Full-Wave, Non-Linear, Inverse Scattering. In André, M. P., Akiyama, I., Andre, M., Arnold, W., Bamber, J., Burov, V., Chubachi, N., Erikson, K., Ermert, H., Fink, M., Gan, W. S., Granz, B., Greenleaf, J., Hu, J., Jones, J. P., Khuri-Yakub, P., Laugier, P., Lee, H., Lees, S., Levin, V. M., Maev, R., Masotti, L., Nowicki, A., O'Brien, W., Prasad, M., Rafter, P., Rouseff, D., Thijssen, J., Tittmann, B., Tortoli, P., Van der Steen, A., Waag, R., and Wells, P., editors, *Acoustical Imaging*, pages 183–193. Springer Netherlands.

Wiskin, J. W., Borup, D. T., Iuanow, E., Klock, J., and Lenox, M. W. (2017). 3-D Nonlinear Acoustic Inverse Scattering: Algorithm and Quantitative Results. *IEEE Transactions on Ultrasonics, Ferroelectrics, and Frequency Control*, 64(8):1161–1174.

Wiskin, J. W., Borup, D. T., Johnson, S. A., and Berggren, M. (2012). Non-linear inverse scattering: High resolution quantitative breast tissue tomography. *The Journal of the Acoustical Society of America*, 131(5):3802–3813.

Yang, D., Peng, J., Lu, M., and Terlaky, T. (2006). Optimal Nearly Analytic Discrete Approximation to the Scalar Wave Equation. *The Bulletin of the Seismological Society of America*, 96:1114–1130.

Yang, P., Brossier, R., Métivier, L., and Virieux, J. (2016). A review on the systematic formulation of 3-D multiparameter full waveform inversion in viscoelastic medium. *Geophysical Journal International*, 207(1):129–149.

Yilmaz, O. (2001). *Seismic Data Analysis*. Society of Exploration Geophysicists.

Zapf, M., Pfistner, P., Liberman, C. I., van Dongen, K., de Jong, N., Leyrer, B., Gemmeke, H., and Ruiter, N. (2018). Dice-and-fill single element octagon transducers for next generation 3D USCT. In Hopp, T., Ruiter, N., Bamber, J. C., Duric, N., and van Dongen, K. W., editors, *Proceedings of the International Workshop on Medical Ultrasound Tomography: 1.- 3. Nov. 2017, Speyer, Germany*. KIT Scientific Publishing, Karlsruhe.

Zhang, X., Tan, J., Song, P., Li, J., Xia, D., and Liu, Z. (2017). Time-domain full waveform inversion using the gradient preconditioning based on transmitted waves energy. In *International Geophysical Conference, Expanded Abstracts*, pages 238–241.

Zhang, Z., Huang, L., and Lin, Y. (2011). Full-waveform inversion in the time domain with an energy-weighted gradient. In *81st SEG Annual Meeting, Extended Abstracts*.

List of Figures

List of Tables

Acknowledgments

First of all, I would like to express my deep gratitude to Professor Bohlen, my research supervisor, for proposing the extraordinary topic of this work, useful critiques and sharing my enthusiasm for the project. I am particularly grateful for the assistance given by Thomas H. who proofread my thesis and greatly supported the whole project with his expertise. I would also like to express my very great appreciation to Renat S. for numerous fruitful discussions and enthusiastic encouragement.

I wish to acknowledge the great collaboration with the Institute of Electronics and Data Processing which kindly provided the clinical dataset analyzed in this work. Special thanks go to Nicole R., Torsten H., Michael Z. and Professor Gemmeke for their valuable guidance.

I would like to thank the whole working group of Applied Geophysics at the Karlsruhe Institute of Technology for supporting me during the last year and the staff of the Geophysical Institute, in particular Claudia P. for being an excellent contact for all administrative tasks and Petra K. for IT support. A special thanks goes to my office mates Valérie K., Daniel K. and Bessam A. for sharing all the productive, funny and exhausting moments in the life of a young scientist being thrown in a world full of ideas, jokes and bugs.

Finally, I must express my very profound gratitude to my family, my friends and to my girlfriend for providing me with unfailing support and continuous encouragement throughout my years of study and through the process of researching and writing this thesis. This accomplishment would not have been possible without them.

Declaration on oath

I declare that I have developed and written the enclosed thesis completely by myself, and have not used sources or means without declaration in the text.

.....

(Fabian Kühn)

Appendix

A: Estimation of the numerical dispersion

In the following I want to derive a formula describing the numerical dispersion, caused by the spatial and temporal discretization Δh and Δt, occurring at two-dimensional acoustic wave simulations using finite-differences (FD) methods. To be precise, I consider FD operators second order accurate in time and higher order accurate in space. Therefore, I expand the one-dimensional acoustic approach described by Bohlen and Pan (2018).

For this derivation the acoustic wave equation is expressed as one second-order differential equation

$$\frac{\partial^2 P}{\partial t^2} = c^2 \left(\frac{\partial^2 P}{\partial x^2} + \frac{\partial^2 P}{\partial y^2} \right) , \tag{6.1}$$

where P is the pressure, c is the speed of sound, x and y denote the spatial coordinates and t is the time. It is obtained by differentiating the pressure term in the velocity-stress formulation (equation 3.8), inserting the velocity term and assuming the mass density ρ to be constant in space.

I discretize the wavefield variables as described in section 3.2.1 with the spatial sampling interval Δh and the time step Δt, leading to the following notation:

$$P(x, y, t) = P(l\,\Delta h, j\,\Delta h, n\,\Delta t) = P^{[n]}_{[l,j]} . \tag{6.2}$$

Using the FD method derived from Taylor's polynomial, the second-order derivative of a function $f(\xi)$ at the point ξ_0 with a $2M$th order central FD operator can be approximated as

$$\frac{\partial^2 f(\xi_0)}{\partial \xi^2} = \frac{1}{\Delta \xi^2} \left(-a_0\, f(\xi_0) + \sum_{m=1}^{M} a_m \left(f(\xi_o + m\,\Delta\xi) + f(\xi_o - m\,\Delta\xi) \right) \right) + \mathcal{O}(\Delta\xi^{2M}) , \tag{6.3}$$

Table 6.1: Taylor coefficients a_m for the central finite-differences (FD) approximation of second-order derivatives (Bohlen and Pan, 2018).

M	a_0	a_1	a_2	a_3	a_4	FD accuracy order $2M$
1	2	1				2
2	5/2	4/3	-1/12			4
3	49/18	3/2	-3/20	1/90		6
4	205/72	8/5	-1/5	8/315	-1/560	8

where a_m are coefficients related to the order of accuracy (examples are shown on table 6.1).

Now, I approximate the second-order derivatives in equation 6.1 with the presented FD operator second-order accurate in time and higher-order accurate in space, yielding

$$\frac{1}{\Delta t^2}\left(P_{l,j}^{n+1} - 2P_{l,j}^{n} + P_{l,j}^{n-1}\right) = \frac{c^2}{\Delta h^2}\left(-2\,a_0\,P_{l,j}^{n+1} + \sum_{m=1}^{M} a_m\left(P_{l+m,j}^{n} + P_{l-m,j}^{n} + P_{l,j+m}^{n} + P_{l,j-m}^{n}\right)\right) . \quad (6.4)$$

I consider a plane wave with the angular frequency ω and the incidence angle θ (defined as the angle between the x-axis and the wavenumber vector $\boldsymbol{k} = (k_x\,,\,k_y)^\top = (k\,\cos(\theta)\,,\,k\,\sin(\theta))^\top = (\frac{\omega}{c}\,\cos(\theta)\,,\,k\,\sin(\theta))^\top$, which is described by

$$P_{l,j}^{n} = P_0\,\exp\left(i\left(k_x\,l\,\Delta h + k_y\,j\,\Delta h + \omega\,n\,\Delta t\right)\right) . \quad (6.5)$$

By inserting this in the wave equation 6.4 and dividing by $P_{l,j}^{n}$, I obtain

$$z_t^1 - 2 + z_t^{-1} = r^2\left(-2a_0 + \sum_{m=1}^{M} a_m\left(z_x^m + z_x^{-m} + z_y^m + z_y^{-m}\right)\right) \quad (6.6)$$

with the courant number $r = c\frac{\Delta t}{\Delta h}$ and the exponential terms $z_t = \exp(i\,\Delta t\,\omega)$, $z_x = \exp(i\,k\,\cos(\theta)\,\Delta h)$ and $z_y = \exp(i\,k\,\sin(\theta)\,\Delta h)$.
Replacing the exponential functions with

$$\begin{aligned} a_m\left(z_x^m + z_x^{-m}\right) &= a_m\left(\exp(i\,k\,\cos(\theta)\,m\,\Delta h) + \exp(-i\,k\,\cos(\theta)\,m\,\Delta h)\right) \\ &= 2\,a_m\,\cos(k\,\cos(\theta)\,m\,\Delta h) \end{aligned} \quad (6.7)$$

and solving for $\omega\,\Delta t$ yields

$$\omega\,\Delta t = \arccos\left(1 + r^2\left(-a_0 + \sum_{m=1}^{M} a_m\left(\cos(k\,\cos(\theta)\,m\,\Delta h) + \cos(k\,\sin(\theta)\,m\,\Delta h)\right)\right)\right) . \quad (6.8)$$

Inserting this into the ratio between the numerical and true speed of sound

$$\frac{c_{FD}}{c} = \frac{\frac{\omega}{k}}{c} = \frac{\frac{\omega}{k}}{\frac{r\,\Delta h}{\Delta t}} = \frac{\omega\,\Delta t}{k\,\Delta h\,r} \tag{6.9}$$

and introducing the number of gridpoints per wavelength $G = \frac{\lambda}{\Delta h} = \frac{2\,\pi}{k\,\Delta h}$ yields

$$\frac{c_{FD}}{c} = \frac{G}{2\,\pi\,r}\arccos\left(1 + r^2\left(-a_0 + \sum_{m=1}^{M} a_m\left(\cos\left(\frac{2\,\pi\,m\,\cos(\theta)}{G}\right) + \cos\left(\frac{2\,\pi\,m\,\sin(\theta)}{G}\right)\right)\right)\right) . \tag{6.10}$$

Using $a_0 = 2\sum_{m=1}^{M} a_m$ and $\theta = 0$, i.e. considering wave propagation in x-direction, this becomes equal to the one-dimensional solution proposed by Bohlen and Pan (2018)

$$\frac{c_{FD}}{c} = \frac{G}{2\,\pi\,r}\arccos\left(1 + r^2\left(-\frac{a_0}{2} + \sum_{m=1}^{M} a_m\,\cos\left(\frac{2\,\pi\,m\,\cos(\theta)}{G}\right)\right)\right) . \tag{6.11}$$

To estimate the numerical dispersion for a given spatial and temporal discretization equation 6.10 can be expressed in terms of Δt, Δh, c and frequency f as

$$\frac{c_{FD}}{c} = \frac{1}{2\,\pi\,f\,\Delta t}\arccos\left(1 + c^2\frac{\Delta t^2}{\Delta h^2}\left(-a_0 + \sum_{m=1}^{M} a_m\left(\cos\left(\frac{m\,\cos(\theta)\,2\,\pi\,f\,\Delta h}{c}\right) + \cos\left(\frac{m\,\sin(\theta)\,2\,\pi\,f\,\Delta h}{c}\right)\right)\right)\right) . \tag{6.12}$$